

UC San Diego

UC San Diego Electronic Theses and Dissertations

Title

Optical spectroscopy of carotenoids in self-assembled aggregates and in avian plumage

Permalink

<https://escholarship.org/uc/item/81p1b935>

Author

Berg, Christopher James

Publication Date

2013

Peer reviewed|Thesis/dissertation

UNIVERSITY OF CALIFORNIA, SAN DIEGO

Optical spectroscopy of carotenoids in self-assembled aggregates and in avian
plumage

A Thesis submitted in partial satisfaction of the requirements for the degree
Master of Science

in

Chemistry

by

Christopher James Berg

Committee in charge:

Professor Michael Tauber, Chair
Professor Judy Kim
Professor Charles Perrin

2013

Copyright

Christopher James Berg, 2013

All rights reserved.

The Thesis of Christopher James Berg is approved, and it is acceptable in quality and form for publication on microfilm and electronically:

Chair

University of California, San Diego

2013

TABLE OF CONTENTS

Signature Page	iii
Table of Contents	iv
List of Figures.....	viii
List of Tables.....	xi
Acknowledgements	xii
Abstract of Thesis.....	xiii
1 Introduction	1
1.1 Carotenoids.....	1
1.2 Electronic and Vibrational spectroscopy.....	4
1.3 Exciton-Coupling	12
1.4 Thesis Overview.....	15
2 Resonance Raman excitation profiles of zeaxanthin aggregates.....	16
2.1 Abstract.....	16
2.2 Introduction	17
2.3 Methods and Materials	19
2.3.1 Preparation of zeaxanthin aggregates.....	19
2.3.2 Characterization of zeaxanthin.....	20
2.3.3 Calculation of absolute Raman cross-sections.....	23
2.4 Computational Modeling.....	24

2.4.1	dipole-dipole interactions: Point dipole approximation and the extended dipole model	27
2.5	Results	29
2.5.1	Resonance Raman spectra of zeaxanthin monomer and aggregates	29
2.5.2	Experimental Resonance Raman excitation profiles	34
2.5.3	Depolarization ratios of zeaxanthin monomer (solution and crystal) and aggregates	39
2.5.4	Computational modeling of zeaxanthin monomer and aggregates	40
2.5.5	Zeaxanthin monomer calculated absorption profiles and REPs	41
2.5.6	J1 and J2 aggregate calculated absorption profiles and REPs	45
2.5.7	H aggregate calculated absorption and resonance Raman profiles	51
2.6	Discussion	54
2.6.1	Overview	54
2.6.2	Conclusions from experimental RREPs	55
2.6.3	Conclusions from experimental depolarization ratios	56
2.6.4	Structural differences between J1 and J2 aggregates	58
2.6.5	Computational results for the zeaxanthin aggregates	59
2.6.6	Conclusions	62
2.7	Appendices	63
2.7.1	Calculation of external standard Raman cross-section	63
2.7.2	Comparison of the J1 and J2 UV-vis results with an integrating sphere	64

2.7.3	The different fits for the J1 aggregate	65
2.7.4	The effect of geometry on the absorption spectra of the J2 and H aggregates – Proof for ‘best’ fits	66
3	Vibrational and electronic spectroscopy of rhodoxanthin in avian plumage, solid-state films, and solutions	72
3.1	Abstract.....	72
3.2	Introduction	73
3.3	Methods and Materials	76
3.3.1	Pigment extraction and analysis	76
3.3.2	Preparation of rhodoxanthin isomers.....	78
3.3.3	Thin-film preparation	79
3.3.4	Microscopy	79
3.3.5	Spectroscopy.....	79
3.3.6	Rhodoxanthin photolysis	85
3.3.7	Calculations	86
3.4	Results	87
3.4.1	Pigment extraction and analysis	87
3.4.2	Optical Microscopy	89
3.4.3	Reflectance spectroscopy and Kubelka-Munk analysis	91
3.4.4	Resonance Raman spectra of rhodoxanthin-containing feathers	96
3.4.5	Resonance Raman spectroscopy of rhodoxanthin in solution	101
3.4.6	Resonance Raman spectroscopy of rhodoxanthin thin-films	103
3.4.7	Photolysis of the 6-trans, 6'-cis isomer of rhodoxanthin	104

3.4.8	Calculations of the electronic structure and vibrational frequencies of rhodoxanthin isomers.....	105
3.4.9	Experimental and Calculated evidence for C=O stretch in rhodoxanthin.....	111
3.5	Discussion.....	112
3.5.1	Overview	112
3.5.2	Color and Raman spectroscopy	114
3.5.3	Carotenoid concentration and photonic structure.....	118
3.5.4	Effect of isomerization at the 6/6' position on the vibrational and electronic structure of rhodoxanthin and rhodoxanthin-containing feathers.....	120
3.5.5	High- vs. low- irradiance vs. low- temperature resonance Raman spectroscopy of rhodoxanthin-containing feathers	121
3.5.6	Comparison with carotenoprotein systems.....	122
3.5.7	Possibility of isomerization with thin-films of rhodoxanthin.....	123
3.5.8	High- vs. low- irradiance experimentation.....	125
3.5.9	Effect of changing the level of irradiance on resonance Raman spectroscopy.....	125
3.6	Conclusions	126
3.7	Appendix	127
3.7.1	Supplementary information for publication	127
3.7.2	Assumptions of the “pile of plates” and the effect of ‘sparse’ feathers	141
4	Conclusion and future studies	145
4.1	Conclusions	145
4.2	Future studies.....	149
5	References	151

LIST OF FIGURES

Figure 1.1:	Molecular structure of beta-carotene, zeaxanthin and rhodoxanthin	2
Figure 1.2:	Diagram illustrating the three possible outcomes of a Raman event	6
Figure 1.3:	Diagram showing example ground state and excited state potential energy surfaces	8
Figure 1.4:	Diagram of absorption and resonance Raman according to the sum-over-states formulation	10
Figure 1.5:	Diagram of absorption and resonance Raman according to the time-dependent formulation	12
Figure 1.6:	The three main classifications of dimer orientations.....	14
Figure 2.1:	Absorption spectra of zeaxanthin monomer, J1, J2, and H	21
Figure 2.2:	Schematic showing geometric parameters of a dimer important to the point dipole approximation and extended dipole model	29
Figure 2.3:	Resonance Raman spectra for the zeaxanthin monomer and J1.....	31
Figure 2.4:	Resonance Raman spectra for J2 and H	32
Figure 2.5:	Zeaxanthin monomer and aggregate experimental Raman excitation Profiles for the 4 fundamental vibrational modes and 5 overtone and combination modes	37
Figure 2.6:	Mode-by-mode intensity comparison between zeaxanthin monomer and aggregates	38
Figure 2.7:	Experimental and calculated absorption profiles and REPs for the zeaxanthin monomer	44
Figure 2.8:	Experimental and calculated absorption profiles, REPs, and depolarization ratios for J1	48

Figure 2.9:	Experimental and calculated absorption profiles, REPs, and depolarization ratios for J2	50
Figure 2.10:	Experimental and calculated absorption profiles and REPs for H	53
Figure 2.A1:	Comparison of the J1 and J2 absorption spectra measured with the ISR-3100 integrating sphere	64
Figure 2.A2:	Ratios of the 0-0/0-1 and 0-2/0-1 intensities of the fitted J2 aggregate as a function of the overlay angle and slip angle	67
Figure 2.A3:	Absorption spectra of the J2-J fit.....	68
Figure 2.A4:	Ratios of the 0-0/0-1 and 0-2/0-1 intensities of the fitted J2-J aggregate as a function of the slip angle or intermolecular separation	70
Figure 2.A5:	Position of the H-band as a function of the intermolecular separation using the extended dipole model and the point dipole approximation	71
Figure 3.1:	Pictures of the five rhodoxanthin-containing feathers.....	77
Figure 3.2:	Molecular structure of the three rhodoxanthin isomers.....	78
Figure 3.3:	Diagram of the ISR-3100 integrating sphere.....	80
Figure 3.4:	Normal-phase HPLC chromatogram of <i>Pt. magnificus</i> and absorption spectra of the three major peaks	88
Figure 3.5:	Microscope images of five rhodoxanthin-containing feathers	90
Figure 3.6:	diffuse reflectance and transmittance of the five rhodoxanthin-containing feathers.....	94
Figure 3.7:	Calculated absorption and scattering coefficient profiles of the five rhodoxanthin-containing feathers	95
Figure 3.8:	Resonance Raman spectra of avian feathers acquired with 514.5 nm excitation and a microscope setup, at both room and low temperatures	98
Figure 3.9:	Raman spectra of rhodoxanthin isomers in the solid state and in DMSO with excitation wavelength 568.2 nm.....	102

Figure 3.10:	Absorption spectra and HPLC chromatograms of rhodoxanthin after photolysis.....	105
Figure 3.11:	Results of the Gaussian 09W calculations of three rhodoxanthin isomers.....	108
Figure 3.A1:	Calculated absorption coefficient and scattering coefficient profiles for the five feathers	132
Figure 3.A2:	Resonance Raman spectra of avian feathers with 514.5 nm excitation at high and low irradiance	133
Figure 3.A3:	Absorption spectra of rhodoxanthin isomers in DMSO	134
Figure 3.A4:	Comparison of resonance Raman spectroscopy of high and low irradiance of rhodoxanthin thin films	135
Figure 3.A5:	Comparison of resonance Raman spectra of a 6Z6'E thin film at low and room temperature with 514.5 nm excitation.....	136
Figure 3.A6:	Position of possible carbonyl stretch for the rhodoxanthin and rhodoxanthin-containing feathers.....	138
Figure 3.A7:	Results of the Gaussian 09W calculations of beta-carotene and iso-carotene.....	139
Figure 3.A8:	Image of cockatiel feather held in sample holder.....	145
Figure 3.A9:	Diffuse reflectance, transmittance, and calculated absorption coefficient profiles of cockatiel feathers	146

LIST OF TABLES

Table 2.1:	Raman band assignments and description for zeaxanthin monomer	30
Table 2.2:	Experimental absolute Raman cross-sections for zeaxanthin monomer and aggregates	33
Table 2.3:	Raman depolarization ratios for zeaxanthin monomer and aggregates for the ethylenic mode	39
Table 2.4:	Spectroscopic parameters for the zeaxanthin monomer and aggregates	43
Table 2.A1:	Experimental and literature values for EtOH Raman cross sections	63
Table 3.1:	Summary of experimental Resonance Raman parameters	83
Table 3.2:	Comparison of R_{mid} and $\lambda_{\text{avg half-max}}$ values for the rhodoxanthin- containing feathers.....	95
Table 3.3:	Relevant calculated results for rhodoxanthin isomers, isocarotene, and beta-carotene.....	106
Table 3.4:	Theoretical frequencies of select modes in the Raman spectra of rhodoxanthin.....	106
Table 3.A1:	Band positions of select Raman bands for the rhodoxanthin isomers in DMSO.....	137
Table 3.A2:	Band positions of select Raman bands for thin films of rhodoxanthin isomers with high and low irradiance.....	137
Table 3.A3:	Peak positions of select Raman bands of the feathers at low and room temperature, both with high irradiance excitation	137
Table 3.A4:	Isomerization parameters.....	142
Table 3.A5:	Example conditions and corresponding reflectance values	144

ACKNOWLEDGEMENTS

I would like to acknowledge Professor Michael Tauber for his support as my graduate advisor and chair of my committee. From the time I joined his group as an undergraduate, Prof. Tauber has always made time to mentor me in all aspects of research. I am very grateful for the effort that he takes to cultivate each of his students into highly competent scientists. I believe his tutelage will benefit my future career more than any other single factor.

I would also like to acknowledge the members of the Tauber group. I am lucky to be surrounded by a group of such intelligent, talented, and motivated people, and am thankful that we were able to push the boundaries of science together.

Chapter 2, in part is currently being prepared for submission for publication of the material. Berg, Christopher J.; Tauber, Michael J. The thesis author was the primary investigator and author of this material.

Chapter 3, in part is currently being prepared for submission for publication of the material. Berg, Christopher J.; LaFountain, Amy M.; Prum, Richard O.; Frank, Harry A.; Tauber, Michael J. The thesis author was the primary investigator and author of this material.

Finally I would like to acknowledge my parents and Bethany, for always supporting me and giving me strength to succeed. With your unwavering belief behind me, I will always be able to push forward and never fear failure. I am blessed to have you in my life and any success that I have could not have been possible without you.

ABSTRACT OF THE THESIS

Optical spectroscopy of carotenoids in self-assembled aggregates and in avian plumage

by

Christopher James Berg

Master of Science in Chemistry

University of California, San Diego, 2013

Professor Michael Tauber, Chair

Carotenoids are strongly absorbing pigments that can self-assemble to form aggregates. These aggregates provide an opportunity to study exciton-coupling, which is the delocalization of an excitation over multiple molecules. Two zeaxanthin

aggregates, previously denoted in our group as “J1” and “J2”, exhibit red-shifted absorption relative to the monomer, and a third, “H”, displays a strongly blue-shifted absorption. Raman scattering cross-sections as a function of excitation wavelength are reported for these three zeaxanthin aggregates and the monomer. The aggregates were modeled as dimers to probe the strength of exciton-coupling, intermolecular geometry, and vibrational displacements. The simulations of J1 and J2 suggest that these two aggregates consist of weakly-coupled, card-stacked carotenoids. J2 was found to have a smaller distance and larger rotation angle between the two chromophores, relative to J1. The H-aggregate was fit to a strongly coupled card-stacked orientation.

The possibility of exciton-coupling in carotenoid-containing feathers was investigated with *in situ* resonance Raman spectroscopy, coupled with measurements of diffuse reflectance and transmittance. Rhodoxanthin is the major carotenoid pigment in five different feathers, but there is a large variation in color. Red-shifts in the absorption profiles of these feathers correlated with a decrease in the frequency of the ethylenic mode and an increase in intensity of hydrogen-out-of-plane modes. Isomeric effects were found to be insignificant in terms of the color of the feathers. These studies of zeaxanthin and rhodoxanthin allow for a better understanding of exciton-coupling and illustrate how environment and structure affect the photophysics of carotenoids.

1. Introduction

1.1 Carotenoids

Carotenoids are some of the most abundant and colorful natural pigments in nature. There are over 600 known carotenoids, and they are responsible for the orange color of carrots, the pink color of flamingos, and both the blue and red of uncooked and cooked lobsters. In fact, the vast majority of yellow to red coloration in nature is due to carotenoids or carotenoid metabolites. Carotenoids primarily consist of a C₄₀ hydrocarbon backbone composed from 8 isoprene subunits.¹ Many have cyclic end groups, such as beta-carotene. A large group of carotenoids, termed xanthophylls, and have at least one oxygen atom (e.g. zeaxanthin, astaxanthin, or rhodoxanthin).¹ Carotenoids are defined by their conjugated polyene backbone, where the number of conjugated double bonds commonly is or exceeds N=11. (N=11 for β-carotene, lycopene, and zeaxanthin; N=13 for astaxanthin; N=14 for rhodoxanthin). The most common pattern of double bonds in carotenoids has them located between the following carbons: C7=C8/C7'=C8', C9=C10/C9'=C10', C11=C12/C11'=C12', C13=C14/C13'=C14' and C15=C15' (**Figure 1A** and **1B**). However, a few of the natural carotenoids, such as rhodoxanthin (**Figure 1C**), are didehydrogenated forms of normal carotenoids and have a *retro* pattern, where locations of single and double bonds are switched. In the *retro* carotenoids, the ring units are held more planar relative to the polyene chain than in the more common configuration. The molecular structures of beta-carotene, zeaxanthin, and rhodoxanthin are shown in **Figure 1.1**.

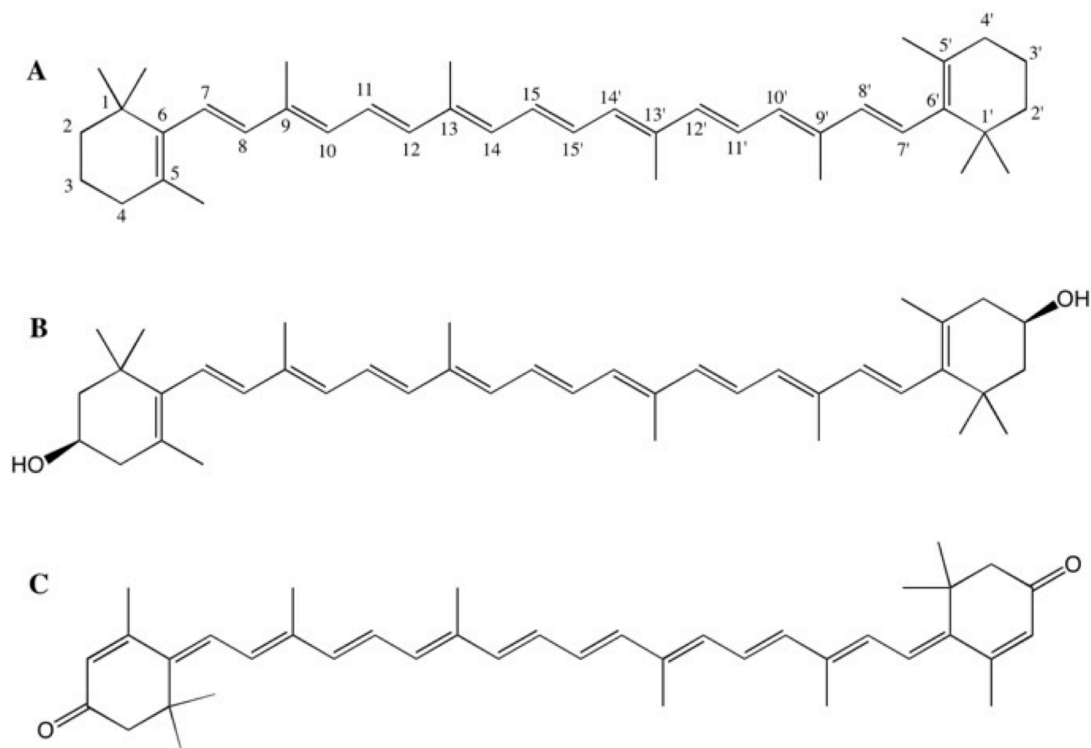


Figure 1.1: Molecular structures of the carotenoids A) β -carotene, B) zeaxanthin, and C) rhodoxanthin.

The number of conjugated double bonds severely changes the energy of the electronic transitions, and thus the observed color of the carotenoids. As the number of conjugated double bonds increases, the energetic difference between the π and π^* energy levels decreases and the primary absorption band undergoes a red-shift. The extent of conjugation is part of the basis for specific colors and hues; the interaction of carotenoids with their environment (usually protein) can also play a large role.³ Therefore, given the tunable nature of the electronic transition, it is not surprising that carotenoids are responsible for a vast array of colors observed in the natural world. Within the animal kingdom, carotenoids contribute to the coloration of plumage in birds,⁴ where they are used for various types of signaling.⁵ As all carotenoids are

obtained through diet or metabolized from dietary carotenoids, carotenoid concentration is an honest signal for fitness in birds, indicating good foraging ability and overall health.⁶ Therefore, carotenoid coloration is often utilized in elaborate courtship displays and is an important criteria in mate selection.⁵ One interesting aspect of carotenoids in avian plumage is that despite similar carotenoid distributions in feathers, the feathers can exhibit considerable variation in color.^{7, 8} Crustaceans also incorporate carotenoids as a method of coloration. Lobsters contain specific proteins that bind astaxanthin as their substrate, where upon binding, the carotenoid absorption exhibits a drastic red-shift.^{9, 10} There are several mechanisms that can account for these changes observed in birds and crustaceans, which include polarization, hydrogen bonding, structural distortion, and exciton-coupling. The modulation of color within rhodoxanthin-containing birds will be the subject of Chapter 3.

Carotenoids are heavily utilized in photosynthesis for harvesting light.^{11, 12} In addition, they provide protection from excessive light and from oxidative damage in both plants and animals.^{6, 13, 14} Carotenoids also play an important part in primate ocular health and there are extremely high concentrations of lutein and zeaxanthin in the macula, where it is thought that they serve as protection from light damage and oxidative species. Increased dietary intake of lutein and zeaxanthin has been implicated in the lowering of risk for age-related macular degeneration, which is caused by a buildup of drusen (cellular debris) in the macula.^{15, 16}

Due to the highly hydrophobic quality of the polyene chain, many carotenoids also exhibit the ability to form different types of non-covalent assemblies in binary aqueous solutions.^{17, 18} Within these aggregates, the electronic structure of carotenoids are changed by a process called exciton-coupling, which will be more fully addressed in section 1.3. Carotenoid aggregates in solution are known to be relatively robust, remaining stable for days at a time.¹⁷ Additionally, the photophysical phenomena of singlet fission, where one singlet excited state gives rise to two triplet states, has been observed in carotenoid aggregates^{19, 20}, carotenoid-containing bacterial photosystems^{21, 22}, and carotenoid-containing lipid membranes²³. This process has applications in solar energy conversion where the possible efficiency of photovoltaics may be increased substantially.²⁴

1.2 Electronic and Vibrational spectroscopy

Spectroscopy is the study of how light interacts with material. Two types of spectroscopy are particularly important for the research considered here, UV-Vis absorption and resonance Raman spectroscopy. UV-Vis spectroscopy is a method used to characterize the excited electronic and vibronic (vibrational states in the excited electronic state) states of a system. In contrast, resonance Raman spectroscopy probes the vibrations of the ground state. However, important excited state properties can also be obtained through resonance Raman spectroscopy.

Raman scattering is an inelastic process where an incident photon is scattered by a molecule and the energy of the scattered photon is changed by an amount equal to

a vibrational or rotational transition. There are two types of Raman events: Stokes and anti-Stokes scattering. In Stokes scattering, the scattered photon is lower in energy than the incident photon while in Anti-Stokes scattering, the scattered photon is of greater energy than the incident photon. This case is possible if the molecule was initially in an excited vibrational state. If there is no change in the energy of the incident photon, this is called Rayleigh scattering. The three processes are shown in **Figure 1.2**. If the incident photon is resonant with an electronic transition of the scattering molecule, then the probability of a Raman event occurring increases by several orders of magnitude. Resonance Raman spectroscopy takes advantage of this resonance effect, and allows for precise probing of a specific chromophore, which is useful in any situation where other molecules may contribute signals that would otherwise obscure the desired information in other types of spectroscopy (ie. IR spectroscopy)

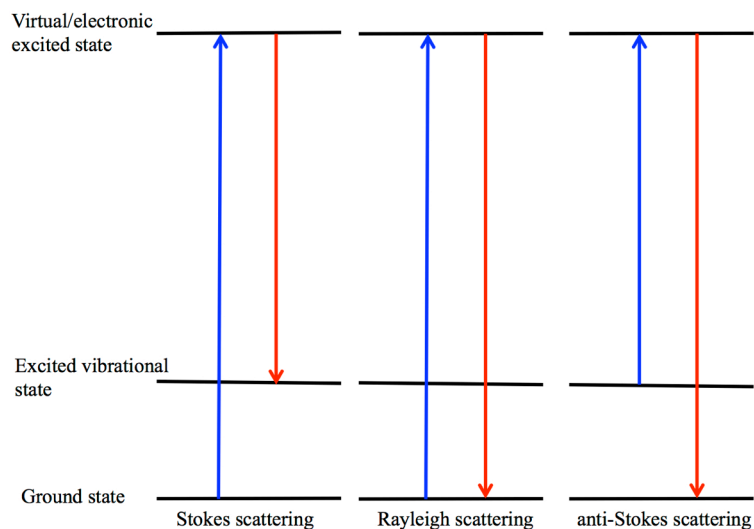


Figure 1.2: Diagram illustrating the three possible outcomes of a Raman event.

Absorption and resonance Raman spectroscopy both depend on the potential energy surfaces of the ground and excited states. The intensities of each transition in an absorption spectrum and resonance Raman spectrum are dependent on the Franck-Condon (FC) factor of that transition, which is defined as the overlap of the vibrational wave functions of the ground and excited states involved in that transition. The Franck-Condon principle states that the most probable transition is a vertical transition from the equilibrium position of the ground state. The equilibrium position of the excited state is often different than that of the ground state, therefore the magnitude of displacement along the corresponding vibrational coordinate, Δ , is very important for the overlap between the ground and excited states (**Figure 1.3**). Within the small Δ

and small homogeneous broadening limit, it is expected that resonance Raman intensities scale as Δ^2 .²⁵

Chapter 2 will deal extensively with the vibrational structure of the zeaxanthin aggregates and the relationship between the dimensionless displacements of each vibrational mode and the corresponding effect on the resonance Raman and absorption cross sections. Therefore, it is necessary to provide a brief theoretical background on the formulations used in the computations featured in Chapter 2. Two different formulations will be covered, the sum-over-states formulation and the time-dependent picture.

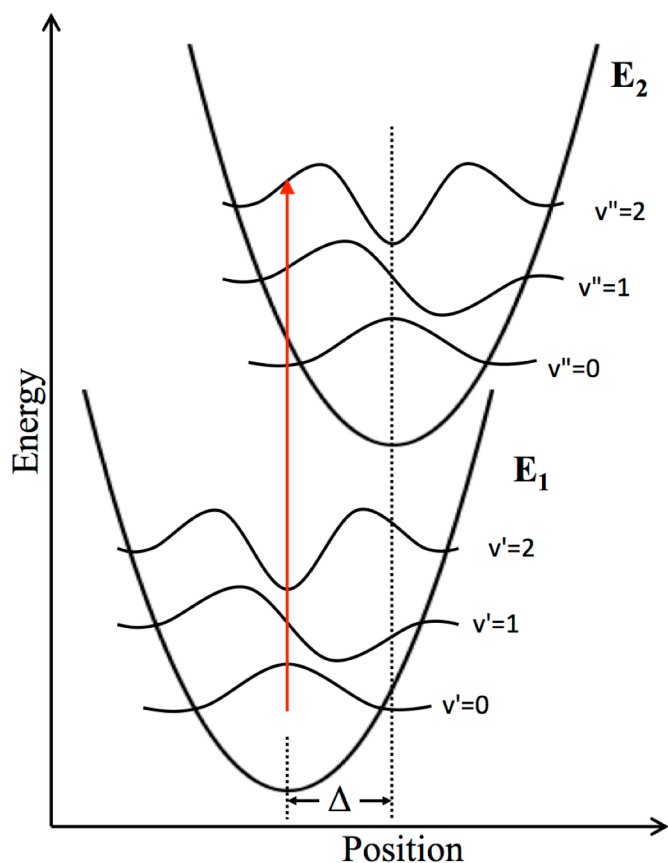


Figure 1.3: Diagram showing an example ground state (E_1) and excited state (E_2) potential energy surfaces. The wave functions of the first three vibrational states are shown. The most probable transition, according to the Franck-Condon principle, is shown by a red arrow. The dimensionless displacement, Δ , is also shown.

Sum-over-states formulation

The sum-over-states formulation is a method of calculating an absorption spectrum and resonance Raman excitation profiles, which is how the resonance Raman cross-sections change as a function of excitation frequency. A basic diagram is shown in **Figure 1.4**. In this case, the likelihood of each possible transition is

considered by computing the Franck-Condon factor between each state involved in the transition. The expression for the absorption cross section, $\sigma_{i,A}(E_L)$, is

$$\sigma_{i,A}(E_L) = \frac{4\pi e^2 M^2 E_L}{3\hbar c} \sum_v \frac{(\hbar\gamma/2)|\langle v|i\rangle|^2}{(\epsilon_v + E_0 - \epsilon_i - E_L)^2 + \Gamma^2} \quad \text{Eq. 1.1}$$

where e is the charge of an electron, M is the transition dipole length and E_L is the frequency of the incident photon, ϵ_i and ϵ_v are the vibrational energies of the initial and excited states, E_0 is the electronic zero-zero energy, and Γ is the homogeneous broadening. The overlap of the wavefunctions is represented by $\langle v|i\rangle$, which is the product of the initial state, $|i\rangle$, with the vibronic state, $|v\rangle$.

Resonance Raman cross sections involve additional considerations, as the overlap between the vibronic state and the final Raman state, $|f\rangle$, must also be considered. The Raman cross sections, $\sigma_{R,i\rightarrow f}(E_L)$, are proportional to the square of the Raman polarizability term and is represented as the following:

$$\sigma_{R,i\rightarrow f}(E_L) = \frac{8\pi e^4 M^4 E_L E_S^3}{9\hbar^4 c^4} \left| \sum_v \frac{\langle f|v\rangle\langle v|i\rangle}{\epsilon_v + E_0 - \epsilon_i - E_L - \Gamma} \right|^2 \quad \text{Eq. 1.2}$$

Additional terms include E_S , which is the frequency of the scattered photon. Both of the above equations are written for single mode systems. However, multimode Franck-Condon factors, such as considered in chapter 2, are modified as a product of all the overlaps of N modes, as described in the following equation:

$$\langle f|v\rangle = \prod_{j=1}^N \langle f_j|v_j\rangle \quad \text{Eq. 1.3}$$

Within large molecules, the number of Raman terms that must be considered become enormous and require much computational time. This is in part motivation for the development of the time-dependent picture.

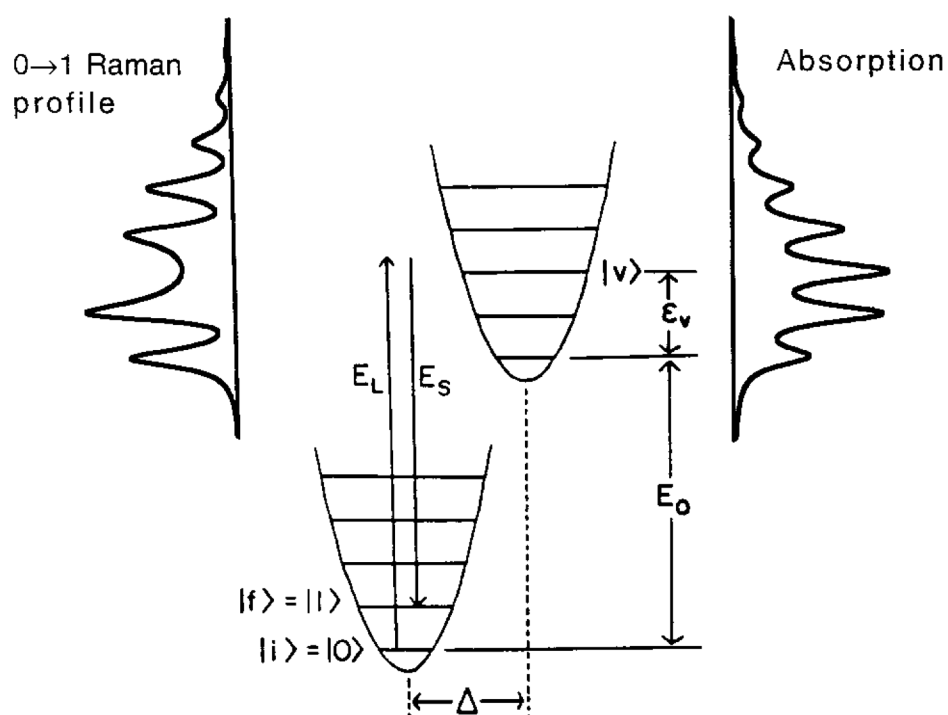


Figure 1.4: This is the absorption and resonance Raman according to the sum-over-states formulation. Shown here is the one-dimensional picture. This figure was taken from Myers (1997).²

Time-dependent picture

The time-dependent picture of Raman scattering was originally introduced by Lee and Heller in 1979.²⁶ A basic diagram is shown in **Figure 1.5**. In this formulation, the systems starts in a vibrational eigenstate of the ground electronic state, $|i\rangle$. Upon excitation by an incident photon, the system is excited and is under the influence of a time-dependent Hamiltonian. Thus, the excited state can now be represented by the propagating wavepacket, $|i(t)\rangle = \exp[-i\hat{H}t/\hbar]|i\rangle$. The absorption cross section, $\sigma_A(E_L)$, is the Fourier transform of the overlap $\langle i|i(t)\rangle$ with respect to the energy multiplied by a homogeneous broadening damping factor, $e^{(-\Gamma t/\hbar)}$. The complete expression is shown below:

$$\sigma_A(E_L) = \frac{4\pi e^2 M^2 E_L}{3\hbar c} \int_{-\infty}^{\infty} \langle i|i(t)\rangle \exp\left[\frac{i(E_L + \epsilon_i)t}{\hbar}\right] e^{(-\Gamma t/\hbar)} dt \quad \text{Eq. 1.4}$$

Similarly, the Raman cross section, $\sigma_{i \rightarrow f}(E_L)$, is the square of the half-Fourier transform of the overlap between the final Raman state with the propagating wavepacket, $\langle f|i(t)\rangle$.

$$\sigma_{i \rightarrow f}(E_L) = \frac{8\pi e^4 M^4 E_L E_S^3}{9\hbar^6 c^4} \left| \int_0^{\infty} \langle f|i(t)\rangle \exp\left[\frac{i(E_L + \epsilon_i)t}{\hbar}\right] e^{(-\Gamma t/\hbar)} dt \right|^2 \quad \text{Eq. 1.5}$$

Also included in this calculation of absorption and resonance Raman excitation profiles is inhomogeneous broadening, which is caused by differences in environment (solvent or otherwise) for each molecule system. The broadening is modeled by a convolution of a Gaussian function with the absorption or Raman excitation profiles.

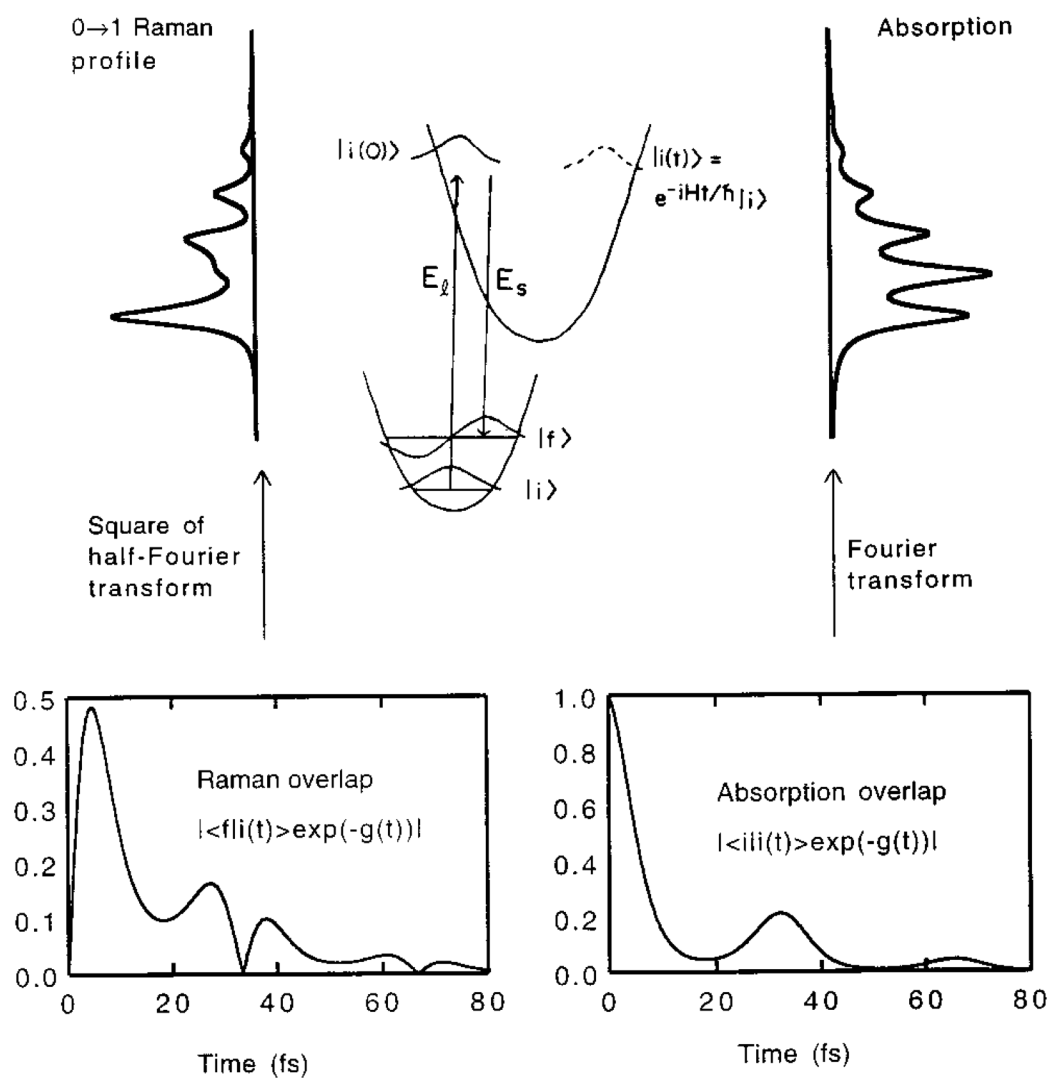


Figure 1.5: This is the absorption and resonance Raman profiles according to the time-dependent formulation. Shown here is the one-dimensional picture. Also shown in the Fourier transforms from the time domain to the energy domain for both Raman and absorption overlaps. This figure was taken from Myers (1997). [2]

1.3 Exciton-Coupling

Exciton coupling is the delocalization of an electronic excitation among multiple chromophores through the coupling of their transition dipoles.²⁷ Although

initially developed by Davydov, Michael Kasha expanded the application beyond crystals to molecular aggregates and lamellar systems.²⁸⁻³⁰ The goal of exciton theory is to explain the changes in the electronic structure observed when a single chromophore becomes coupled to others, such as in crystals or aggregates. The simplest model of exciton theory is the molecular dimer. The Hamiltonian operator of the dimer contains an interaction term, which results in two non-degenerate excited states, one of which will be higher in energy than the unperturbed state, the other lower in energy.³¹ The magnitude of the interaction energy depends on the orientation of the transition dipole moments, the magnitude of the transition dipoles, and the distance between the monomers. The two exciton states are either in-phase or out-of-phase, where the in-phase state is ‘allowed’ and the out-of-phase state is ‘disallowed’. The in-phase state is where the constituent transition dipoles are oriented in the same direction, whereas the out-of-phase state has the transition dipoles opposed to each other. There are two major classifications of types of exciton-interactions. In the J-type interaction, the chromophores are aligned head-to-tail, and the in-phase state is lower in energy than the unperturbed chromophore. In this case, the dimer absorption spectrum would be red-shifted. In the H-type interaction, the chromophores are card-stacked, and the in-phase state is higher in energy than the unperturbed chromophore causing a blue-shift in the absorption spectrum. Orientations that are not strictly head-to-tail or card-stacked can result in two allowed exciton states. A diagram showing the exciton-splitting of a dimer is shown in **Figure 1.6**.

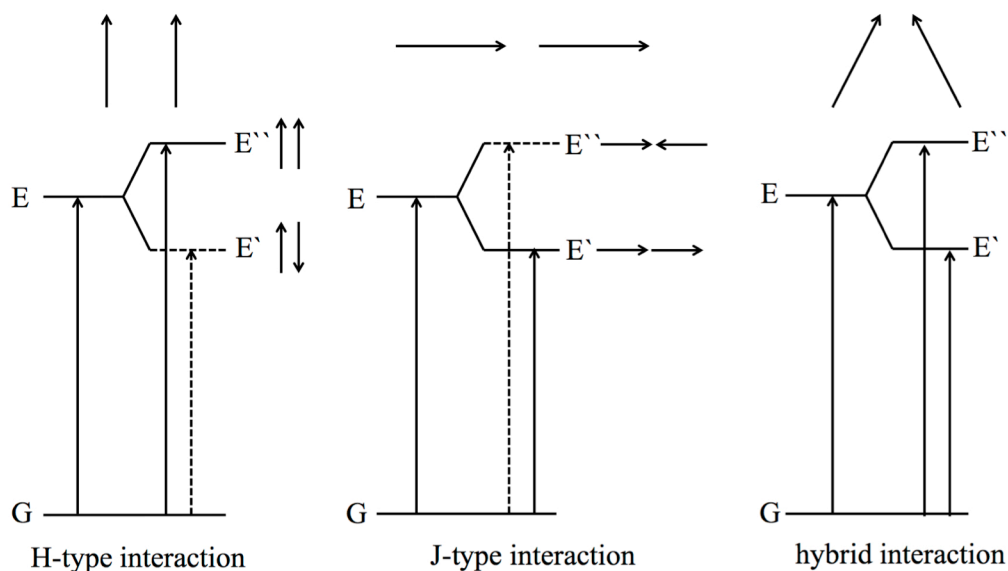


Figure 1.6: The three main classifications of dimer orientations with respect to their transition dipoles are shown above.

The coupling strength is another extremely important parameter to consider when attempting to understand the effects of exciton-coupling. There are three regimes of exciton-coupling: weakly-coupled, intermediately-coupled, and strongly-coupled. In the weakly-coupled regime, the exciton bandwidth is much smaller than the vibrational reorganization energy, whereas in the strongly-coupled regime, the exciton bandwidth is much larger than the vibrational reorganization energy. In the intermediately-coupled regime, the exciton bandwidth and the vibrational reorganization energy are similar.²⁸ Within the weakly-coupled limit, the absorption spectra maintains much of the shape of the unperturbed monomer. In the strongly-coupled limit of a dimer, the vibrational perturbation is equally shared between both

monomers, changing the Franck-Condon factors of each vibrational mode the Δ s are decreased. In the case of a strongly-coupled and infinitely long polymer, the vibrational displacement decreases to a point where the exciton is spread between so many monomers that the excited state becomes vibrationally identical to the ground state. Therefore, only the 0-0 transition is allowed and the absorption profile narrows to a single transition.²⁸

1.4 Thesis Overview

This thesis will be divided into two additional chapters. The first chapter will cover the attempt to model the experimental absorption and resonance Raman excitation profiles with a modified version of a previously developed exciton-coupled dimer model. The optimized geometric orientations and vibrational parameters will be analyzed with respect to exciton theory. The results will also be compared to rREP analysis of the zeaxanthin monomer to gain insight into the effect of exciton-coupling. The possibility of exciton-coupling in carotenoids will also be explored in non-aggregate systems, particularly within avian plumage. The second chapter will investigate the cause of the variance in feather color among five rhodoxanthin-containing bird feathers. Resonance Raman spectroscopy and reflectance spectroscopy will be used in conjunction to determine the changes in electronic and vibrational structure among the birds. In addition, the mechanisms by which the electronic structure is perturbed will be investigated, which could include exciton-coupling, isomeric differences, polarization mechanisms, and structural distortion.

2. Resonance Raman excitation profiles of zeaxanthin aggregates

2.1 Abstract

Raman scattering cross sections as a function of excitation wavelength, otherwise known as Raman excitation profiles (REPs), are reported for three different aggregates of zeaxanthin, and compared with the monomer in solution. Two of the aggregates were previously named “J1” and “J2” because of their overall red-shifted absorption bands relative to the monomer; a third aggregate has a strongly blue-shifted absorption and is an H-aggregate. The Raman cross sections of the four strongest fundamental bands, and five combination or overtone bands, were compared with results from a sum-over-states calculations within the framework of a dimer model.³² The effects of separation between the chromophores, their relative orientation of the chromophores, and the Huang-Rhys displacements were explored. The possibility of replacing the point-dipole approximation of the original model with the extended dipole model was also explored. The absorption and REPs of one weakly-coupled aggregates (J1) was found to be adequately modeled within the dimer model, and a physically reasonable separation for the chromophores was found in the extended dipole model. The optimal orientation of the chromophores found within the dimer model supports the true characterization of the J1-aggregate as a weakly-coupled H-aggregate, as proposed earlier. The model is unsuccessful in modeling the second weak aggregate (J2), which suggests a structure of this aggregate where interactions

other than a single dimer type are important. As expected, the strongly-coupled H-aggregate cannot be modeled as a chromophore pair.

2.2 Introduction

Non-covalent molecular assemblies have gained the interest of the scientific community because they can exhibit different photophysical properties from their constituent monomers, especially in highly conjugated systems.³³ There are many practical applications for these assemblies including electroluminescent devices³³⁻³⁵ and photovoltaics³⁶. The vast list of molecules currently being investigated and studied includes carotenoids. There hundreds of different carotenoids in nature, and are important for photosynthesis³⁷, as anti-oxidants in living organisms³⁸, and their bright colors make them useful for signaling.⁵ The carotenoids have a highly conjugated polyene backbone, which results in a low energy $\pi \rightarrow \pi^*$ transition. Their highly hydrophobic characteristic allows for the formation of stable aggregates in binary solvent mixtures.^{17, 39, 40} During aggregation, the absorption spectra are drastically changed due to exciton-coupling between carotenoid molecules, where the excited state is distributed over two or more molecules. Depending on the orientation of the transition dipoles of the constituent monomers, the absorption spectrum is either shifted to higher or lower energies due to splitting of the excited state into an upper and lower exciton state.²⁸ There are many modern theoretical and experimental studies aimed at understanding the coupling and geometry of carotenoid assemblies.^{41,}

One photophysical process that has attracted much recent interest is singlet fission, where by an excited singlet state distributes its energy over two neighboring molecules to yield two triplet excited states.⁴³ The low energy of the carotenoid triplet excited states generally favors the fission process. The mechanism has been identified as the basis for 5-30% triplet yields in LHC's of purple bacteria²¹, and has been directly observed in carotenoid aggregates^{19, 20}, and carotenoid-containing lipid bilayers²³. Singlet fission could improve the efficiency of solar energy conversion.^{24, 44} Of particular interest to our group is how exciton-coupling and orientation of molecules within aggregated systems changes the excited state. Exciton-coupling is required for singlet fission, and is it therefore necessary to gain information correlating the propensity of a system to undergo singlet fission and the type and magnitude of coupling within that system.

In the present study we have measured and analyzed resonance Raman excitation profiles (rREPs), which are the Raman scattering cross sections of a Raman band as a function of excitation wavelength. By examining how the Raman mode intensities scale with the absorption spectrum of each aggregate, we can gain information about the vibrational displacements of normal modes, and thus the excited state potential energy surfaces. There has been significant foundation laid by the Myer-Kelley group regarding the calculation of Raman excitation profiles and absorption profiles of exciton-coupled dimers using a sum-over-states method,³² and a routine for calculating the absorption and Raman excitation profiles of a single molecule using the Lee and Heller formalism.^{26, 45, 46} Additionally, there has been

extensive theoretical work regarding electronic structure of molecular dimers, including resonance Raman scattering⁴⁷ and vibronic coupling^{48, 49}

Here we will use the exciton-coupled dimer model to investigate the types of interactions that govern the absorption and resonance Raman intensities of three aggregates. The J1 and J2 aggregates have been previously reported as weakly-coupled H-type aggregates, while the H-aggregate exhibits the signs of a strongly coupled H-type aggregate¹⁷ We have also expanded the commonly used method of coupling calculation, the point dipole approximation, to the extended dipole model.⁵⁰ The dimer model is an adequate model for the J1 aggregate, showing good agreement between calculated and experimental absorption spectra and rREPs. However, the J2 aggregate was found to be poorly represented by the dimer model and indicates additional complexity. Lastly, the reduced vibrational displacements and optimized geometry of the H aggregate indicate that the exciton is spread among 3-5 molecules.

2.3 Methods and Materials

2.3.1 Preparation of zeaxanthin aggregates (best overall header for all the “chemical” aspects

Organic solvents (Fisher or Sigma-Aldrich) were spectroscopic-grade and free of stabilizers, or denaturants in the case of ethanol. All were used as received, except tetrahydrofuran (THF), which was passed through an alumina column to remove residual peroxides. Water was deionized with resistivity $\geq 18 \text{ M}\Omega$ (Barnstead, model D11911).

All-trans 3R, 3'R-zeaxanthin was received from DSM Nutritional Products and purified as previously reported.¹⁷ Three kinds of zeaxanthin aggregates were formed by dissolving high-purity all-trans zeaxanthin in various organic solvents, followed by addition of water. The strongly coupled H-aggregate (abbreviated as H) formed upon adding 8 ml water to 2 ml of 50 μ M zeaxanthin in EtOH. One of the weakly-coupled aggregates, denoted "J1" resulted from adding 9 ml water to 1 ml of 100 μ M zeaxanthin in THF. The other weakly-coupled aggregated, denoted "J2" formed with slow addition of 8 ml water to 2 ml of 50 μ M zeaxanthin in 1,4-dioxane. In all cases the mixing of water and zeaxanthin/organic solutions was done while sonicating (Branson, model 3510) and agitating the receiving vial. Samples were sonicated for an additional 10 minutes after mixing.

2.3.2 Characterization of zeaxanthin and zeaxanthin aggregates

UV-Vis: UV-Vis absorption spectra of zeaxanthin monomer and aggregates (**Figure 2.1**) were measured with a scanning spectrophotometer (Shimadzu, UV-3600) using a quartz cuvette with 1 cm pathlength. The molar absorption coefficient (expressed in terms of molar concentration of zeaxanthin) were determined by filtering the zeaxanthin aggregates from each binary solution, followed by quantitative analysis of the residue by dissolution and UV-Vis absorbance measurements of the redissolved monomeric solutions. Repeated measurements indicated that the relative molar absorption coefficients of the aggregates were reliable within 10%. An integrating sphere (Shimadzu, ISR-3100) was used for the J1 and J2 aggregates to eliminate any contribution from scattering (**Figure 2.A1**)

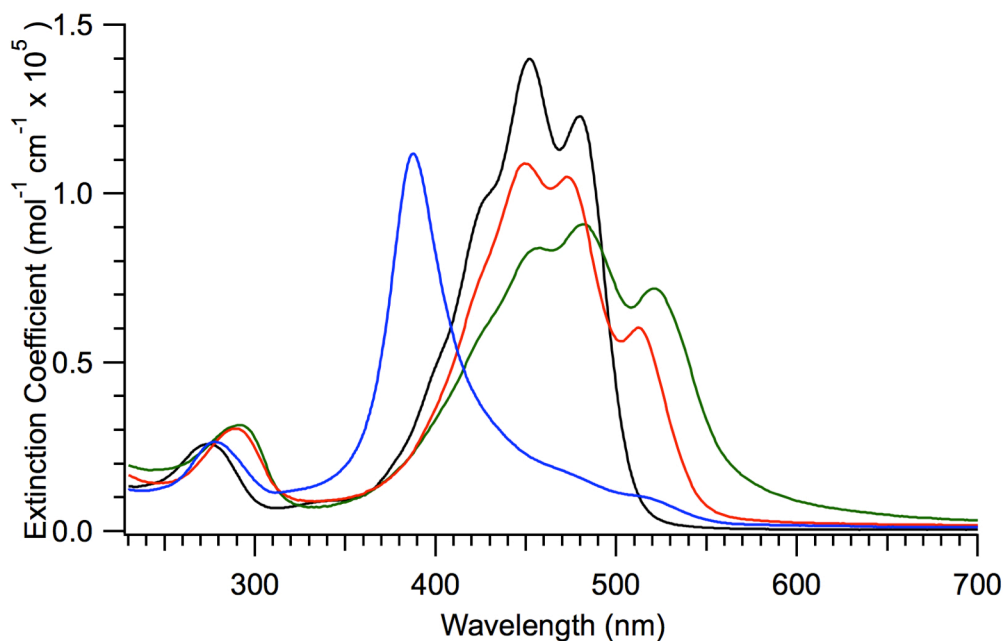


Figure 2.1: Absorption spectra of zeaxanthin monomer (black), J1 (red), J2 (green), and H (blue) aggregates. (J1 and J2 spectra gathered with the ISR-3100 are shown in **Figure 2.A1**).

CW-Resonance Raman: 457.9, 488.0, 514.5, 530.9, and 568.2nm excitation wavelengths were generated by an Argon/Krypton ion laser (Laser Innovations, Innova-70C). A laser pointer was used for 404.3 nm excitation. A picosecond laser system¹⁹ was used to generate additional excitation wavelengths 415, 473, 501, 527, 551 and 599nm. Briefly, ~3 mJ 1kHz pulses at either 800 or 830 nm from a Ti:sapphire regenerative amplifier (Spectra-Physics Spitfire XP-Pro) were directed into a specialized second-harmonic generator (Light Conversion SHBC) that lengthened the incoming pulses more than 30-fold and narrowed their bandwidth. The 400 or 415 nm pulse energy was ~1.2-1.5 mJ, with ~15 cm^{-1} bandwidth and 4 ps duration. The second harmonic pulses were focused into a 47 cm length pipe that was

filled with either ~ 1200 psi pressure D_2 or H_2 gas. Desired wavelengths were produced by stimulated Raman scattering and the beam of interest was selected with a prism and various irises.

The sample was flowed through a horizontal capillary with inner dimensions of 2×2 mm. The excitation power ~ 1.0 mW at the sample. Raman scattering was collected at a 90° angle relative to the excitation beam with a F/1.2 camera lens (Canon FD, focal length 85 mm), and focused onto spectrograph with a F/4 achromatic lens. The appropriate edge filter (Semrock) for each excitation wavelength was installed before the entrance slit for each of the wavelengths to reject Rayleigh scattering. A depolarizer (Sigma Koki DEQ-2S) was used to scramble the polarization of the incoming light, and therefore compensate for differing response efficiencies of the spectrograph to p-polarized and s-polarized light. The spectrograph has a f.l. of 320 mm, and was equipped with a 1200 groove/mm holographic grating and open-electrode CCD detector (Horiba Jobin-Yvon, iHR-320 and Synapse) was used to disperse and detect the Raman scattering. The slitwidth was 0.1 mm and the spectral resolution is better than 10 cm^{-1} . Raman shifts were calibrated with the known peak positions of the reference solution of acetonitrile and toluene 50:50(v/v). Sample O.D. was lower than 0.3 at the excitation wavelength. Attenuation of the excitation beam or the Raman scattering were corrected for with the transmission spectrum and experimental excitation and emission pathlengths. Raman spectra were also corrected for instrument response of the detection system through calibration of a white light

source (Acton Research, TDS-429). Solvent peaks were removed from the sample spectra by subtracting the solvent-only spectra.

Raman depolarization ratios: The depolarization ratio ρ of the Raman scattering is defined as $\rho = I_{\perp}/I_{\parallel}$, where I_{\parallel} and I_{\perp} are the intensities of scattered light with polarization that is parallel or perpendicular to that of the excitation. These intensities were analyzed with a dichroic polarizer (OptoSigma) mounted on a rotation stage was positioned between the F/4 focusing lens and depolarizer. The known depolarization ratios of the 992 cm^{-1} benzene Raman band ($\rho = 0.03$) and the 459 cm^{-1} carbon tetrachloride Raman band ($\rho = 0.008$) were used to fine-tune the parallel and perpendicular orientations of the polarizer⁵¹

2.3.3 Calculation of absolute Raman cross-sections

The absolute Raman scattering cross-section of a Raman band is determined by the ratio of the intensity of the band with the Raman intensity of a known band. The expression for the absolute Raman cross-sections, σ , of a sample(S) and reference(R), are shown in **Eq. 2.1** and **2.3**.^{52, 53}

$$\sigma_S = \left(\frac{I_S(\Omega)}{I_R(\Omega)} \right) \frac{c_R}{c_S} \sigma_R D \quad \text{Eq. 2.1}$$

$$\text{and,} \quad D = \left(\frac{1 + 2\rho_S}{1 + \rho_S} / \frac{1 + 2\rho_R}{1 + \rho_R} \right) \quad \text{Eq. 2.2}$$

Where $I(\Omega)$ is the intensity of the Raman band, c_S and c_R are the concentrations of the sample and reference, and D is a correction factor for the difference in depolarization

ratios, ρ , of the reference and sample Raman bands. The absolute Raman cross-section of the reference band was not known prior to the present study by either experiment or literature for every excitation wavelength gathered in the present study. Therefore, **Eq. 2.3** was employed to fit the known cross section values to an Albrecht *A*-term^{52, 54}

$$\sigma_R = \frac{8\pi}{3} \frac{1 + 2\rho}{1 + \rho} K v_e v^3 \left[\frac{v_e^2 + v_0^2}{(v_e^2 - v_0^2)^2} + C \right]^2 \quad \text{Eq. 2.3}$$

where v_0 is the incident photon energy, v is the scattered photon energy, v_e is the electronic resonant energy, C is a contribution from other electronic states, and K is the fitting parameter. The reference band is the 884 cm^{-1} band of ethanol for all excitation wavelengths, with the exception of 404.3 nm excitation wavelength, where the 2900 cm^{-1} band of ethanol was used instead due to chromatic aberrations. Additional details are in the Appendix.

A multi-peak fitting routine (Multi-peak fitting 2.0, IGOR Pro, Wavemetrics) was used to fit the Raman bands of each spectrum with Voigt functions. The integrated area of a particular band, with respect to the frequency domain, was taken to be the intensity of that Raman transition.

2.4 Computational modeling

Two previously developed computational routines were used to calculate the absorption spectra and resonance Raman excitation profiles of the zeaxanthin monomer and zeaxanthin aggregates, one of which was designed to model

excitonically coupled dimers.^{45, 32, 46} The monomer absorption and resonance Raman excitation profiles were simulated by using the time-dependent picture according to the Lee and Heller formalism²⁶, which was described earlier (Chapter 1). We assume that there is no change in the vibrational frequencies between the ground and excited state and that there is no transformation in the character of the normal modes in the excited state (Duschinsky rotation). The homogeneous broadening was modeled as a time-dependent exponential decay and the inhomogeneous broadening was modeled as a Gaussian distribution of the frequency of the electronic transition. The frequency of the electronic zero-zero transition, transition dipole length, and dimensionless displacements of each vibrational mode were also adjusted and used to obtain the best fits to the absorption and resonance Raman excitation profiles.

The aggregates were modeled as a dimer of exciton-coupled monomers. The interaction between the transition dipoles of the chromophores was computed in two ways. The first was the point-dipole approximation (PDA) and the second was the extended dipole model (EDM). In addition to the same parameters that are included in the monomeric routine, there are three adjustable parameters describing the relative orientation of the monomers, which included 1) the center-to-center distance, 2) the rotation angle, and 3) the slip angle. The interactions are described further below in section 2.4.1. This routine uses a sum-over-states picture rather than the previously used time-dependent picture. The symmetric and anti-symmetric contributions to the excited states are used to calculate the Raman tensors and overlaps necessary to

calculate the absorption profile, resonance Raman excitation profiles, and depolarization ratio profiles.

Each of these routines were coupled with a non-linear solver 'lsqcurvefit' from MATLAB's Optimization ToolKit, which utilized a non-linear least squares algorithm to optimize the fitting parameters. The algorithm iteratively changed the fitting parameters to find the best fit between the experimental and calculated results, until a sufficiently good agreement was reached. While modeling the aggregates, the routine was also instructed to consider the depolarization ratios. The routine was instructed to weigh each of the parameters equally in determining the best fit. However, the automated routine did not always determine at the best fit with the aggregates, but often gravitate towards a local minimum. Therefore the automated routine was used to estimate the molecular parameters and further fine-tuning was done manually. Manual fitting involved iteratively finding the value for each parameter that yielded the best fit to the experimental data. Using a 2011 MacBook Pro with 2.3 GHz Intel i5 processor and MATLAB R2011b, the monomer REP optimization procedure completed the fit between 5 and 30 minutes depending on the initial input parameters and number of parameters constrained. The computational time required of the dimer REP routine was significantly greater, especially when considering larger numbers of vibrational modes or higher vibrational states.

2.4.1 dipole-dipole interactions: Point dipole approximation and the extended dipole model

The point dipole approximation is the crudest description of the interaction between transition dipoles of two molecules. The general expression in vacuum is ^{32, 55}

$$J_{12} = \frac{\mu_A \mu_B}{4\pi\epsilon_0 R_{AB}^3} (\sin\theta_A \sin\theta_B \cos\phi - 2\cos\theta_A \cos\theta_B) \quad \text{Eq. 2.4}$$

where μ is the transition length of the molecule (eÅ), ϵ_0 is the permittivity of free space and R_{AB} is the distance between the centers of the two monomers. The slip angles, θ_A and θ_B , are the angles between each transition dipole vector and a line connecting the centers of the monomers. ϕ is the angle of rotation between the transition dipole vectors (**Figure 2.2**). The validity of the point dipole approximation depends upon whether the separation of the molecules is greater than the lengths of the molecules. ⁵⁶ If the approximation is used at shorter distances, not only can the magnitude of the energy be too large, but even the sign of the interaction integral can be wrong, relative to quantum mechanical calculations. ⁵⁰ Although PDA is known to be inaccurate, it is still commonly used as an approximate method of determining the magnitude of coupling. ^{36, 57}

The alternative method that is used in this project to determine the exciton-coupling between two monomers is the extended dipole approximation, which was originally proposed and developed by Czikkely and Kuhn. ⁵⁰ The basis of the model

is to replace the molecule with two point charges separated by the length, l . The expression for the interaction integral (J_{12}) in a vacuum is

$$J_{12} = \frac{\epsilon^2}{4\pi\epsilon_0} \left(\frac{1}{r_{++}} + \frac{1}{r_{--}} - \frac{1}{r_{\pm}} - \frac{1}{r_{\mp}} \right) \quad \text{Eq. 2.5a}$$

$$= \frac{\mu^2}{4\pi\epsilon_0 l^2} \left(\frac{1}{r_{++}} + \frac{1}{r_{--}} - \frac{1}{r_{+-}} - \frac{1}{r_{-+}} \right) \quad \text{Eq. 2.5b}$$

where the four r_{ij} terms are the distances between the point charges on each molecule.

Figure 2.2 shows the relevant distances and angles. To the best of our knowledge there is no previous precedent for carotenoids or polyenes and the EDM. We have estimated the length, l , to be equal to the conjugation length, which is approximately 23Å for zeaxanthin. Although the magnitude of charge on each of the point charges is not explicitly necessary, according to the model it would be defined as $\pm\epsilon$, where ϵ is the charge of the transition dipole and equal to $\frac{\mu}{l}$. As noted by previous studies, the extended dipole model offers better agreement to quantum mechanical calculations than the point-dipole approximation.^{58, 59} However, given the same ϕ and θ angles, most magnitudes of J_{12} calculated by one model may be achieved by the other by changing R_{AB} .

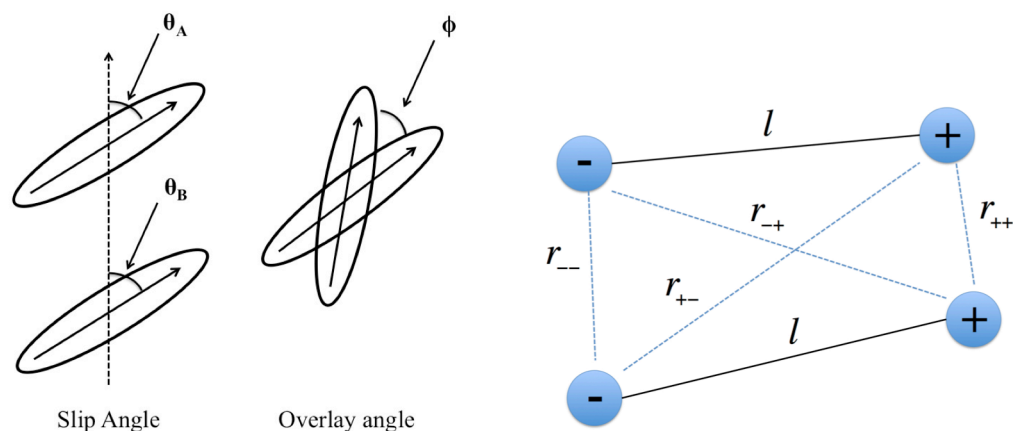


Figure 2.2: Left) schematic showing the two different angles considered in this report. A top view is used to show the overlay angle. Right) distances and notation used in the extended dipole approximation.

2.5 Results

2.5.1 Resonance Raman spectra of zeaxanthin monomer and aggregates

The resonance Raman spectra of zeaxanthin monomer and aggregates were acquired with 6 – 10 different excitation wavelengths as shown in **Figures 2.2** and **2.3**. The resonance Raman spectrum of zeaxanthin is characterized by three strong bands at 1525 cm^{-1} , 1156 cm^{-1} , and 1005 cm^{-1} . These bands correspond to normal modes that are primarily C=C stretch, C-C stretch, and methyl rock, respectively. The relative intensities of each mode follows the pattern: C=C stretch > C-C stretch > methyl rock. We are also investigating the intensities of the large fundamental peaks, the 965 cm^{-1} hydrogen out-of-plane mode, and 5 overtone or combination bands at 2164 cm^{-1} , 2312

cm^{-1} , 2525 cm^{-1} , 2672 cm^{-1} , and 3040 cm^{-1} . The Raman bands will be referred to as the assignments given in **Table 2.1** for the remainder of the report.

Table 2.1: Raman band assignments and description for zeaxanthin monomer.

Approximate Raman frequency (cm^{-1})	Assignment	Description
965	ν_4	Hydrogen out-of-plane wag
1008	ν_3	methyl rock
1156	ν_2	C-C stretches + C-H in-plane bends
1525	ν_1	C=C stretches
2164	$\nu_3 + \nu_2$	Combination band
2310	$2\nu_2$	Overtone band
2525	$\nu_3 + \nu_1$	Combination band
2672	$\nu_2 + \nu_1$	Combination band
3040	$2\nu_1$	Overtone band

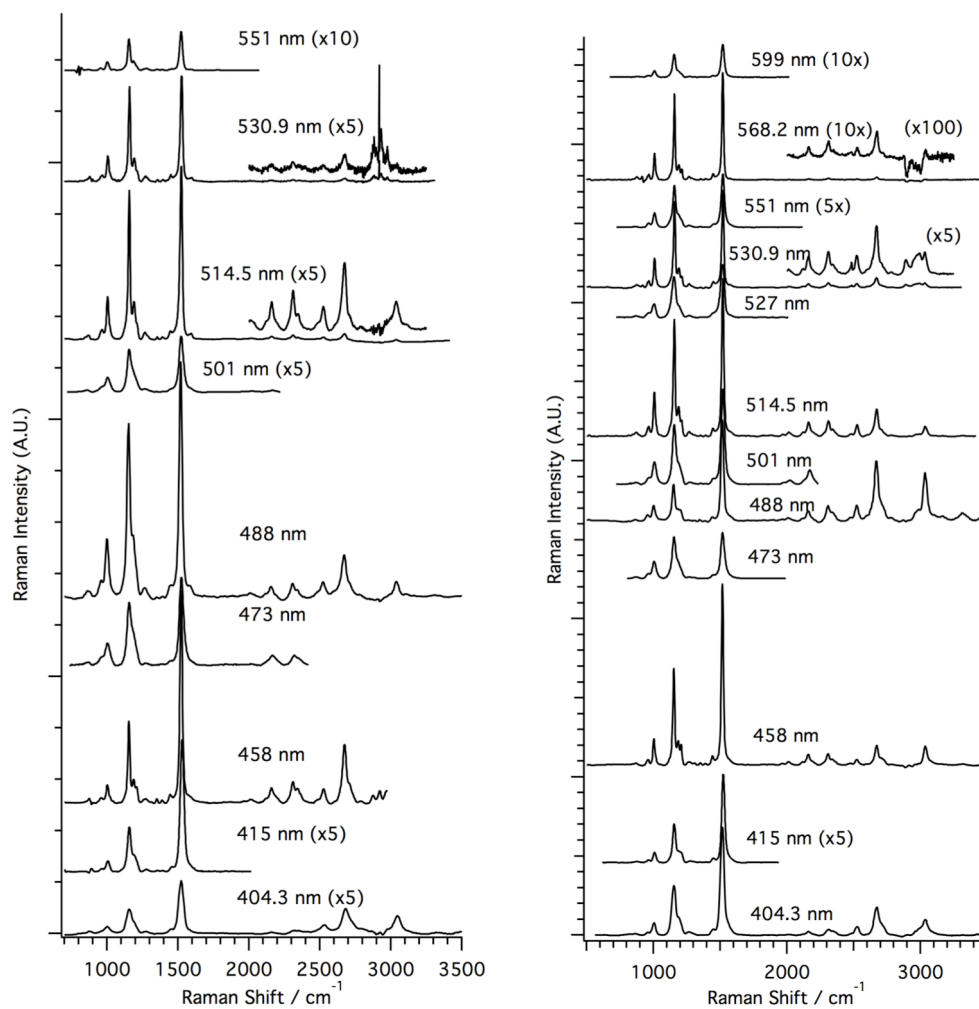


Figure 2.3: Resonance Raman spectra for the zeaxanthin monomer (left) and J1 aggregate (right). The overtone and combination region are magnified by a scalar as indicated in the figure. Spectra acquired with the pulsed laser system (415, 473, 501, 527, 551, 599 nm) were acquired only for the fundamental bands. All spectra are corrected for relative concentration, self-absorption, and laser power.

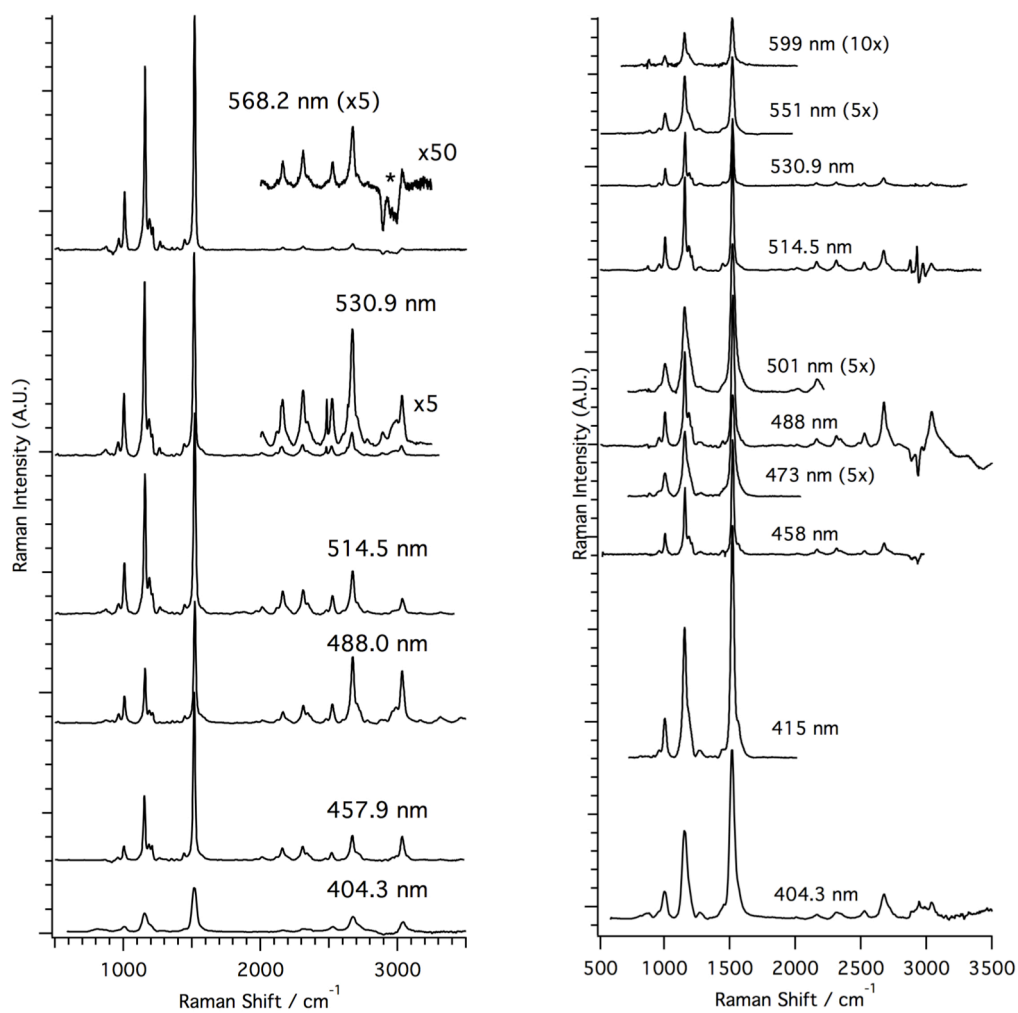


Figure 2.4: Resonance Raman spectra for the zeaxanthin J2 aggregate (left) and H aggregate (right). The overtone and combination region are magnified by a scalar as indicated in the figure. Spectra acquired with the pulsed laser system (415, 473, 501, 527, 551, 599 nm) were acquired only for the fundamental bands. All spectra are corrected for relative concentration, self-absorption, and laser power.

Table 2.2: Experimental absolute Raman cross-sections for zeaxanthin monomer and aggregates.

Excitation Wavelength (nm)	Raman Cross Section / $10^{-8} \text{ \AA}^2 \text{ molecule}^{-1}$								
Monomer	965 cm^{-1}	1008 cm^{-1}	1156 cm^{-1}	1525 cm^{-1}	2164 cm^{-1}	2310 cm^{-1}	2525 cm^{-1}	2672 cm^{-1}	3040 cm^{-1}
404.3	13.1	33.8	124	247	21.5	7.19	28.4	109	80.0
415	4.30	17.2	95.3	267					
457.9	9.50	36.1	156	458	40.7	77.8	54.2	282	120
473	45.6	99.0	247.8	347					
488.0	38.5	191	440	638	82.4	63.0	59.2	136	71.4
501	15.6	56.3	124	213					
514.5	3.17	14.9	40.5	60.6	2.10	2.47	1.77	4.93	0.94
530.9	0.87	3.78	12.6	17.7	0.24	0.39	0.28	0.94	
551	0.23	1.11	4.62	6.18					
J1-agg	965 cm^{-1}	1008 cm^{-1}	1156 cm^{-1}	1516 cm^{-1}	2164 cm^{-1}	2310 cm^{-1}	2525 cm^{-1}	2672 cm^{-1}	3040 cm^{-1}
404.3	4.85	26.9	137	261	11.3	20.7	25.6	94.6	50.2
415	1.64	7.31	32.1	72.0					
457.9	8.61	41.5	156	314	32.1	34.2	15.2	57.2	44.8
473	6.45	54.5	108	145					
488.0	4.46	11.4	28.5	66.8	13.8	14.5	11.1	68.0	36.2
501	2.63	13.0	41.6	74.0					
514.5	12.2	45.0	105	157	18.3	15.5	11.0	29.0	13.9
527	8.47	17.3	67.1	69.1					
530.9	5.11	23.4	76.5	102	5.93	5.67	3.79	11.0	
551	0.86	3.11	9.14	14.6					
568.2	0.36	1.46	4.91	6.07	0.11	0.19	0.08	0.28	
599	0.17	0.50	1.69	2.85					
J2-aggregate	965 cm^{-1}	1008 cm^{-1}	1156 cm^{-1}	1516 cm^{-1}	2164 cm^{-1}	2310 cm^{-1}	2525 cm^{-1}	2672 cm^{-1}	3040 cm^{-1}
404.3	0.42	4.13	34.5	71.5	4.02	4.12	4.91	28.7	19.3
457.9	1.67	12.5	64.1	186	21.4	30.0	13.3	54.8	41.0
488	5.41	23.1	46.4	99.3	16.7	27.5	24.4	101	80.7
514.5	14.8	48.2	128	199	33.6	28.6	19.8	72.1	23.4
530.9	6.72	35.5	106	131	7.09	6.64	7.27	13.2	10.9
568.2	0.95	4.24	11.1	117.4	0.33	0.32	0.39	0.80	

Table 2.2: (continued)

Excitation Wavelength (nm)	Raman Cross Section / $10^{-8} \text{ \AA}^2 \text{ molecule}^{-1}$								
	H-aggregate	965 cm^{-1}	1008 cm^{-1}	1156 cm^{-1}	1525 cm^{-1}	2164 cm^{-1}	2310 cm^{-1}	2525 cm^{-1}	2672 cm^{-1}
404.3	3.77	17.5	92.3	137	5.09	6.37	4.35	19.0	7.52
415	1.51	13.5	47.3	81.6					
457.9	0.31	1.62	5.61	9.55	0.57	0.59	0.45	1.82	2.81
473	0.16	1.29	2.62	5.21					
488.0	1.00	4.08	12.8	20.1	1.30	2.40	2.74	7.42	10.7
501	0.11	1.26	4.27	8.22					
514.5	0.83	2.84	6.91	12.3	1.47	1.88	1.08	3.56	1.45
530.9	0.21	1.25	3.34	5.76	0.31	0.27	0.31	0.62	
551	0.11	0.41	0.92	1.70					
599		0.05	0.20	0.31					

2.5.2 Experimental Resonance Raman excitation profiles

The experimental resonance Raman excitation profiles (RREPs) of the zeaxanthin monomer and aggregates are shown in **Figure 2.4** and overlaid with the absorption profile of the corresponding sample. **Figure 2.5** shows the mode-by-mode comparison of intensity between the monomer, J1, J2, and H aggregates. The absolute Raman cross-section values are listed in **Table 2.2** and are reproducible within 20%.

The zeaxanthin monomer Raman scattering intensities of the 4 fundamental bands follow have similar excitation profiles in the visible wavelength region. The 3 large fundamental modes (ν_1 , ν_2 , and ν_3) each have a experimental maximum at 488.0 nm, corresponding to the $0 \rightarrow 0$ electronic transition. The global maximum of ν_4 is 473

nm excitation, but is only slightly higher than the Raman scattering cross-section at 488.0 nm excitation. ν_1 also has another local maximum at 457.9 nm, near the absorption maximum. The $\nu_2+\nu_3$ and $\nu_1+\nu_3$ bands have the greatest cross-sections with 488.0 nm excitation; the other overtone and combination bands are greatest with 457.9 nm excitation.

The Raman intensities of J1 bands have the greatest intensities at excitation wavelengths that correspond to the 0 \rightarrow 0 and 0 \rightarrow 2 vibronic transitions, near 514.5 nm and 457.9 nm. J1 has very little Raman activity at 488.0 nm excitation, but surprisingly large intensities at 404.3 nm. The trend of large intensities at 404.3 nm carries over to the overtone and combination bands as well; the $2\nu_1$, $\nu_1+\nu_2$, and $\nu_1+\nu_3$ bands show highest Raman intensity at 404.3 nm excitation. It is possible that the contribution from the ν_1 mode causes the overly large Raman cross-section in these overtone and combination bands. Additionally, it is observed that the RREPs for the overtones or combination modes that do not have contribution from the ν_1 mode appear significantly different than the bands that do, with cross section maxima at 457.9 nm and 514.5 nm.

Similarly to the J1 aggregate, J2 Raman bands have local maxima with 514.5 and 457.9 nm excitation (corresponding to the 0 \rightarrow 0 and 0 \rightarrow 2 vibronic transitions) and a relatively lower Raman intensity at 488.0 nm excitation. The overtone and combination bands with ν_1 contribution ($\nu_1+\nu_3$, $\nu_1+\nu_2$, and $2\nu_1$) have greatest Raman intensity at 488.0 nm. The $\nu_2+\nu_3$ and $2\nu_2$ bands have lower Raman activity at this wavelength, resulting in a local minimum. As with the J1 aggregate, the overtone and

combination bands that do not have contributions from the ν_1 mode have a distinct RREP from those that do.

The rREP of H for all of the studied modes show closely track with the absorption profile, showing an increase of Raman activity as the excitation wavelengths become bluer. The overtone and combination intensities show a significant increase in Raman activity at 488.0 nm. Unlike that J1 and J2 aggregates, there does not seem to be a significant difference in the RREPs of the modes studied here.

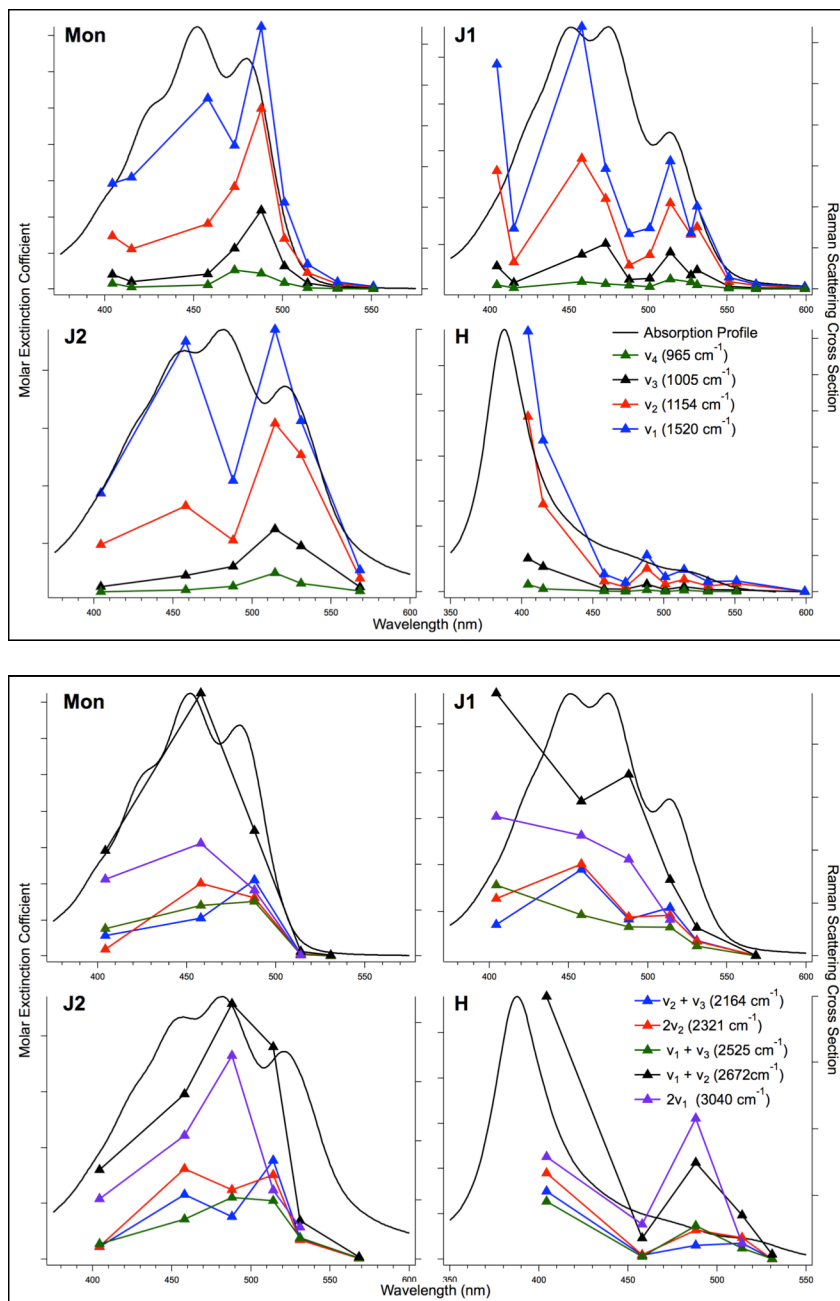


Figure 2.5: Zeaxanthin monomer and aggregate experimental resonance Raman excitation profiles for the 4 fundamental vibrational modes (upper) and 5 overtone/combination modes (lower). The numerical values can be found in Table 2.2. Lines between experimental points are added to guide the eye of the reader.

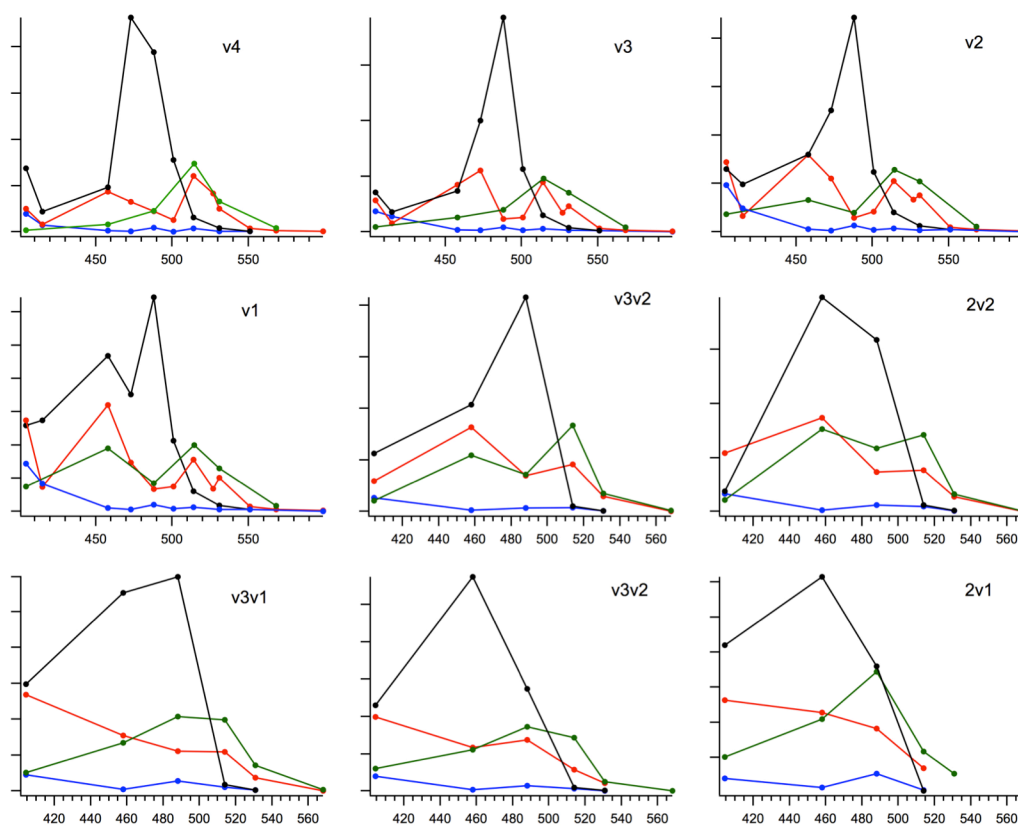


Figure 2.6: Mode by mode intensity comparison between zeaxanthin monomer (black), J1 aggregate (red), J2 aggregate (green), and H aggregate (blue). The modes are labeled in the figure. Lines between experimental points are used to guide the eye of the reader.

From **Figure 2.6**, it is clear at the peak of the rREPs for each mode that the monomer has the greatest intensity. The cross-sections of J1 and J2 are similar to one another, although generally half that of the monomer at the peak cross-section. The H aggregate cross-section are much lower, even at wavelengths approaching the peak absorption.

2.5.3 Depolarization ratios of zeaxanthin monomer (solution and crystal) and aggregates

The magnitude of perturbation of the Raman depolarization is correlated to electronic coupling and molecular symmetry.^{32, 60} As with the resonance Raman cross-section calculations, the intensity is determined as the integrated area of the Raman band. The results are shown in **Table 2.3**. Only the ν_1 depolarization ratio is reported as all the studied Raman lines exhibit the same depolarization ratios at each excitation wavelength.

Table 2.3: Raman Depolarization Ratios for Zeaxanthin monomer and aggregates for the ethylenic (ν_1) mode. Error is ± 0.01 for all measurements.

Zeaxanthin	Excitation Wavelength (nm)			
	514.5	488.0	476.0	457.9
Monomer	N/A	.34	N/A	.34
J1-agg	N/A	.36	.37	.36
J2-agg	N/A	.28	.34	.29
H-agg	N/A	.36	N/A	.44

The depolarization ratios of β -carotene and astaxanthin have been previously reported in the literature⁵¹ and consistently reported as $\frac{1}{3}$ at 488.0 nm excitation for both ν_1 and ν_2 mode. Our results for the solution-phase zeaxanthin monomer agree with the literature values and allow us to proceed with confidence with the aggregate results.

The depolarization ratios of the aggregates are only deviate slightly from the monomer. The J1 aggregate was consistently measured to be $\rho = \sim 0.36$ while the J2 aggregate ρ values are < 0.33 at 488.0 and 457.9 nm and ~ 0.33 at 476 nm. The

depolarization ratio dispersion for H is greater than the J1 or J2 aggregates. Error in these measurements are small, approximately ± 0.01 .

2.5.4 Computational modeling of zeaxanthin monomer and aggregates

A computational routine that was designed by Anne Myers Kelley and Eric Shorr was used to optimize the electronic and molecular parameters of the zeaxanthin monomer.⁴⁵ As previously noted, this routine uses the time-dependent picture as described by Lee and Heller to model the potential energy surfaces and calculate absorption and resonance Raman excitation profiles.^{2, 26, 45, 46} We will use this model to determine the broadening parameters and dimensionless displacements of the zeaxanthin monomer by comparison with the experimental absorption profile and resonance Raman excitation profiles.

The J1 and J2 aggregates were modeled as a dimer of identical monomers.³² The interaction integral between the constituent monomers are either determined through the point dipole approximation (PDA) or the extended dipole model (EDM). The vibronic eigenstates are calculated by diagonalizing a matrix of transition dipole-coupled harmonic oscillators of the constituent monomers. A matrix of the dipole operator elements are used to calculate the absorption profile, while the Raman tensors are calculated to generate the resonance Raman excitation profiles and depolarization ratios. Along with the parameters that were included in the monomeric routine, geometric parameters such as distance between monomers and the orientation of the monomers are also considered.

Given that the oscillator strength of the zeaxanthin monomer is largely conserved in the J1 and J2 aggregates, we can expect the optimized transition dipole lengths of J1 and J2 to be similar to this value.

Determination of transition dipole moments

The transition dipole moment of zeaxanthin is an important value needed to optimize the remaining parameters. This value will be even more important in the aggregate modeling, as the interaction energy from both the PDA and EDM depend on μ . The transition dipole moment, μ , is proportional to the integrated area of the molar absorption divided by the frequency, $\varepsilon(\omega)/\omega$, as shown in the expression ⁶¹

$$|\mu|^2 = \frac{2.303(1000 \text{ cm}^3 \text{ L}^{-1})3\hbar cn\varepsilon_0}{\pi N_A} \int \frac{\varepsilon(\omega)}{\omega} d\omega \quad \text{Eq 2.6a}$$

$$|\mu|^2 = 9.18 \times 10^{-3} n \int \frac{\varepsilon(\omega)}{\omega} d\omega \quad \text{Eq 2.6b}$$

where n is the index of refraction of the solvent. Using this expression and the integrated experimental absorption data from 14000 – 29000 cm^{-1} and $n = 1.36$ for ethanol, we can estimate that the transition dipole moment is 3.78 eÅ. This value will be used as the initial transition dipole moment value for zeaxanthin.

2.5.5 Zeaxanthin monomer calculated absorption profiles and REPs

The calculated monomer absorption profile matches the experimental profile very well (**Figure 2.7a**). Slight deviations occur at the high energy and low energy

edges of the spectrum. The high-energy tail is accurate for the absorption state – the experimental profile includes contributions from additional electronic states such as *cis*-zeaxanthin or $S_0 \rightarrow S_n$ absorbance, which are not included in the simulation. The computational broadening on the low-energy side is unexpected. We would expect a more narrow calculated absorption spectrum, as many of the low-frequency modes, ($<800 \text{ cm}^{-1}$) are not included in the simulation.²⁵ As shown in **Figure 2.7b**, the calculated RREPs of the 9 Raman transitions show very good agreement with the experimental values. Optimized electronic and molecular parameters are shown in **Table 2.4**. The total vibrational reorganization energy is defined as

$$\lambda_{vib} = \frac{1}{2} \sum_i \omega_i \Delta_i^2 \quad \text{Eq. 2.7}$$

where ω is the frequency of the vibrational mode and Δ is the dimensionless displacement. The vibrational reorganization energy is the energy difference of the chromophore in a ground state versus relaxed excited-state geometry, both determined on the electronic excited state potential energy surface.⁶²

RREP analysis of carotenoid monomers has been extensively studied in the past, and a range of values for the broadening parameters and dimensionless displacements have been reported to model the absorption and resonance Raman excitation profiles.⁶³⁻⁶⁷ The optimized values that are reported here for zeaxanthin agree with the reported dimensionless displacements and broadening parameters of other carotenoids, supporting not only the method by which the absorption and resonance Raman excitation profiles are calculated, but the determined absolute

Raman cross sections as well. Additionally, the optimized transition dipole moment was found to be the same as the experimentally determined value for β -carotene further lending support for our computational results.

Table 2.4: Spectroscopic parameters for the zeaxanthin monomer and aggregates

Parameter	Mon	J1	J2	H
Electronic zero-zero energy (cm ⁻¹)	20730	19450	19270	19570
Homogeneous Broadening (cm ⁻¹)	280	375	460	452
Inhomogeneous Broadening (cm ⁻¹)	360	175	260	671
Electronic Transition Dipole Moment (eÅ)	3.86	3.54	3.54	2.69
θ (dipole vector to distance vector angle)	N/A	90	90	90 / 90
ϕ (overlay angle)	N/A	43	84.8	0
R(ab) (Distance between chromophores) (Å)	N/A	11.4 (PDA)	5.9 (PDA)	0.51 (EDM) 5.2 (PDA)
Dipole-dipole Coupling strength (cm ⁻¹)	N/A	725	660	6175
Dimensionless displacement				
Δ_4	0.32	.32	0.32	0.12
Δ_3	0.56	.56	0.56	0.22
Δ_2	0.95	0.95	0.95	0.49
Δ_1	1.11	1.11	1.11	0.60
Total vibrational reorganization energy (cm ⁻¹)	1670	1670	1670	440
Folder name [for in-house organization purposes]	a	b	c	d

a – mon_reduced_u; b –

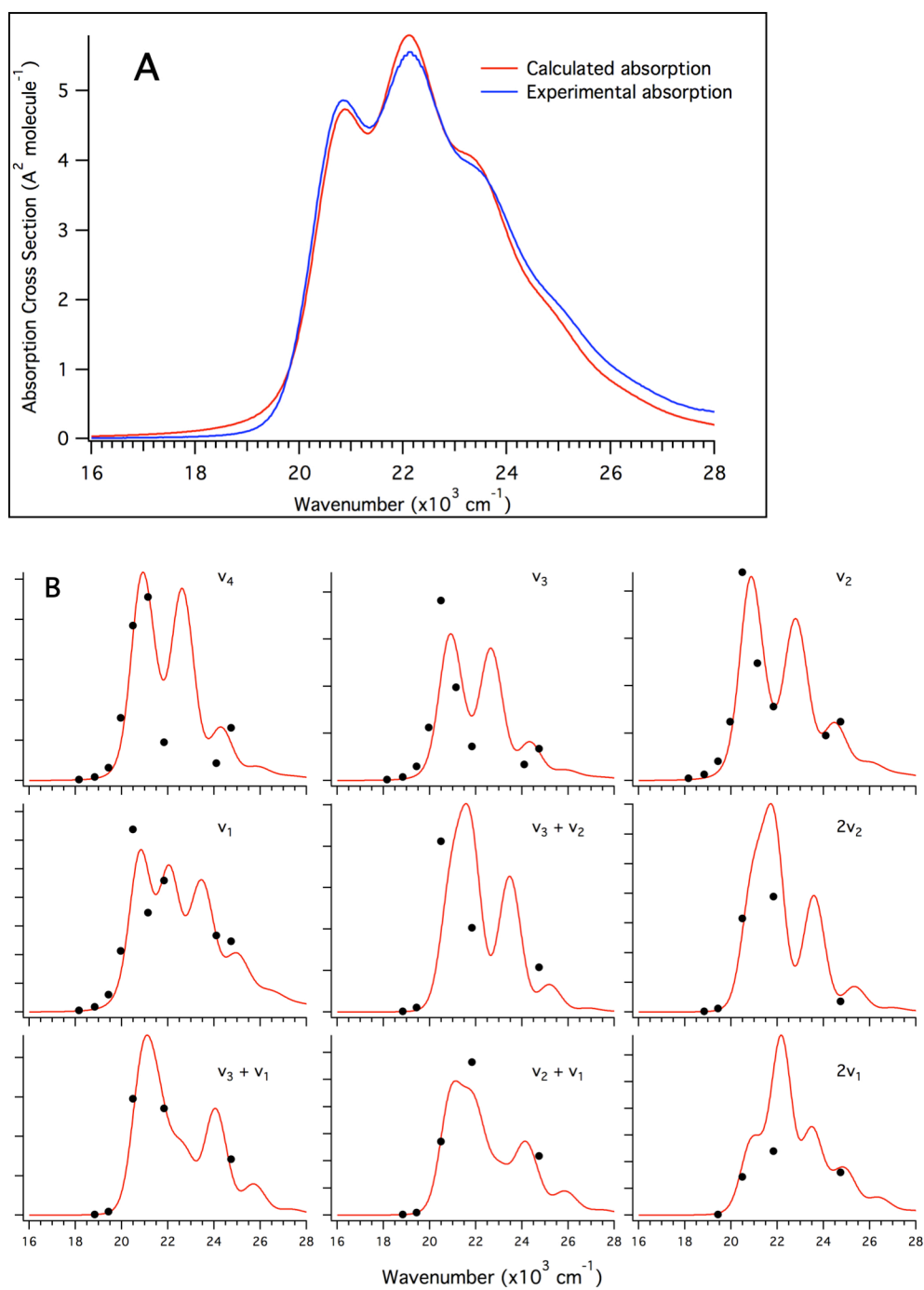


Figure 2.7: (A) Experimental (blue) and calculated (red) absorption spectra for the zeaxanthin monomer. (B) Experimental (black dots) and calculated (red trace) resonance Raman excitation profiles for the zeaxanthin monomer. Parameters that lead to these fits are summarized in **Table 2.4**.

2.5.6 J1 and J2 aggregate calculated absorption and REPs.

As the experimental absorption profiles of J1 and J2 aggregates are very similar, it was expected that the interactions between each chromophore in the aggregates would be similar as well. To reduce the degrees of freedom that require optimization, the slip angles were held at 90° while the rotation angle, ϕ , and the center-to-center distance were optimized. The calculated J1 aggregate fits to the experimental absorption, RREPs, and depolarization ratios are shown in **Figures 2.8a-c**. The calculated J2 aggregate fits to the experimental absorption, RREPs, and depolarization ratios are shown in **Figures 2.9a-c**. The optimized parameters are shown in **Table 2.4**.

Optimized molecular and electronic parameters.

The optimized geometric parameters of both J1 and J2 indicate a weakly coupled h-type interaction between zeaxanthin monomers. With the point dipole approximation, the optimized geometry of the J1 aggregate has a rotation angle of 43° and a R_{AB} of 11.4\AA . In contrast, the J2 aggregate has a optimized geometry with a rotation angle of $\sim 85^\circ$ and a R_{AB} of 5.9\AA . The J_{12} values of J1 and J2 are 725 cm^{-1} and 660 cm^{-1} , respectively.

As with the monomer program, the electronic zero-zero, E_{00} is determined for the J1 and J2 aggregates with the dimer model. However, the optimized value is affected by additional factors, such as nonresonant intermolecular interactions (gas-to-crystal shift).⁴¹ The greater polarizability of zeaxanthin relative to solvent molecules is

the origin of the shifts for these aggregates. The gas-to-crystal shift can be quantified as following: $D = E_{00,\text{mon}} - E_{00,\text{agg}}$, where $E_{00,\text{mon}}$ and $E_{00,\text{agg}}$ are the optimized E_{00} for the monomer and aggregate, respectively. We report in the present study a gas-to-crystal shift of $\sim 1280 \text{ cm}^{-1}$ for the J1-aggregate and $\sim 1460 \text{ cm}^{-1}$ for the J2-aggregate. These shifts contribute to the overall redshift observed in the absorption spectra of the aggregates compared to the monomer.

Both J1 and J2 have significantly larger homogeneous broadening than the monomer, as expected for a exciton-coupled system. The broadening is enhanced by some phonon interactions or intermolecular vibronic coupling, where the excitation can be shared with a variety of neighboring molecules. The inhomogeneous broadening is significantly smaller for J1 and J2 than the monomer, indicating a more ordered environment.²⁵ J2 has a larger value of both homogeneous and inhomogeneous broadening than J1.

Within an excitonically coupled system, we would expect that the vibrational displacements on a per-molecule basis would be lower than the monomer. Therefore, the Δs were constrained to be equal to or less than the optimized monomer values. An unexpected result with for J1 aggregate is that the best fit happens to be found when the Δs are approximately equal or even slightly larger than those found for the monomer results (data not shown).

J1 Calculated absorption profiles, rREPs, and depolarization ratios.

The qualitative fit of the calculated absorption profile of J1 has close agreement with the experimental profile. Although the spacings between the prominent vibronic peaks in the calculated absorption profile of 0-1 to 0-2 are significantly less than experimental the experimental spacing, the relative magnitudes of each of those peaks are very similar to the experimental profile.

The positions of the peaks and troughs for the experimental and calculated fundamental RREPs are very similar. The relative amplitudes also agree, but show greater deviation for the lower frequency (and less intense) modes, possibly due to experimental uncertainty. The overtone and combination bands show good agreement at all measured wavelengths except 404.3 nm. Nearly all of the experimental 404.3 nm cross sections are twice as large as the calculated values. The 404.3 nm excitation approaches the $S_0 \rightarrow S_n$ transition of zeaxanthin, possibly indicating that the additional Raman activity is related to the overlap of the $S_0 \rightarrow S_n$ and $S_0 \rightarrow S_2$ absorption bands. The calculated depolarization ratio profile shown in **Figure 2.8b** is specific to the ν_1 Raman line. The calculated depolarization ratio does not agree well with the experimental results, being significantly higher than at all examined excitation wavelengths.

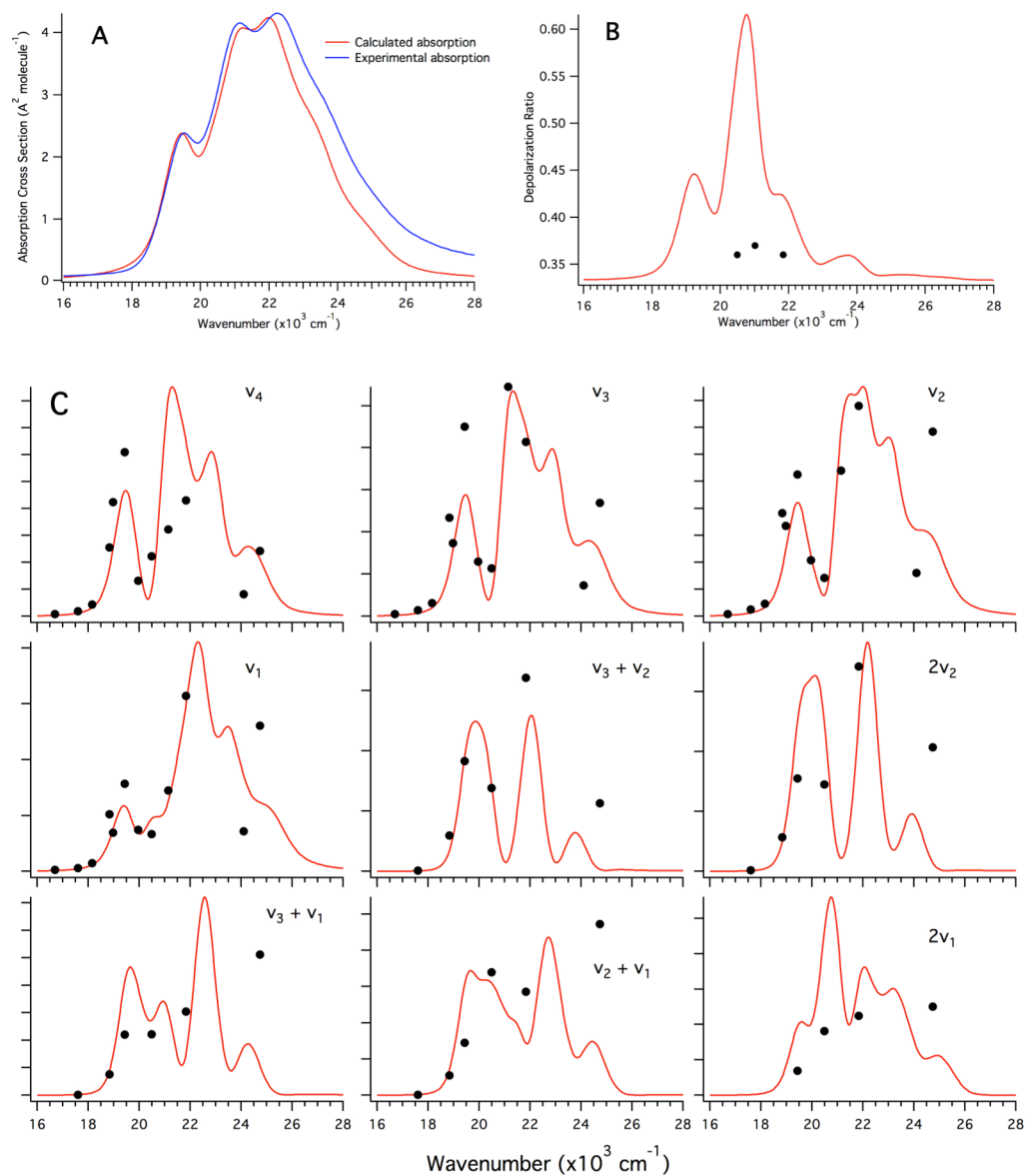


Figure 2.8: (A) calculated and experimental absorption spectra of the J1 aggregate. (B) calculated and experimental (black dots) depolarization ratios. (C) experimental (black dots) and calculated (red trace) resonance Raman excitation profiles for the zeaxanthin J1 aggregate. Parameters that lead to these fits are summarized in **Table 2.4**.

J2 Calculated absorption, resonance Raman excitation, and depolarization ratios.

As is shown in **Figure 2.9a**, the calculated absorption profile accurately captures the intensities, shape, and spacing of the 0-0 and the 0-1 experimental bands. However, as with the J1 aggregate, the spacing between the 0-1 and 0-2 are poorly represented. As expected for a simple dimer model, the absorption profile does not fit well to the red tail. Although the mechanism for the red-tail is largely unknown, it has been attributed to long range intermolecular interactions or lattice vibrations.¹⁷

The calculated rREPs for the J2 aggregate match well for both the fundamental and combination/overtone bands. The calculated depolarization ratios of J2 corresponding to the best fit for the absorption profile and rREPs deviates significantly from the experimental values. As discussed in **section 2.5.3**, the experimental depolarization ratios for the J2 aggregate are significantly lower than the theoretical lower limit of $\rho = 0.33$ for a dimer with parallel or antiparallel transition dipoles.

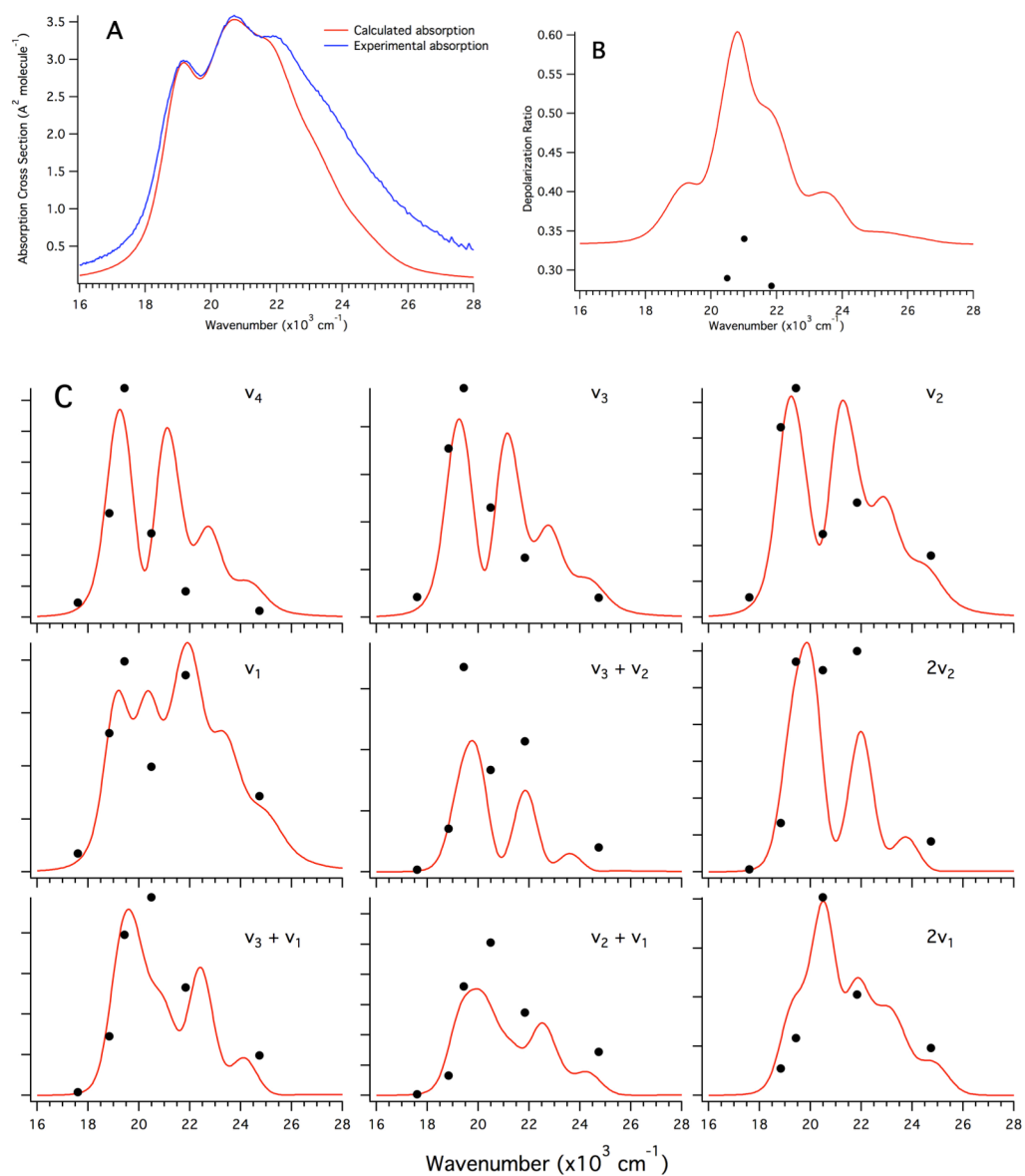


Figure 2.9: (A) calculated and experimental absorption spectra of the J2 aggregate. (B) calculated and experimental (black dots) depolarization ratios. (C) experimental (black dots) and calculated (red trace) resonance Raman excitation profiles for the zeaxanthin J1 aggregate. Parameters that lead to these fits are summarized in **Table 2.4**.

2.5.7 H-aggregate calculated absorption and resonance Raman profiles

As was recently published, the strongly-coupled H-aggregate is believed to contain a subpopulation of weakly coupled constituents which are most likely J1 or J2 type in nature.¹⁷ Therefore, we did not attempt to fit the entire H-aggregate absorption or resonance Raman excitation profiles, as the program is only designed to model the interaction between one pair of molecules. The fitting routine was constrained to fit only the region between 24700 - 27500 cm^{-1} as this region is believed to be primarily occupied by the H-band transition. The calculated absorption profile and rREPs are shown in **Figures 2.10a-b**.

The H-aggregate was fit to a perfect card-stacked dimer, with $\theta_A = \theta_B = 90^\circ$ and $\phi = 0^\circ$. However, an impossibly small separation of 0.51 Å was determined when using the extended dipole moment, whereas the expected distance for a π stacked system is about 3.5 Å. Fitting with the point dipole approximation yields a center-center separation of 5.2 Å. Additionally, the inhomogeneous broadening is much larger than the other aggregates and monomer. The determined dimensionless displacements for the ν_1 and ν_2 modes of the H aggregate are approximately half as large as the monomer, J1, and J2 aggregate optimized values while the ν_3 and ν_4 modes exhibit a ~ 3 fold decrease in the displacement. Therefore, the total vibrational reorganization energy for the H aggregate is much lower than the monomer, J1 aggregate, and J2 aggregates.

The H-aggregate exhibits hypochromism relative to the zeaxanthin monomer, with a relative oscillator strengths 70% that of the monomer.¹⁷ However, as the H-band only comprises about 75% of the oscillator strength of the H-aggregate, the optimized transition dipole is necessarily a smaller 2.69 eÅ. The $\sim 5000\text{ cm}^{-1}$ blue-shift of the absorption band is captured by the optimized fit: the determined E_{00} is at 19570 cm^{-1} , which includes a 1080 cm^{-1} gas-to-crystal shift. The calculated J_{12} of 6200 cm^{-1} puts the position of the calculated absorption band at $\sim 5000\text{ cm}^{-1}$ blue-shifted from the monomeric E_{00} .

Within the region that the H-aggregate was fit, there is very good agreement between the calculated and experimental absorption profiles. However, most of the experimental resonance Raman cross-sections were acquired at too long a wavelength to accurately test the fit. The calculated overtone and combination bands are much lower than the experimental Raman cross sections. As expected, the red tail of the H-aggregate is not modeled at all by the calculated absorption or resonance Raman excitation profiles.

As the geometry of the dimer is of a perfect H-type interaction, the depolarization ratios of all modes at all wavelengths will be 0.33. Experimentally, there are excitation wavelengths where the depolarization ratios were found to be significantly different from 0.33, but were all found in the red-tail which is thought to be made of the weakly-coupled H-type interactions.

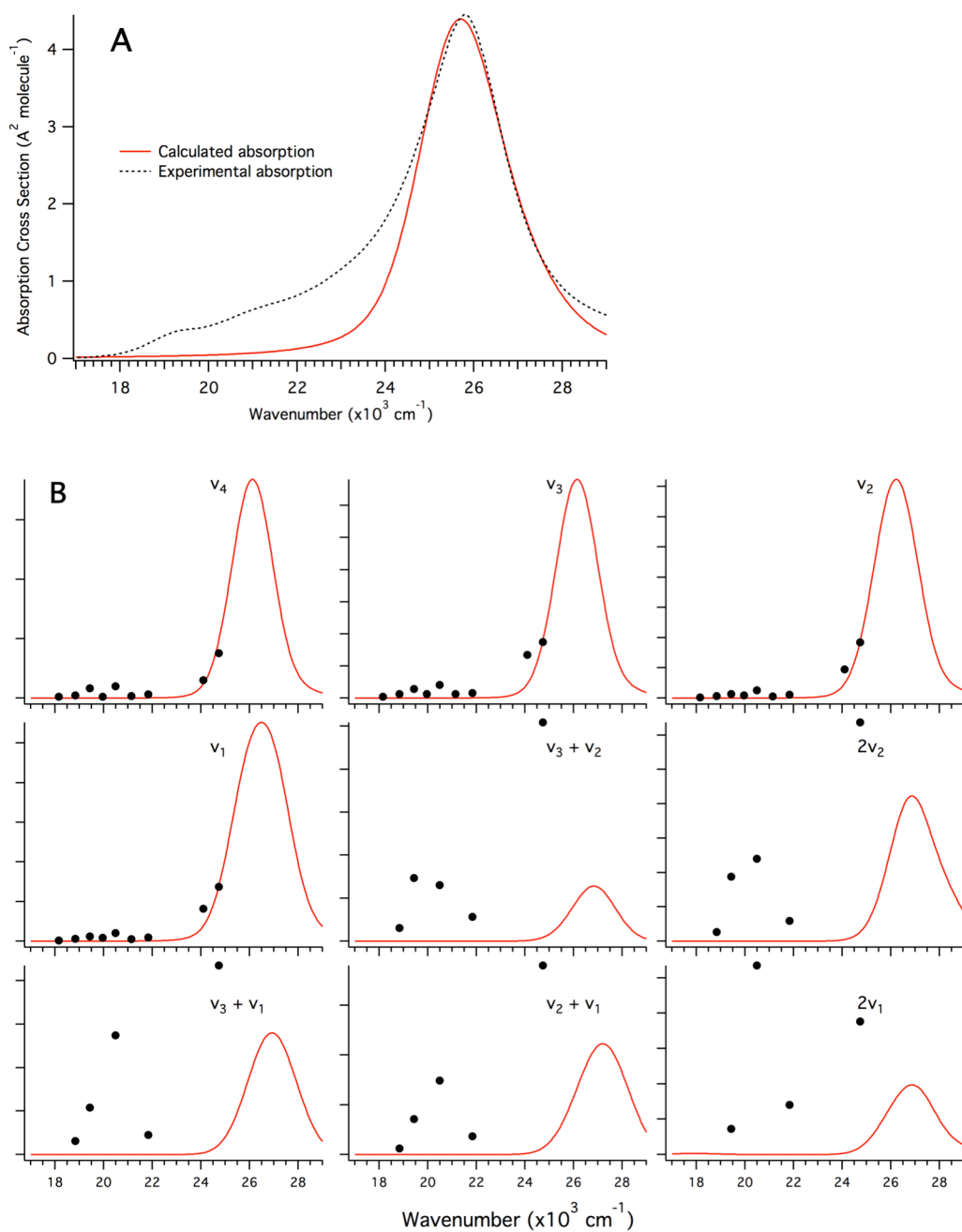


Figure 2.10: (A) The calculated absorption profile of the H aggregate with the extended dipole model (red) compared with the experimental absorption profile (black dashes). (B) Experimental (black dots) and calculated (red trace) resonance Raman excitation profiles for the zeaxanthin H aggregate. Parameters that lead to these fits are summarized in Table 2.4.

A common classification of the extent of exciton-coupling is the relative magnitudes of the free exciton bandwidth (W), which is described as $2J_{12}$, relative to the total vibrational reorganization energy (λ_{vib}). The strength of the exciton-coupling can be broken down into three regimes: weakly-coupled ($W \ll \lambda_{vib}$), intermediately-coupled ($W \approx \lambda_{vib}$), and strongly-coupled ($W \gg \lambda_{vib}$).⁴¹ According to these designations, both the J1 and J2 aggregates can be described as weakly-coupled H-aggregates and the H-aggregate is well within the realm of a strongly-coupled H-type interaction.

2.6 Discussion

2.6.1 overview

Zeaxanthin has the propensity to form three different types of aggregates in aqueous binary solvent systems. Each aggregate has a distinct absorption spectrum despite having nearly identical vibrational frequencies as measured by resonance Raman spectroscopy.¹⁷ The absorption spectra, resonance Raman intensities, and Raman depolarization ratios were analyzed for the zeaxanthin monomer and aggregates with the aim of constraining the arrangements of the constituent monomers. The raw spectroscopic data of the zeaxanthin monomer, J1 aggregate, J2 aggregate, and H aggregate were used to determine various molecular, geometric and electronic parameters of those specific entities including broadening parameters and vibrational displacements. These parameters were optimized by finding the most closely fitting absorption, resonance Raman excitation, and depolarization ratio profiles.^{32, 46}

The J1, J2, and H zeaxanthin aggregates have been previously described as H-type aggregates of varying strengths.¹⁷ Here, these aggregates were modeled as an excitonically coupled dimers in an attempt to understand correlation between coupling strength and aggregate geometry. The optimized geometry of the J1 and H aggregates is consistent with a weakly-coupled and strongly-coupled card-stacked interaction, respectively. Although the J2-aggregate was fit to a nearly monomeric geometry, there is a slight H-type quality, as indicated by the positive J_{12} value. The three different cases of the J1, J2, and H-aggregate reinforce and expand upon the differences between each aggregate as discussed in the previous report, and illustrate the limitations of the dimer model.¹⁷ In addition, advantages of the extended dipole model of the point dipole approximation have been suggested: These points will be discussed below.

2.6.2 Conclusions from experimental RREPs

The absorption and Raman cross-sections of fundamental modes are dependent on the Franck-Condon (FC) factors, or the overlap between the ground and excited potential surfaces. FC factors are dependent on the magnitude of the dimensionless displacement and the frequency of the fundamental mode. The intensities of combination modes, modes with vibrational quanta in multiple vibrational states, are proportional to the products of the FC factors for each constituent vibrational state.⁶⁸ As discussed before, exciton-coupling between in an aggregate distorts the excited state, resulting in a splitting of the excited electronic state into a higher and lower energy-state. Depending on the summed transition dipoles of each constituent

monomer in the aggregate, the upper and lower energy states will have different relative strengths. Each split state will have its own FC manifold for absorption and Raman processes. Additionally, as the exciton is among multiple chromophores, the vibrational displacements and total vibrational reorganizational energy is expected to decrease.^{28, 69}

The RREPs among the four fundamental modes are very similar for each zeaxanthin species. Regions of greatest absorption do not always correspond to the regions of greatest Raman intensity. Particularly for the J1 and J2 modes, the 0→1 transition has a surprising lack of Raman intensity when the excitation is near the peak of the absorption profile. As noted for the J1 and J2 aggregates, the overtone/combination bands exhibit different excitation profiles depending on whether the band receives contribution from the ν_1 mode. The bands without contribution from ν_1 have a similar excitation profile as the fundamental modes. Each of these results can be explained as due to the overlap of the excited state with the final Raman state, which would be shifted and weighted depending on the magnitude and nature of the net transition dipole. These points will be addressed further while comparing the optimized vibrational displacements, geometries, and calculated profiles with the experimental data.

2.6.3 Conclusions from experimental depolarization ratios

Within the probed region, the monomer depolarization ratios are consistent with the fact that only a single electronic transition, $S_0 \rightarrow S_2$, is active. There are

several mechanisms that can cause the depolarization ratios to depart from the typical monomeric value of 0.33 for a resonant transition to a single electronic state. The first mechanism, which is the greatest interest to this study, is the distortion due to multiple electronic states coexisting in the same energy level, which could be caused by exciton-coupling. The second mechanism is a distortion of the structure of the molecule, which could change the symmetry of the molecule and thus the polarizability tensors.

As was discussed previously, within the dimer model, perfect H-type ($\theta_A = \theta_B = 90^\circ$ and $\phi = 0^\circ$) and or J-type ($\theta_A = \theta_B$ and $\phi = 0^\circ$) interactions would only give rise to a single allowed electronic state. Thus the resonance Raman depolarization ratios would be indistinguishable from the monomer, equal to 1/3. Any other orientation, with the exception of orientations where the dipole vectors are perpendicular to each other, will result in a deviated ρ value.^{32, 70, 71} Therefore, it is likely that overlapping electronic bands caused by exciton-coupling are a primary contributor to the depolarization ratio dispersion.

Additionally, the magnitude of depolarization ratio dispersion is dependent in part to the magnitude of the interaction energy, where stronger interactions between chromophores results is a deviation from 0.33, indicating that the zeaxanthin crystal and the H-aggregate have greater intermolecular interactions than the J1 and J2 aggregate. The depolarization ratio distortion observed for the H-aggregate is likely not due to exciton-coupling of the H-band interaction, but rather the overlapping electronic bands of the weakly-coupled H-type interactions that make up the red tail.

For molecules where the transition dipole moment is along a single molecule axis, such as zeaxanthin and β -carotene, we would only expect a non-zero value for one of the Raman tensors, yielding a depolarization ratio of $\rho = 1/3$ for the polarized bands and $\rho = 3/4$ for the unpolarized bands. Molecules with higher symmetry, such as porphyrins (D_{4h}), have $\rho = 1/8$ and $\rho = 3/4$ for polarized and unpolarized bands, respectively.^{72, 73} Lowering of symmetry from packing or aggregation effects can cause significant deviations from the ideal values, as in the case of porphyrin dimers.⁶⁰ However, there very little changes in the resonance Raman spectra between the J1 and J2 aggregates, meaning that the molecular structure of the zeaxanthin molecules in these aggregates are very similar.

2.6.4 Structural differences between J1 and J2 aggregates

With the constraints placed on the geometries of the aggregates and modeled as dimers, the primary differences between the J1 and J2 aggregates can be explained by a increase in the rotation angle, ϕ , and a decrease in the distance between the chromophores. The spectral changes of the dimer with the changes in geometry have similarities to what is observed with the previously reported change in temperature of the J1 aggregate.¹⁷ The figure is reproduced in the supplementary information. With an increase in temperature, there is a permanent decrease in the 0-2 band and an increase in the 0-0 band relative to the 0-1 band, which was previously described as an annealing of the aggregate. These results suggest that the annealing is characterized by

a decrease in the distance between each chromophore and an increase in the rotation angle.

2.6.5 Computational results for the zeaxanthin aggregates

The magnitudes of the interaction energies for the J1 and J2 aggregates are consistent with weakly coupled h-type interactions. As the ratio of the 0-0 and 0-1 is directly dependent on the strength of the exciton-coupling, with a decrease in the ratio with an increase of the exciton-coupling.⁴¹ From the experimental absorption spectra of the J1 and J2 aggregates, we would expect that the interaction of the J1 aggregate is greater than that of the J2 aggregate. This is properly represented by the optimized parameters, as the calculated interaction energies are 725 (J1) and 660 (J2) cm^{-1} .

The determined geometry for the J1 aggregate is consistent with a weakly-coupled H-type interaction, and a relatively small $|J_{12}|$ term of 725 cm^{-1} . In contrast, the determined geometry of the J2 aggregate is ambiguous in their designation as clearly H or J type interactions. In fact, the transition dipoles are nearly perpendicular to one another, which decreases the dipole-dipole interaction and generates a result very similar to the monomer spectra. However, although the transition dipoles are nearly perpendicular, the calculated J_{12} is still similar to that of J1, which exemplifies the inaccuracies of the PDA. It was previously suggested that the point dipole model only be used when the distance between the molecules exceeds the length of the molecules, which is not the case for these optimized structures.⁶⁹ However, the results gained with the point dipole approximation are very good despite a strange geometry

and the calculated absorption spectra follows the experimental profile very well, without sacrificing much agreement between the calculated and experimental rREPs. The extent by which the point dipole succeeds while the extended dipole fails may be insightful into the true structure of the J2-aggregate and is still under investigation. The dimer model only accounts for a single type of interaction, and in the aggregate, it would only be suitable for situations where the constituent molecules are translationally equivalent, such as in the case for a one-molecule per unit cell picture.⁷⁴ If however, the reality of the aggregate is more similar to the two-molecule per unit cell, where alternating molecules are translationally equivalent, then the dimer model would be expected to fail.

Several solutions may be suggested to remedy the situation. First of all, if the J2-aggregate is accurately represented by a two-molecule per unit cell lattice, then it is possible that two sets of dimer interactions may accurately encompass the J2 absorption. Additionally, the model of exciton interactions may also be improved. Although the extended dipole model is significantly better than the point dipole approximation according relative to quantum-mechanical calculations,⁵⁸ another improvement, which would not significantly increase computational time, would be the line-dipole approximation.⁵⁹

The fitted J1 and J2 aggregates have very similar homogeneous and inhomogeneous broadening. The homogeneous broadening is larger for the aggregates than the monomer, possibly due to additional exciton/phonon-interactions or lattice vibrations that are not accounted for in the calculations.⁷⁵ Lifetime broadening cannot

account for a significant broadening difference between the J1, J2 and monomer. The monomeric S_2 lifetime is ~ 200 fs (26 cm^{-1} lifetime broadening), while ~ 300 fs (20 cm^{-1} lifetime broadening) for the J1 and J2 aggregates, which corresponds to $\sim 6 \text{ cm}^{-1}$ decrease in lifetime broadening between the monomer and aggregates.²⁰ The inhomogeneous broadening is smaller for the J1 and J2 aggregates than the monomer, indicating a more ordered structure. The optimized broadening values of the H aggregate are noteworthy, namely because of the extremely large σ value, despite a similar value for Γ . In consideration of the entire aggregate, with both the strongly coupled H-type interactions and the weakly-coupled H-type interactions, it would be expected that the inhomogeneous broadening parameters would be very large for the H-aggregate, as the H-aggregate is largely inhomogeneous.

For the zeaxanthin J1 and J2 aggregates, the dimensionless displacements are, for the most part, conserved or slightly lower than that of the monomer. The conservation of Δs is consistent with the fact that molecular aggregates are Frenkel excitons, and the intramolecular properties of the excited state remain although the exciton-coupling extends over a number of molecules.^{76,77} This result also supports our assertion that the zeaxanthin J1 aggregate is in reality, *weakly-coupled* H-type aggregates.^{17,41} This assertion was also made for the J2 aggregate, but the ambiguous geometric results presented here prevent a final classification at this time.

Within the strongly-coupled regime we would expect the exciton to be delocalized over many molecules, spreading the vibrational displacements between them. Leng and coworkers have shown that merocyanine dye dimer vibrational

displacements are decreased by a factor of $\sqrt{2}$ relative to the monomer, as the intramolecular distortions are spread equally between the two constituent monomers.⁶⁹ However, within the weakly-coupled system, the vibrational displacements are largely restricted to the single molecule, such as indicated for the resonance Raman analysis of aggregated porphyrin diacids.^{60, 78} With these points in mind, we can also conclude that the exciton is delocalized between several molecules in the H-aggregate. First of all, the vibrational displacements are between 2-3 fold smaller for the H-aggregate than for the zeaxanthin monomer. Second, the optimized distance between chromophores for the H-aggregate was calculated to be an impossible $\sim 0.5\text{\AA}$. This result can be interpreted as the level of coupling is impossible to obtain between only two molecules, and thus the coupling must include the contribution for multiple other neighbors. From this information, we can expect that the exciton is spread between at least 4 neighboring zeaxanthin molecules.

2.6.5 Conclusions

The present study has been primarily motivated by our interest in determining the electronic, vibrational, and geometric characteristics of carotenoid aggregates. We have reaffirmed, through modeling the aggregates as a excitonically-coupled dimer, that the J1 and H aggregates are both defined by H-type interactions of varying strengths, as indicated by the geometry and change in the vibrational displacement. The J2 aggregate was fit very poorly to the dimer model, indicating that either the J2 aggregate is more complex than can be expressed as a dimer, or that the method of

calculating the dipole-dipole interaction is not sufficiently accurate to accurately represent the J2 aggregate. These results motivate expansion of the interaction energy calculation to the line-dipole approximation and the development of a two-molecule per unit cell lattice model.

This chapter in part is currently being prepared for submission for publication of the material. Berg, Christopher J.; Tauber, Michael J. The thesis author was the primary investigator and author of this material.

2.7 Appendices

2.7.1 Calculation of external standard Raman cross-section ($\sigma_{\text{Ram,R}}$)

Known absolute Raman cross-sections of the external standard are used to fit **Eq. 2.3** to determine values for K , v_e , and C . The determined values for K , v_e , and C are shown in the **Table 2.A1**.

Table 2.A1: Experimental and literature values for EtOH Raman cross sections

Raman line	Differential Raman cross section ($10^{-30} \text{ cm}^2 \text{ molecule}^{-1} \text{ sr}^{-1}$)					K ($10^{-27} \text{ cm}^2 \text{ molecule}^{-1} \text{ sr}^{-1}$)	v_e (10^4 cm^{-1})	C (10^{-11} cm^2)
	337.1 nm^1	415 nm^3	488.0 nm^2	514.5 nm^1	550 nm^3			
884 cm^{-1}	12.9	4.99	2.27	1.82	1.34	16.3	14.31	-4.037
2900 cm^{-1}	223	--	35.0	27.6	--	7.62	8.614	-6.093

¹ Taken from Abe and Ito (1978)

² Extrapolation from 514.5 nm differential raman cross section using a $v_L(v_L - v_S)^3$ correction, where v_L is the frequency of the laser line and v_S is the frequency of the Raman line.

³ These cross section values were determined through comparison with the 3400 cm^{-1} water -OH band.

\

2.7.2 Comparison of the J1 and J2 UV-Vis results with an integrating sphere.

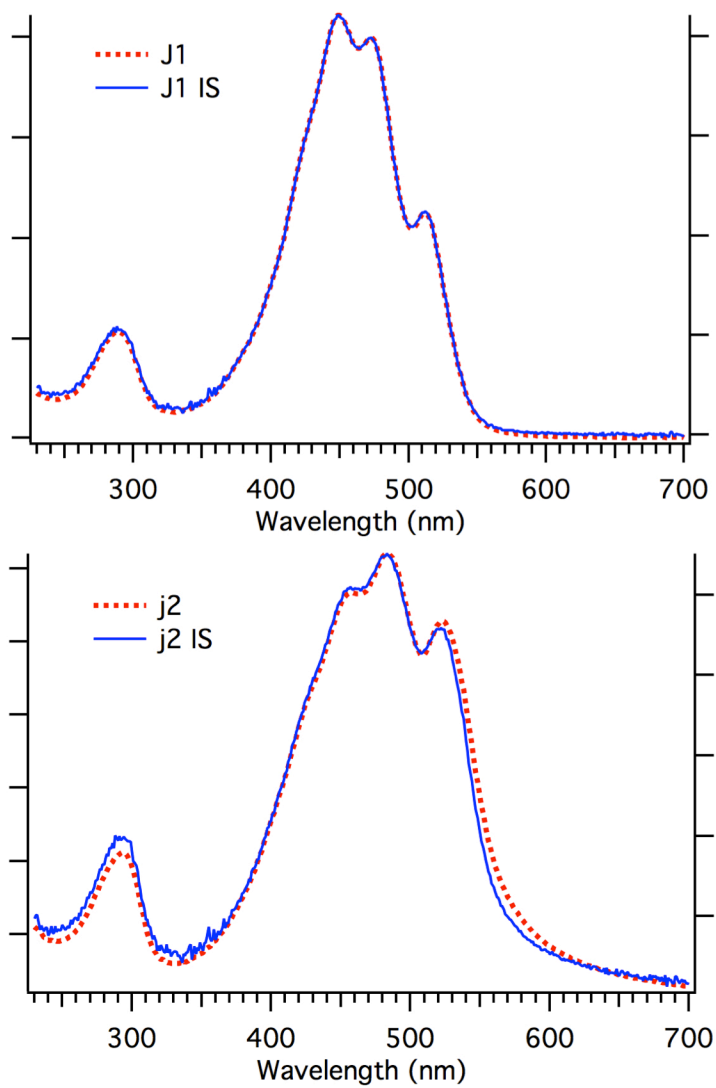


Figure 2.A1: Comparison of the J1 and J2 absorption spectra measured with (blue lines) and without (red dashes) the ISR-3100 integrating sphere.

As shown in **Figure 2.A1**, the measured absorption spectra of the J1 aggregate did not change with the use of the integrating sphere. However, the J2 showed a slight

decrease in absorption in the 500-600 nm region, indicating that there was some scattering effects.

2.7.3 The different fits for the J1 aggregate

Several different J1 fits are shown in **Table 2.A2**. J1-PDA and J1-ED were optimized unconstrained. As the delta values are greater than the monomeric values, these cannot be realistic. Also shown is the J2 aggregate fit with the extended dipole model, which is not shown in the main chapter, but shown in **section 2.7.3**.

Table 2.A2: Spectroscopic parameters for the zeaxanthin J1 and J2 aggregate fits

Parameter	J1-PDA	J1-ED	J1-PDA2	J1-ED2	J2-ED
Electronic zero-zero energy (cm ⁻¹)	19434	19437	19433	19433	19170
Homogeneous Broadening (cm ⁻¹)	450.0	450	375	375	500
Inhomogeneous Broadening (cm ⁻¹)	245.0	246	2	200	230
Electronic Transition Dipole Moment (eÅ)	3.74	3.71	3.54	3.54	3.42
θ (dipole vector to distance vector angle)	61.1	59	100/64	100,64	55
φ (overlay angle)	29.8	32	11	11	85
R(ab) (Distance between chromophores) (Å)	8.57	4.295	12.7	4.3	4.0
Dipole-dipole Coupling strength (cm ⁻¹)	511	560	725	722	124
Dimensionless displacement					
Δ ₄	0.329	.32	0.29	.29	.29
Δ ₃	.599	.635	0.56	.56	.66
Δ ₂	1.029	1.02	0.95	0.95	0.99
Δ ₁	1.189	1.15	1.11	1.11	1.04
Total vibrational reorganization energy (cm ⁻¹)	1920	1870	1656	1656	1650
Foldername [for in-house organization purposes]	a	b	c	d	e
PDA: a -- J1(4mode,auto_6,4quanta)2; c -- J1_opt11_4q_2; ED: b -- j1_opt9_4q_1; d -- j1_opt10_4q_2; e -- J2_opt8_4q_1					

2.7.4 The effect of geometry on the absorption spectra of the J2 and H aggregates

– Proof for ‘best’ fits.

The largest difficulty against the point dipole and the extended dipole models is that, for the J2 aggregate, it is difficult to get both a good match on both the spacing and relative intensities of the vibronic bands. This is largely due to the fact that the

magnitude and weights of each exciton band is dependent on both the dot product between the two vectors and the magnitude of the interaction energy. As these two quantities are not correlated to each other, there are situations where a perfect match is not possible for both the spacing and the relative intensities. We will explore in this appendix the effect of changing different aspects of the dimer configuration: distance between centers (R_{AB}), overlay angle (ϕ), and slip angle (θ). We will use two parameter sets that failed to fit the J2-aggregate well. We will also show the effect of changing the R_{AB} values for the H-aggregate, showing the need for the optimized 0.5Å.

As can be seen from **Figure 2.A2**, within the angle ranges, there was no position where the vibronic band positions were close to the experimental values. It should also be noted that the simultaneous agreement in the ratios of the bands are not possible, if the 0-0 band decreases, the 0-2 band increases and vice versa. Additional tests were conducted by varying the distance from 2-6Å. However, due to the negligible exciton-coupling from the $\phi = 85^\circ$ and $\theta = 55^\circ$, there was virtually no change in the absorption spectra a closer or further R_{AB} values.

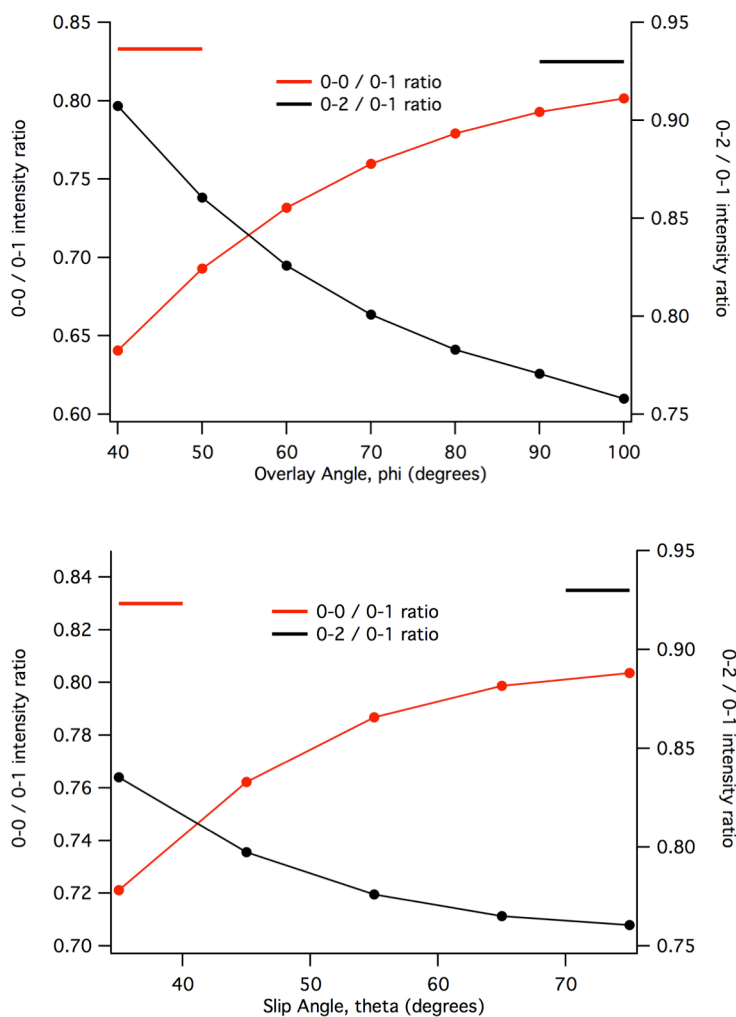


Figure 2.A2: This graph shows change of the ratios of the 0-0/0-1 and 0-2/0-1 intensities of the fitted J2 aggregate as a function of the overlay angle, ϕ (top), or slip angle, θ (bottom). The experimental ratios are shown in bolded lines at .83 for the 0-0/0-1 ratio and .93 for the 0-2/0-1 ratio. The parameter set is J2-ED (Table 2.A4).

For illustrative purposes, the J2 aggregate was also fit to a intermediately coupled J-type interaction, and the same manipulation of geometric parameters was conducted. Figure 2.A2 shows the absorption spectra of the J2-J aggregate. The J2-J fit was specifically designed to fit the intensity ratio of the 0-0 and 0-1 bands, which are nearly perfectly matched. However, the peak positions of the 0-1 bands for the

experimental and calculated spectra are $\sim 300 \text{ cm}^{-1}$ different. As can be seen in Figure 2.A3, either the 0-0 / 0-1 ratio *or* the 0-2 / 0-1 ratio may be achieved at any given geometry, but never both at the same time.

From the comparison of these two results, it is clear that for the J2 aggregate, there are no geometries where both intensity ratios can be satisfied. Therefore, we are forced to conclude that either the dimer model does not accurately account for the interactions of the J2 aggregate, or that the method of calculating the interaction energy is not accurate enough for this system.

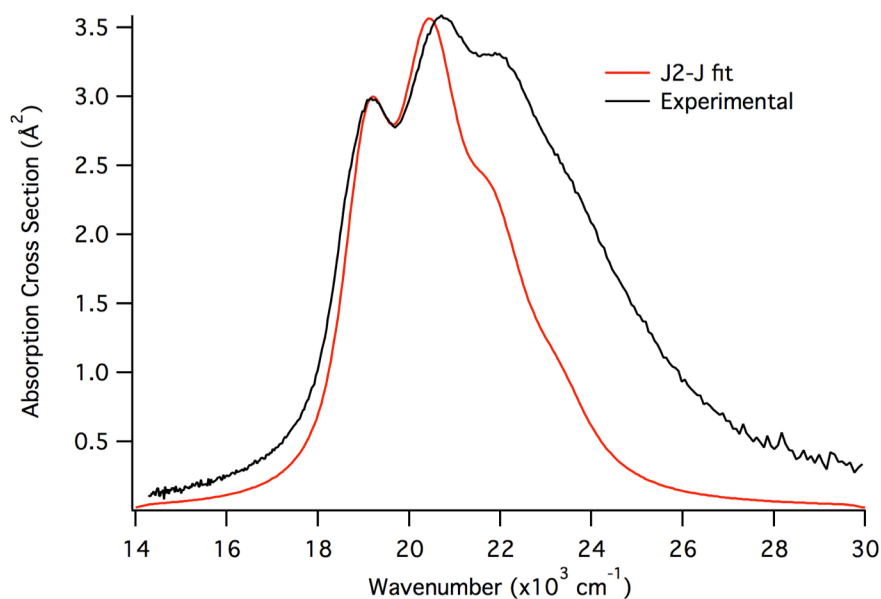


Figure 2.A3: Absorption spectra of the J2-J fit. The parameters used for this fit are as follows: $\theta = 5^\circ$; $\phi = 0^\circ$; $E_{00} = 19470 \text{ cm}^{-1}$; $\Gamma = 500 \text{ cm}^{-1}$; $\sigma = 250 \text{ cm}^{-1}$; $\mu = 3.52 \text{ e}\text{\AA}$; $R_{AB} = 23\text{\AA}$; $\Delta_4 = 0.40$; $\Delta_3 = 0.68$; $\Delta_2 = 1.12$; $\Delta_1 = 1.40$

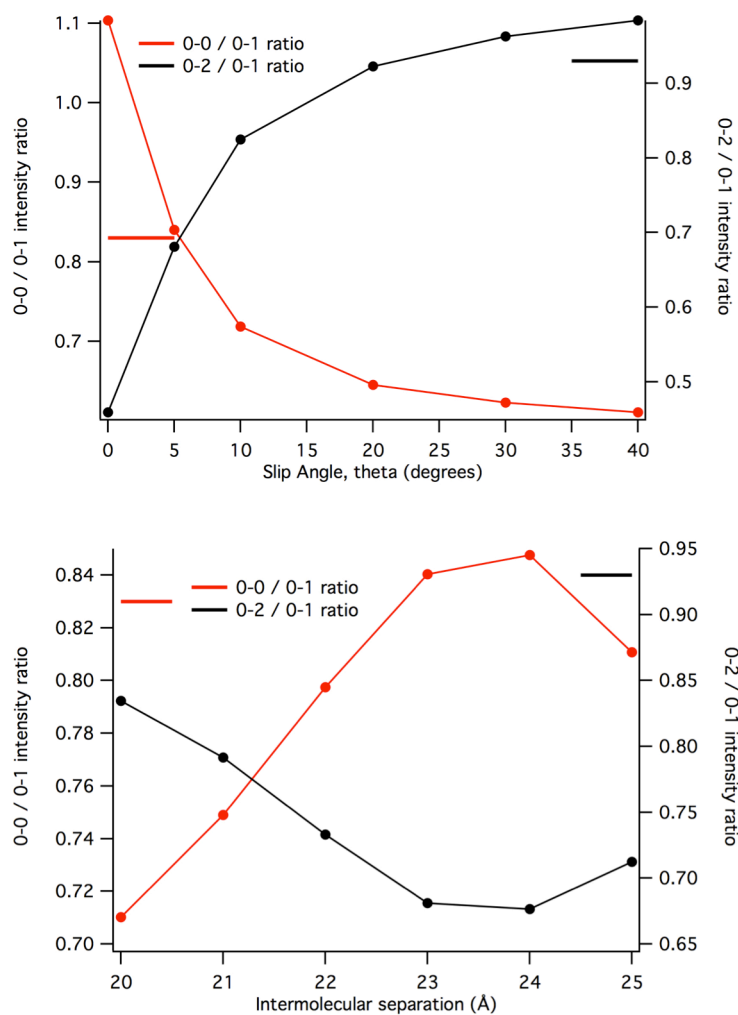


Figure 2.A4: This graph shows change of the ratios of the 0-0/0-1 and 0-2/0-1 intensities of the fitted J2-J aggregate as a function of the slip angle, θ (top), or intermolecular separation, R_{AB} (bottom). The experimental ratios are shown in bolded lines at .83 for the 0-0/0-1 ratio and .93 for the 0-2/0-1 ratio. The parameter set is J2-J. (See **Figure 2.A3**).

In contrast to the J2 aggregate, the H aggregate was fit to a unrealistic, but well-matching fit. The necessity of the impossibly small R_{AB} values is proved in **Figure 2.A5**. The other geometric, electronic, and vibrational parameters are as described in **Table 2.4**.

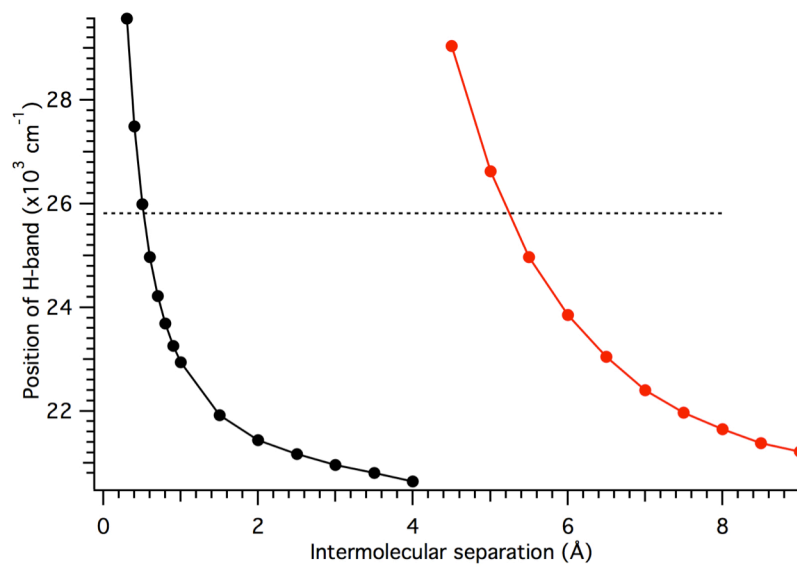


Figure 2.A5: Position of the H-band as a function of the intermolecular separation using the extended dipole model (black) and the point dipole approximation (red). The experimental position of the H-band is designated as the dotted line at 25820 cm^{-1} .

3. Vibrational and electronic spectroscopy of rhodoxanthin in avian plumage, solid-state films, and solutions

3.1 Abstract

Carotenoids are some of the most abundant and colorful natural pigments in nature. In this study, we will examine four fruit doves (*Ptilinopus*) and a cotinga (Cotingidae), which have been thought to contain the retro-carotenoid, rhodoxanthin, as the primary carotenoid. Through extraction and subsequent purification by HPLC analysis, it was verified that the four fruit doves only contained rhodoxanthin while ~95% of the carotenoids in the cotinga are rhodoxanthin, the rest of which is lutein. Using Kubelka-Munk analysis and the ‘pile of plates’ methodology, absorption profiles were generated from diffuse reflectance and transmittance spectra and a redshift in the absorption profile was coincident with the change in feather color. Through resonance Raman spectroscopy it was observed that the ν_1 frequency correlated with the shift in absorption profiles. Comparison of solution-phase rhodoxanthin resonance Raman and absorption results of the 6E6`E, 6E6`Z, and 6Z6`Z rhodoxanthin isomers suggests that isomeric effects are not a primary contributor to the spectral shifts. Several mechanisms in concert, such as distortion, polarization, and exciton-coupling, likely contribute to the shifts in absorption. Additionally, low-irradiance resonance Raman spectroscopy is shown to be a viable alternative to resonance Raman microscope spectroscopy when the sample is prone to photo-degradation or photo-alteration.

3.2 Introduction

There are over 25 different carotenoids that have been identified within bird feathers,⁴ with colors ranging from yellow to red. These carotenoids are either directly acquired by the bird through diet or by metabolism of other dietary carotenoids.^{79, 80} While other pigments such as melanin and photonic structures⁸¹ contribute to the beauty and bright colors associated with many birds, carotenoids, with their strong absorptivity and natural abundance in the environment, are responsible for the most vibrant displays. The importance of avian carotenoid coloration is vast, associated with signaling and sexual communication, as concentration of carotenoids are an honest signal for fitness.^{6, 82} As carotenoids are obtained solely through diet, concentration of carotenoids within the bird is subject to many factors including availability in the environment, the ability of the bird to forage, and the overall health of the bird.⁶ Additionally, new carotenoids may be observed in a bird population when a novel carotenoid is introduced via a new food source.^{83, 84}

Relatively rare in birds is the retro-carotenoid rhodoxanthin, which has 14 conjugated double bonds including two carbonyl groups in the C(3) and C(3') position. Until recently, it was thought that rhodoxanthin was only obtained through diet and deposited unmodified into the feathers.⁷⁹ However, there has been recent evidence to support the endogenous metabolism of rhodoxanthin from other dietary carotenoids, most notably zeaxanthin and lutein, in some bird species.^{79, 80}

In this study we have purified and isolated the carotenoids of four fruit pigeons in the genus *Ptilinopus* within the Columbidae family: *Pt. magnificus*, *Pt. pulchellus*,

Pt. solomonensis, and *Pt. jambu*. These birds were previously thought to contain rhodoxanthin as the primary carotenoid pigment despite a wide range of colors in their plumage.⁸⁵ For comparison, the bright red plumage from a specimen of *Phoenicircus carnifex* in the Cotingidae family, which has been long known to contain rhodoxanthin as the principle pigment, was also analyzed.^{80, 85} The variation of feather color, despite similar carotenoid composition, has been a topic of strong interest in canthaxanthin-containing birds⁸ and finches⁷.

There are various mechanisms by which the vibrational and electronic structure of the chromophore can be changed, including perturbations caused by a protein environment, such as structural distortion,^{86, 87} hydrogen bonding,⁸⁸ or charge polarization⁸⁸⁻⁹¹. Alternatively, electronic interactions between neighboring carotenoid molecules could play a role.^{7, 8} Similar questions have arisen with carotenoids in the carotenoproteins of crustaceans.^{10, 90, 92}

Resonance Raman spectroscopy is a useful technique to selectively amplify the vibrational signatures of a strongly absorbing chromophore by choosing an excitation wavelength that coincides with the electronic absorption band. Thus, resonance Raman spectroscopy is a perfect tool for analyzing, *in situ*, samples such as feathers or crustacean and mollusk carapaces that only contain a single strongly absorbing chromophore.^{9, 93} Raman is particularly sensitive to the geometric configuration and distortion of the molecule, allowing for the correlation of geometric and electronic structure. To the best of our knowledge, we report the first resonance Raman spectra of a retro-carotenoid.

Reflectance spectra are commonly used in the study of bird plumage⁹⁴. One shortcoming is that a reflectance spectrum is insufficient to distinguish the portion of an attenuation coefficient that is due to absorption versus that is due to scattering.^{Cordon, 2007 #32793} For the present study, a central aim has been the correlation of electronic absorption spectra and resonance Raman vibrational spectra of rhodoxanthin, particularly where both spectra are acquired *in situ*. Therefore, the isolation of the absorption component is important. We have acquired both the diffuse transmittance and the diffuse reflectance spectra of feathers from each species of bird and the combination of the two spectra allowed us to derive absorption and scattering spectra using the ‘pile-of-plates’ model.^{95,96} This model is an extension of the widely-known Kubelka-Munk model.⁹⁷

Resonance Raman spectra were acquired using both micro- and macro- Raman systems, and at room and low-temperature. The Raman spectra of rhodoxanthin acquired *in situ* are compared with spectra of the molecule in solution and in thin solid films. The vibrational spectra are compared with the electronic spectra, and discussed in the context of various possible mechanisms that can cause color variation in the plumage of each species. Differences in the resonance Raman spectra of the feathers, solution-phase rhodoxanthin, and rhodoxanthin thin-films are analyzed in context of normal mode calculations

3.3 Methods and Materials

3.3.1 Pigment extraction and analysis

The feathers of this study were obtained from the Kansas Museum of Natural History (Kansas University, Lawrence, KS, USA) and the Yale Peabody Museum of Natural History (Yale University, New Haven, CT, USA). The five feather types are described as follows: (1) red body feathers of a male *Phoenicircus carnifex* (KU 88704, collected March 1997); (2) burgundy breast feathers of a male *Ptilinopus magnificus septentrionalis* (YPM 74482, collected October 1960); (3) crimson breast feathers of a male *Ptilinopus pulchellus pulchellus* (YPM 73164, collected 1955); (4) Purple breast feathers of a male *Ptilinopus solomonensis speciosus* (YPM 41523, collected November 1937); and (5) Pink breast feathers of a male *Ptilinopus jambu* (YPM 62797, collected October 1952). Pictures of the five birds featured in this chapter are shown in **Figure 3.1**

The carotenoids were extracted from the feathers following procedures described previously.^{98,99} Cleaned feathers were soaked in acidified pyridine at 90 °C for several hours. The acidified pyridine was then washed with methyl *tert*-butyl ether (MTBE)/Water (3:1 v/v). The *Pt. solomonensis*, *Pt. magnificus* and *Pt. pulchellus* feathers were each soaked in the acidified pyridene for 3 hours. The feathers of *Pt. solomonensis* were white at the end of this treatment; however, the feathers of *Pt. magnificus* and *Pt. pulchellus* were dark brown. The soaking of *Pt. jambu* feathers was stopped after 2 hours, at which time the feathers also appeared white. *Ph. carnifex* feathers were pale orange after extraction. The feather extracts in the MTBE layer of

the wash were next analyzed by HPLC and absorption spectroscopy as described previously. McGraw, 2005 #316} Pigments eluting from the HPLC were collected and dried under a gentle stream of nitrogen gas. The pigments were then redissolved in methanol (HPLC grade, Fisher Scientific) and their absorption spectra were recorded. The pigments from *Pt. magnificus* were sufficiently concentrated for mass spectrometry, which was performed in the APCI mode (Applied Biosystems API 2000). The samples were dissolved in methanol and introduced into the mass spectrometer by direct infusion at a rate of 20 $\mu\text{L}/\text{min}$.

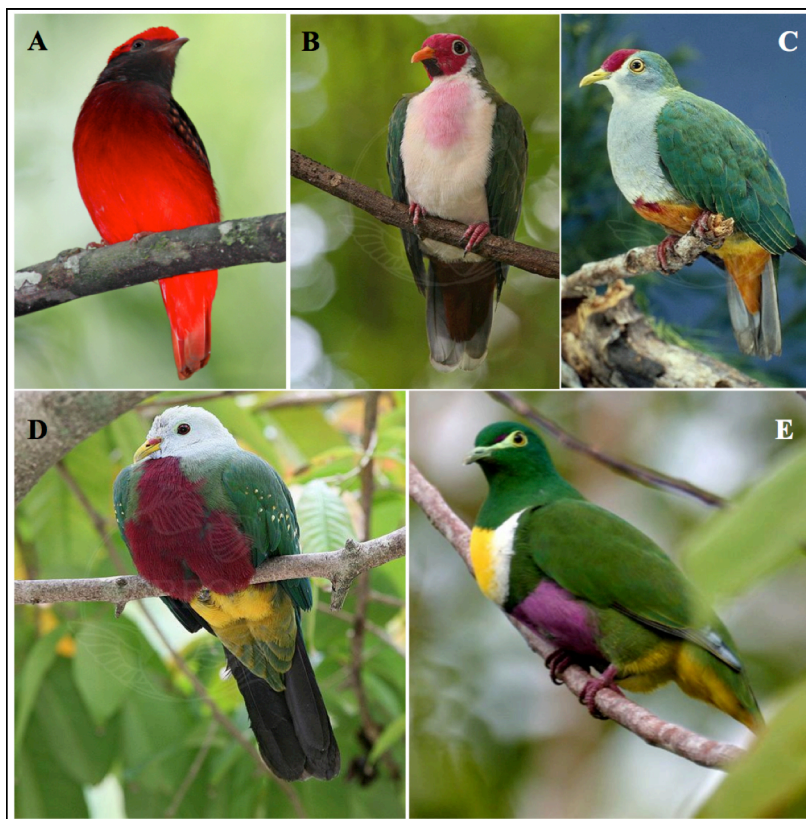


Figure 3.1: Pictures of rhodoxanthin-containing birds. (A) *Phoenicircus carnifex* (B) *Ptilinopus jambu* (C) *Ptilinopus pulchellus* (D) *Ptilinopus magnificus* (E) *Ptilinopus solomonensis*

3.3.2 Preparation of rhodoxanthin isomers

Three isomers of rhodoxanthin, 6-cis, 6'-cis (6Z6'Z); 6-trans, 6'-cis (6E6'Z); and 6-trans, 6'-trans (6E6'E) configurations were prepared by heating a solution of synthetic rhodoxanthin dissolved in acidified pyridine to a temperature of 90 °C. The isomers were then separated by normal-phase HPLC and identified by comparison of the absorption spectra with those previously published.¹⁰⁰ The molecular structures of each rhodoxanthin isomer are shown in **Figure 3.2**.

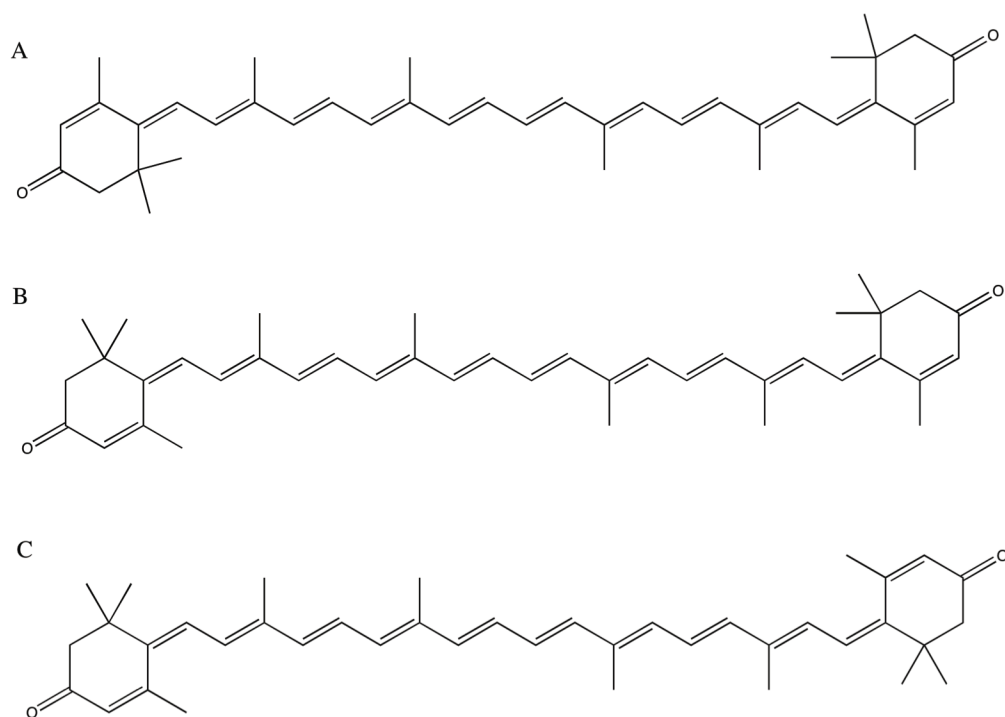


Figure 3.2: Chemical structures of A) 6-trans,6'-trans rhodoxanthin, B) 6-trans,6'-cis rhodoxanthin, C) 6-cis,6'-cis rhodoxanthin

3.3.3 Thin-film preparation

Three thin-films of the (6E,6'E), (6E,6'Z), and (6Z,6'Z) isomers were prepared from the synthetic rhodoxanthin treated with acidified pyridine. The dried rhodoxanthin was dissolved in acetone and added drop-wise to a glass microscope slide, with sufficient time between each drop to allow the solvent to evaporate.

3.3.4 Microscopy

Images of the five rhodoxanthin-containing feathers were acquired with a CCD camera (AVT Stingray F-201B/C) attached to an upright microscope (Zeiss Axio Imager). The feathers were epi-illuminated with light from a quartz tungsten halogen lamp. The objective was a NA=0.25 plan semi-apochromat (Zeiss Epiplan-Neofluar 10x). A diffuse white reflector (Spectralon) was used to perform a color balance calibration. After the calibration, each feather was placed on the Spectralon block for the acquisition of an image.

3.3.5 Spectroscopy

Absorption Spectroscopy. UV-vis absorption spectra of the samples were measured with scanning spectrometers (Shimadzu, UV-3600, or Varian Cary 50). Samples were held in a quartz cuvette with 1 cm path length, unless otherwise noted.

Reflectance, and Transmittance Spectroscopy. Reflectance and transmittance data was collected with a UV-Vis spectrophotometer with an integrating sphere attachment (Shimadzu UV-3600 with ISR-3100 attachment) A diagram showing the

experimental setup for reflectance and transmittance is shown in **Figure 3.3**. Diffuse reflectance and diffuse transmittance measurements were collected for the five-rhodoxanthin containing feathers. For both reflectance and transmittance experiments, a baseline correction was performed with barium sulfate prior to sample measurements. The feathers were positioned so that the most colorful region of the feather was probed.

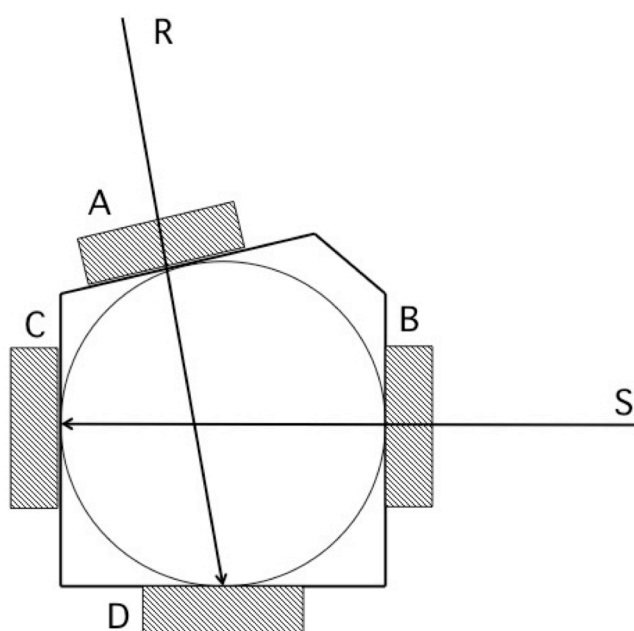


Figure 3.3: Diagram of the ISR-3100 integrating sphere. For diffuse reflectance measurements, C contains feather over non-reflective surface, D contains barium sulfate plate, A and B contain nothing. For diffuse transmittance measurements, B contains feather, A and C contain nothing, and D contains barium sulfate plate. In all cases non-reflective black masks with a 3.0 mm diameter aperture were used at both reference and sample positions for greater specificity.

The absorption and scattering coefficient profiles for the feathers were calculated using Kubelka-Munk theory and the pile of plates model.^{97, 101, 102 96} We assume that feathers are single layer with two parallel surfaces that can either transmit

or reflect light. The diffuse reflectance and transmittance are denoted as r and t , respectively. r and t are related to the Stokes parameters in the following way⁹⁵

$$a = \frac{1 + r^2 - t^2 + \Delta}{2r} \quad \text{Eq. 3.1} \quad \text{and} \quad b = \frac{1 - r^2 + t^2 + \Delta}{2t} \quad \text{Eq. 3.2}$$

where

$$\Delta^2 = (1 + r + t)(1 + r - t)(1 + t - r)(1 - r - t) \quad \text{Eq. 3.3}$$

The Stokes parameters are directly related to the absorption (K) and scattering (S) coefficients.

$$K = \frac{a - 1}{a + 1} \log b \quad \text{Eq. 3.4}$$

$$S = \frac{2a}{a^2 - 1} \log b \quad \text{Eq. 3.5}$$

K/S is known as the remission function, $F(R)$, and is therefore equal to

$$F(R) = \frac{K}{S} = \frac{(1 - a^{-1})^2}{2a^{-1}} \quad \text{Eq. 3.6}$$

Where a^{-1} is the absolute reflectance of a completely non-transmitting (infinitely thick) sample. A more thorough derivation is contained in the *Supplementary information* (Appendix).

Macro Resonance Raman Spectroscopy. 514.5 and 568.2 nm excitation beams were generated by an Argon/Krypton ion laser (Laser Innovations, Innova-70C). The

beam was directed through a narrow-band interference filter (Semrock) that matched the wavelength of the laser line.

For the solid-state samples, a 180 – degree geometry was used to collect the scattering from the sample. A 75 mm cylindrical lens was used to increase the dimensions of the laser spot at the plane of the sample to 2.50 x 0.40 mm, reducing the irradiance at the focus. The excitation power was below 1.5 mW. For solution-phase experiments, the sample was held in a 10 mm x 4 mm septum-capped quartz cuvette. The rhodoxanthin solution was constantly purged and agitated with a steady stream of N₂ gas. As with the solid-state experiments, a 75 mm cylindrical lens was used to reduce irradiance and focus the beam at the sample point to dimensions of 1.25 x 0.040 mm, with the shortest dimension parallel to the spectrograph slit. Scattered light was collected at 90° relative to the excitation beam. Excitation power was approximately 4.5 mW.

For the solution-phase Raman experiments, the rhodoxanthin isomers were each dissolved in dimethyl sulfoxide (DMSO). DMSO was selected for three reasons: carotenoids have good solubility in DMSO, the solvent has a high boiling point and therefore evaporates relatively slowly when purged, and the Raman bands of the solvent do not overlap with the carotenoid hydrogen-out-of-plane (HOOP) bands.

A F/1.2 camera lens (Canon FD, focal length 85 mm) and F/4 achromatic lens were used to collect and focus the scattered light into a 320 mm focal length spectrograph (Horiba Jobin-Yvon, iHr-320) equipped with 1200 and 2400

grooves/mm holographic gratings and an open-electrode CCD detector (Horiba Jobin-Yvon Synapse) The scattered light passed through a polarization scrambler (Opto-Sigma) and an edge filter (cutoff either 514.5 or 568.2 nm, Semrock, Razoredge).

Micro Resonance Raman Spectroscopy. The same laser source, filters, and spectrograph were utilized as with the macro-Raman experiments. The beam was directed into a Zeiss Axio-Imager upright microscope modified with beamsplitters appropriate for routing the laser beam to the objective, and for transmitting the Raman-scattered light efficiently. The excitation was focused onto the sample with a NA=0.55 objective lens (Zeiss LD EC Epiplan-Neofluar 50x). Scattered light was collected with the same lens, and subsequently directed along a path that included a polarization scrambler and an edge filter that was selected for the excitation wavelength (Semrock, Razoredge), and focused into the spectrograph slit. The laser spot size was measured to be approximately 1 μm in diameter, and consequently, the irradiance was $\sim 10^5$ -fold higher when compared with spectra acquired with the macro-Raman system at equal power. To reduce degradation of the thin film and feather samples, excitation powers were kept below 50 and 200 μW , respectively. We will refer to spectra gathered with Raman microscope as ‘high-irradiance’, as the irradiance levels are between 6400 - 25600 W/cm^2 .

Low-temperature micro-resonance Raman spectroscopy. A Linkam THMS600 microscope stage was employed to lower the temperature of the feathers to near liquid N_2 temperatures. For the feathers, a barb was cut from the main feather and placed between two glass coverslips. A thin layer of silicon oil was used to adhere the

coverslips together, as well as adhere the coverslip to the cooling block. All spectra were acquired with the sample in a vacuum. The temperature probe on the cold block indicated the temperature was -195°C for all samples. For the low temperature resonance Raman studies of the thin film of 6Z6'Z, the microscope slide was placed inside a Linkam LTS420 cooling stage and subsequently cooled until the temperature probe on the cold block read -195° . Excitation powers were kept below $300\ \mu\text{W}$.

The 2400 grooves/mm grating was employed for nearly all spectra, except the solution-phase experiment, where the 1200 grooves/mm grating was used. The slit-width varied between 0.030 – 0.100 mm, and depended upon whether resolution or system throughput was most important. Spectral resolution is approximately $3\ \text{cm}^{-1}$ with 2400 grooves / mm grating and 0.050 mm slit width and approximately $6\ \text{cm}^{-1}$ with 1200 grooves / mm grating and 0.050 mm slit width. A summary of experimental conditions is contained in **Table 3.1**.

Table 3.1: Summary of experimental Resonance Raman parameters

Rhodoxanthin Sample, and experiment	Raman system	Excitation	Grating (groove/m m)	Slit width (mm)	Power (mW)
Thin films (6E,6'E);(6E,6'Z);(6Z,6'Z) (Room temp.)	Microscope (180-degree)	514.5 nm High-irrad.	2400	0.050	0.050
Feathers (Room temp.)	Microscope (180-degree)	514.5 nm High-irrad.	2400	0.030	0.17-.20
Feathers (Low temp.)	Microscope (180-degree)	514.5 nm High-irrad.	2400	0.050	.20-.30
Thin film (6Z,6'Z) (Low-temp.)	Microscope (180-degree)	514.5 nm High-irrad.	2400	0.050	.20-.30
Thin films (6E,6'E); (6E,6'Z) (Room temp.)	Macro (180-degree)	568.2 nm Low-irrad.	2400	0.100	0.80-1.5
Feathers (Room temp.)	Macro (180-degree)	514.5 nm Low-irrad.	2400	0.100	0.80-1.5
Solution-phase (DMSO) (6E,6'E);(6E,6'Z);(6Z,6'Z) (Room temp.)	Macro (90-degree)	568.2 nm Low-irrad.	1200	0.050	4.5

3.3.6 Rhodoxanthin Photolysis

A bulk photolysis experiment was conducted in order to examine the potential for isomerization of rhodoxanthin during the resonance Raman experiments. The 6-*trans*, 6'-*cis* rhodoxanthin isomer was isolated by preparative HPLC of the extract of a single male *Phoenicircus carnifex* specimen (KU88704)⁸⁰. The sample was then dried under nitrogen gas and redissolved in 13% acetone in hexanes. This solvent mixture was selected because rhodoxanthin shows vibronic structure in hexanes, making shifts in spectra during photolysis more easily discernable. Acetone was added for increased solubility of rhodoxanthin.

The photolysis experiment was conducted using the 488.0 nm line from an argon ion laser (Spectra Physics Model 164-09). The power and diameter of the laser

beam at the sample were 200 mW and 1 cm. 400 μ L aliquots of the solution containing the rhodoxanthin isomer were placed into two separate 2 mm path length cuvettes, one of which served as a control. Both cuvettes were bubbled with nitrogen gas for 1 min and then capped and sealed with parafilm. The control sample was exposed to dim light throughout the experiment. The absorption spectra of both the laser-illuminated and un-illuminated samples were measured before photolysis and after 5, 10, 15, 20, 25, 30, and 60 min of exposure to the 488.0 nm light. After 60 min, both samples were dried under a gentle stream of nitrogen gas, and then re-dissolved in 14% acetone in hexanes for injection into the HPLC having a normal phase (NP) silica column (Phenomenex Luna 5 μ , 250 x 4.6 mm). The mobile phase protocol consisted of a linear gradient from 10% acetone in hexanes increasing to 20% acetone in hexanes over 40 minutes.

3.3.7 Calculations.

Geometry optimization and normal modes of vibration were calculated with density functional theory (DFT) using Gaussian 09W software.¹⁰³ Initial structures of 6E6`E, 6E6`Z, 6Z6`Z, beta-carotene, and iso-carotene were imported as a ChemDraw structure. The geometry was first optimized with the Hartree-Fock method using the 6-31G(d) basis set. The results were subsequently optimized with DFT using the B3LYP functional and 6-31G(d) basis set followed by a normal mode frequency calculation with the same level of theory. A scaling factor of 0.9614 provided the best agreement between the calculated and experimental frequencies.

3.4 Results

3.4.1 Pigment extraction and analysis

Extraction of the carotenoids from *Pt. magnificus* feathers yielded a deep red solution. HPLC analysis showed three major peaks with retention times of 10, 11.3, and 12.2 min (**Figure 3.4A**). These retention times, along with the absorption spectra (**Figure 3.4B**) in the mobile phase solvent, are the same as purified rhodoxanthin. The peaks eluting at 11.3 and 12.2 minutes were analyzed by mass spectrometry and both were found to have a mass of 562 m/z, consistent with rhodoxanthin. Therefore, it can be concluded that the red coloration of the breast feathers of *Pt. magnificus* arises from the retro-carotenoid rhodoxanthin, which is consistent with previous findings by Volker⁸⁵. Based on the position of the λ_{\max} in the absorption spectra of the three samples in methanol, the isomers can be identified in order of retention time as 6-*cis*, 6'-*cis* (6Z6'Z), 6-*cis*, 6'-*trans* (6Z6'E) (which may also be the symmetric 6-*trans*, 6'-*cis* (6E6'Z) isomer), and 6-*trans*, 6'-*trans* (6E6'E), which have corresponding absorption peaks at 477, 484, and 489 nm, respectively. Isomerization of the carotenoid occurs during the extraction procedure, and therefore the initial presence of the isomers cannot be determined. In addition, based on the brown color of the feathers post-extraction, it can be concluded that an unidentified melanin compound is present.⁹⁹

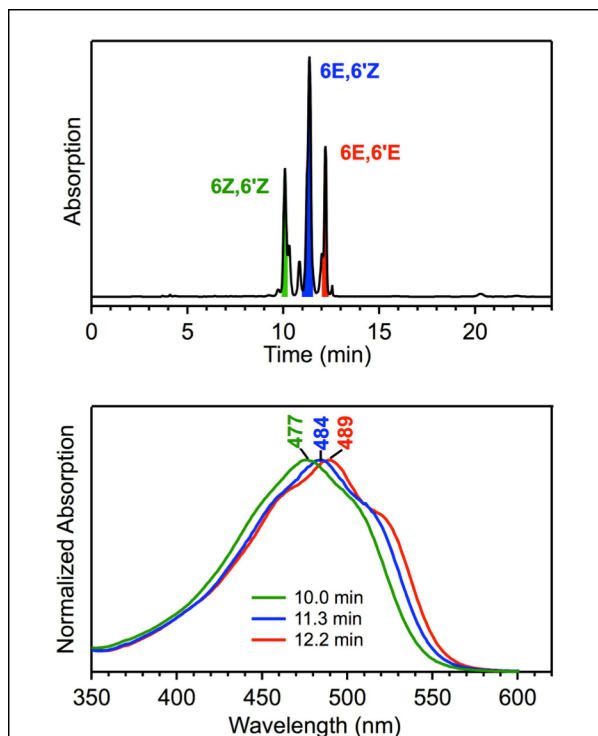


Figure 3.4: (Top) Normal-phase HPLC chromatogram of *Pt. magnificus* feather extract, with detection at 480 nm. (Bottom) absorption spectra of the three major peaks in the mobile phase solvent.

The red breast feathers of *Pt. pulchellus* also remained brown following three hours of extraction, indicating that the red coloration of these feathers arises from a combination of carotenoid and melanin pigments. Conversely, the purple feathers of *Pt. solomonensis* and the pink feathers of *Pt. jambu* both appeared colorless following extraction, indicating a lack of melanin in these feathers. The HPLC chromatograms of the extraction from *Pt. solomonensis*, *Pt. jambu*, and *Pt. pulchellus* feathers yielded three peaks which eluted at approximately the same retention time and had matching absorption spectra to of those from the red *Pt. magnificus* feathers. HPLC chromatograms of the *Ph. carnifex* extract yielded the same three peaks plus an

additional one at 27 min which was verified by mass spectrometry to be all-*trans* lutein (data not shown). However, the amount of lutein is estimated to be less than 5% of total carotenoid in the feather.⁸⁰ Additionally, *Ph. carnifex* remained a pale orange after the extraction process previously reported, suggesting the presence of pheomelanin.¹⁰⁴ Therefore, we conclude that the dominant pigment in all of these feathers is rhodoxanthin.

3.4.2 Optical Microscopy

The barbs and barbules of rhodoxanthin-containing feathers are shown in the microscope images of **Figure 3.5**. The approximate locations probed by Raman spectroscopy (indicated by black circles) were the barbules of the feathers. These brightly-colored regions appear to have the highest concentrations of rhodoxanthin and can be ranked in order of strongest red to strongest purple coloration: *Pt. magnificus* \approx *Ph. carnifex*, *Pt. pulchellus*, *Pt. jambu*, *Pt. solomonensis*. The images of **Figure 3.5** also show various characteristics that were not investigated in depth. First, the barbs of *Pt. pulchellus* and *Pt. magnificus* are dark, which suggests that melanin is more concentrated in this region than in the barbules. By contrast, the feathers of *Ph. carnifex* were the only ones of the study with barbs that appear to have a significant concentration of carotenoid. Second, several feather types showed significant iridescence, suggesting the presence of structural coloration. In general these regions were avoided in the Raman measurements. The overall appearance of *Pt. magnificus* is clearly influenced by the green and purple iridescent structures. The *Pt. solomonensis* feather barbules at the distal end of the rachis are also weakly iridescent (image not

shown). In the case of *Pt. pulchellus*, the distal end of some barbules are weakly iridescent. Third, the images show that the breast feathers of several birds exhibit a color gradient from the base of the rachis to the tip. For *Pt. magnificus*, the color variation is from iridescent green to red; for *Pt. pulchellus*, yellow to bright crimson. Only the reddest regions of these feathers were probed in the present study.

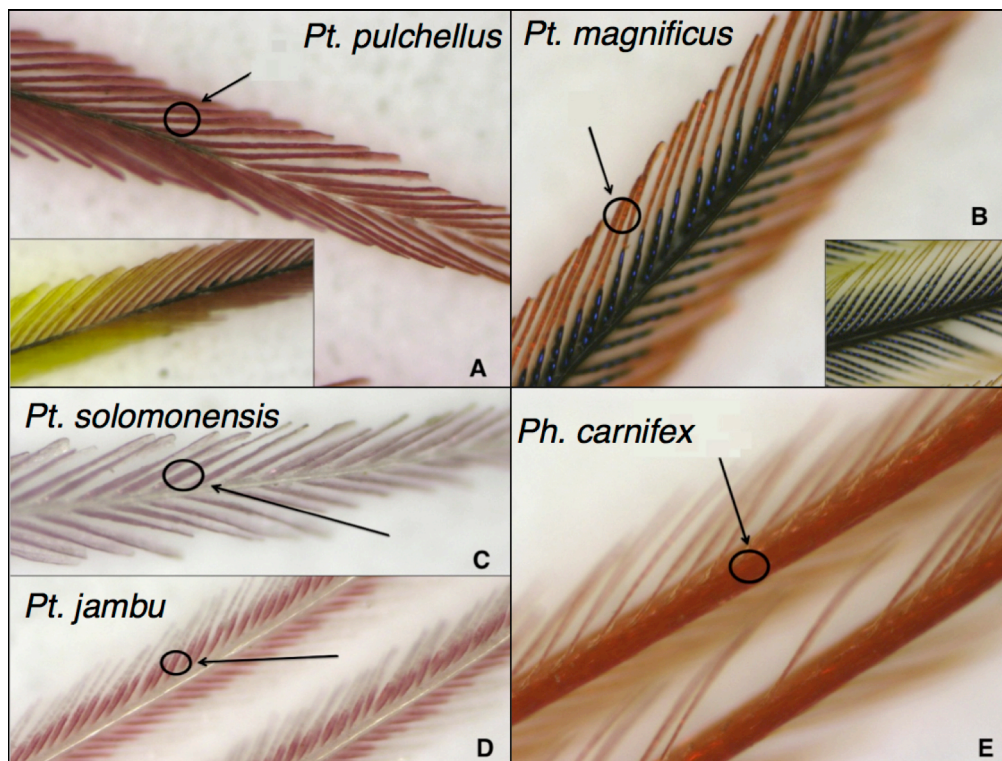


Figure 3.5: Images of five rhodoxanthin-containing feathers (A) Image of the *Pt. pulchellus* feather barb. (Inset) Section of feather barb showing a gradient of yellow to red color. (B) Image of the *P. magnificus* feather barb. (Inset): Approximately half of each barbule is slightly iridescent green, closest to the point of attachment to the barb. (C) Image of the *P. solomonensis* feather barb. (D) Image of the *P. jambu* feather barb. (E) Image of the *P. carnifex* feather barb.

3.4.3 Reflectance Spectroscopy and Kubelka-Munk Analysis

The diffuse reflectance and diffuse transmittance spectra of the five rhodoxanthin-containing feathers are shown in **Figure 3.6**. The absorption of rhodoxanthin causes the diffuse reflectance or transmittance to drop in the range 400-650 nm. The onset of visible absorption on the low-energy (long-wavelength) side is commonly characterized by a reflectance midpoint, $\lambda(R_{mid})$ (alternatively called R_{mid}).^{8,}
¹⁰⁵ The $\lambda(R_{mid})$ value is the wavelength position where the reflectance is midway between a maximum value R_{max} (typically located in the red), and a minimum value R_{min} (in the present case, R_{min} can be found in the region 450-600 nm):

$$\lambda(R_{mid}) = \lambda((R_{min} + R_{max})/2) \text{ Eq. 3.7}$$

We note that the reflectance spectra of *Pt. magnificus* and *Pt. pulchellus* feathers are monotonically increasing in the red portion of our spectra, which prevents an accurate selection of the R_{max} value. The R_{max} values for these feathers are taken to be the reflectance at 725 nm. The $\lambda(R_{mid})$ values are shown in **Table 3.2**.

The characterization of feather pigments by a single parameter $\lambda(R_{mid})$ has some more general shortcomings aside from the specific ambiguity noted above for *Pt. magnificus* and *Pt. pulchellus*. For example, it is expected and observed,^{105, 106} that as pigments reach concentration levels where the reflection approaches low values (saturation), $\lambda(R_{mid})$ values can shift significantly as a function of concentration. Clearly a much better method of characterizing a feather pigment would be the acquisition of its full absorption spectrum *in situ*. In general, it is not possible to derive

an absorption spectrum directly from a reflectance spectrum because of the role of scattering must also be considered. However, with a suitable model, the measurement of diffuse reflectance and diffuse transmittance spectra of the same sample allows the derivation of absorption and scattering profiles. Specifically, we use the pile-of-plates model as described above. The results are spectra of the absorption coefficient (K) and scattering coefficient (S) (**Figure 3.7** and Appendix).

The spectra of absorption coefficients show clear absorption in the 400-650 nm region that is attributed to rhodoxanthin. The overall offset of the raw spectra (see SI) is caused by the fact that the feathers are too sparse to fully prevent direct transmission. As shown in the inset of **Figure 3.7**, the strong absorbance in the UV region can be attributed to the keratin-matrix that makes up the structural framework of the feathers. Keratin has local absorption peak at ~280 nm, but has increasingly strong absorption in the deep UV.¹⁰⁷ It is well known that carotenoids also absorb in the same region in the UV, from a $S_0 \rightarrow S_n$ absorption. However, the molar absorption coefficient of the carotenoid $S_0 \rightarrow S_n$ transition are in general approximately 5-fold smaller than that of the primary ($S_0 \rightarrow S_2$) absorption band. Therefore, the absorption at 280 nm caused by the carotenoid is expected to be much smaller than the keratin. Melanin may also contribute to the absorption of *Pt. magnificus* and *Pt. pulchellus*. Melanin has an extended absorption that is greatest in the UV, and it declines monotonically to the red.¹⁰⁸

We isolate the carotenoid absorption in the visible region by fitting a polynomial to spectral regions where that absorption is expected to be at or near

baseline. The function is subtracted to remove contributions from the protein scaffold and other absorbing species. The baseline-subtracted absorption spectra are shown in **Figure 3.7**, and clearly show a red shift from *Pt. magnificus* to *Pt. solomonensis*. Positions of the half-maxima for each feather are shown in the **Table 3.2**.

The calculated absorption profiles also yield some insights into the relative concentration of carotenoid within the feathers. With the assumption that the keratin concentrations are equal among feathers, we observe that the relative absorbance of carotenoid in *Pt. pulchellus*, *Ph. carnifex*, and *Pt. magnificus* are 2-3 times higher than *Pt. solomonensis* or *Pt. jambu*. This result is consistent with the muted appearance of *Pt. solomonensis* and *Pt. jambu*.

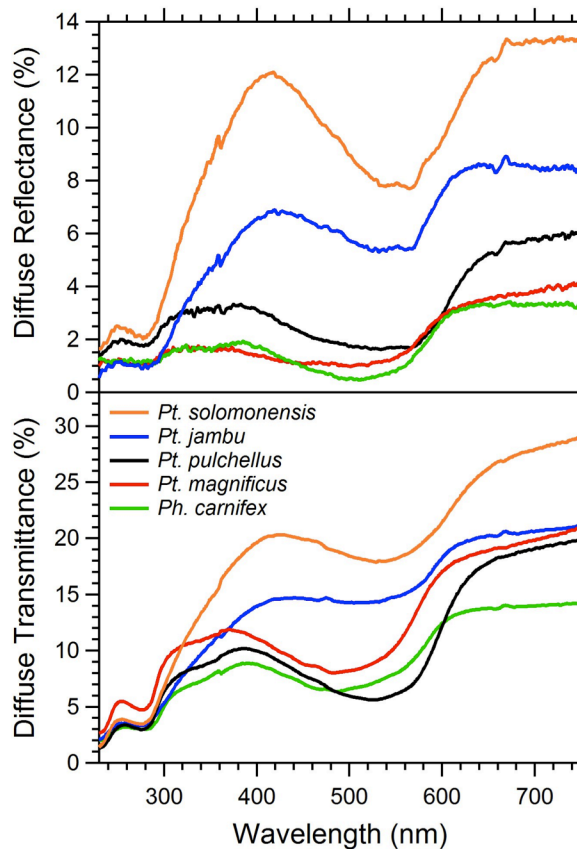


Figure 3.6: (Top) diffuse reflectance and (Bottom) diffuse transmittance of the five rhodoxanthin containing feathers.

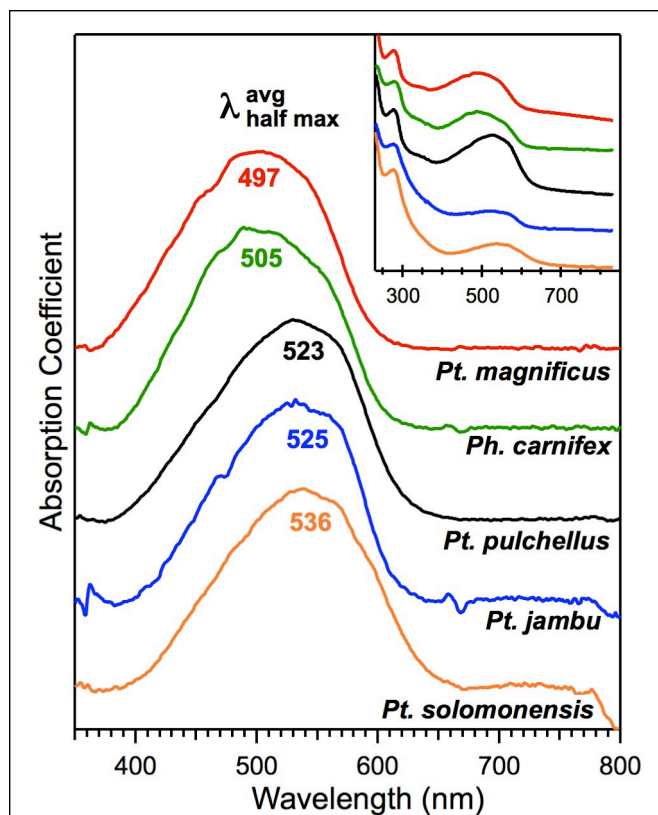


Figure 3.7: Absorption spectra of rhodoxanthin in the five feathers, calculated from diffuse transmittance and diffuse reflectance data. The spectra are offset clarity. The wavelength corresponding to the average of the two half maxima positions are shown. **(Inset)** Absorption coefficient spectra before baseline subtraction, also offset for clarity.

Table 3.2: Comparison of R_{mid} and $\lambda_{avg\ half-max}$ values for the rhodoxanthin-containing feathers

Feather	$R(\lambda_{mid})$	$\lambda_{halfmax1}$	$\lambda_{avg\ half-max}$	$\lambda_{half-max2}$
<i>Pt. magnificus</i>	584	427	497	567
<i>Ph. carnifex</i>	583	435	505	575
<i>Pt. pulchellus</i>	611	453	523	592
<i>Pt. jambu</i>	594	460	525	591
<i>Pt. solomonensis</i>	614	462	536	610

The scattering coefficient profiles of the feathers are very similar to the diffuse reflectance data, with decreased scattering in places of larger absorption and larger scattering profiles in areas of greater reflectance. Among the feathers, there is a relative increase in the scattering coefficient at ~ 400 nm with the increase in purple characteristic of the feather.

The pile of plates model assumes that 100% of the incident light interacts with the sample. However, the feathers are sparse, meaning that only a fraction of the light actually interacts with the feather. As we are measuring *diffuse* reflectance and transmittance, the non-interacting light causes the measured reflectance and transmittance to be lower than it would be if the feathers were completely full. The unaccounted for light causes the absorption (scattering) profile to be positively (negatively) offset. Aside from the offset, the profiles remain unchanged.

3.4.4 Resonance Raman spectra of rhodoxanthin-containing feathers

Overview. The room and low temperature spectra of the feathers are shown in **Figure 3.8**. These spectra were acquired with the Raman microscope with excitation at 514.5 nm. The laser spot was positioned to probe the areas of the feather that appeared to have the highest concentration of pigments. To the best of our knowledge, these resonance Raman spectra are the first reported for a retrocarotenoid. As expected, the bands are largely similar to other more common carotenoids, such as beta-carotene or zeaxanthin.¹⁷ The strongest band is ν_1 , with maximum near 1520 cm^{-1} . The band results from modes that are symmetric linear combinations of C=C stretches. The

fingerprint region (1100-1400 cm^{-1}) is dominated by ν_2 at $\sim 1155 \text{ cm}^{-1}$ which is a band that results largely from various C-C single bond stretches in combination with C-H in-plane bending motions. The bands clustered in the ν_2 region are better resolved at low-temperature, and all samples reveal that there is significant Raman scattering from at least two main bands, as well as a shoulder at $\sim 1132 \text{ cm}^{-1}$. Another strong band is ν_3 that results largely from methyl rocking motions. Finally the bands assigned to hydrogen-out-of-plane (HOOP) wagging modes are found in the region 800 - 1000 cm^{-1} . These bands gain intensity upon the loss of planarity of the carotenoid.^{109, 110} In general, band frequencies increase slightly upon lowering the sample temperature. Additionally, at low temperature the Raman amplitudes of the low-frequency bands, as well as ν_2 and ν_3 , tend to increase upon cooling relative to the ν_1 band. Similarly, enhancements of the low-frequency bands and ν_3 at low temperature are also apparent for a thin film of one isomer (**Figure 3.A5**). The peak positions of the feather spectra at low-temperature and room temperature are summarized in **Table 3.A1-3**.

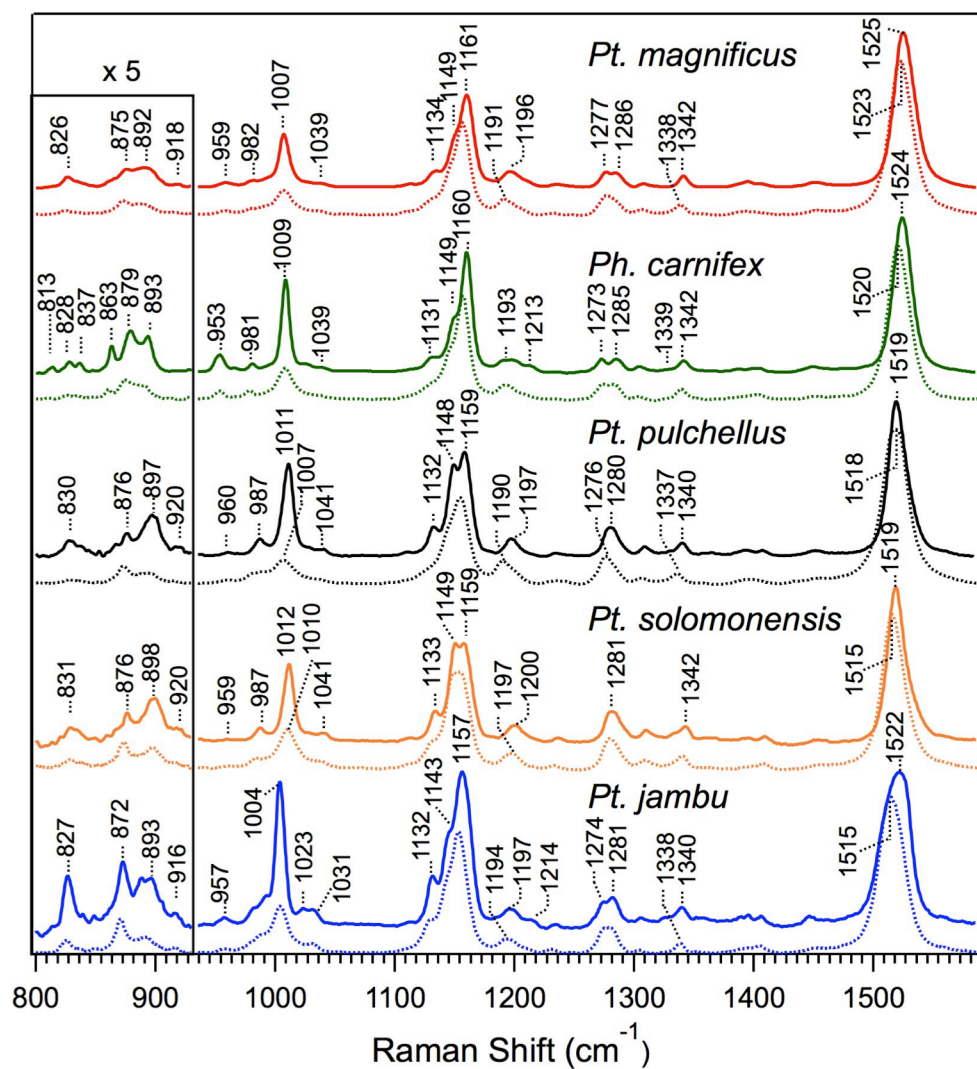


Figure 3.8: Resonance Raman spectra of avian feathers acquired with 514.5 nm excitation and a microscope setup. For each pair of spectra, the upper one is acquired at approximately -195 °C, and the lower is acquired at room temperature. The 800 – 930 cm^{-1} region is magnified by a factor of 5.

Specific description of Raman spectra of each feather sample

Pt. magnificus: This feather is characterized by the highest frequency for ν_1 at 1525 (1523) cm^{-1} at low (room) temperature. The band is somewhat broadened relative to other samples, and only *Pt. jambu* has greater breadth. The ν_2 region of *Pt. magnificus* is also broadened relative to others. The HOOP bands have the lowest intensities and are the least well resolved among all feathers. Most of the intensity in the HOOP region is found in the 875 and 890 cm^{-1} bands.

Ph. carnifex: This spectrum is most similar to *Pt. magnificus*. At low temperature, the ν_1 band has its peak at 1524 cm^{-1} , only one wavenumber lower than corresponding peak of *Pt. magnificus*. The maxima of the bands in the fingerprint region for both samples have frequencies that match one another within several wavenumbers. However, the spectra of *Ph. carnifex* appear to be the most well-resolved, with narrower ν_2 and ν_3 bands relative to spectra of *Pt. magnificus* and other species. Other bands in the fingerprint region, e.g. at 1275 and 1285 cm^{-1} are distinguishable even at room temperature. Likewise, the bands in the HOOP region are the most well resolved and numerous of all the feathers at low temperature and span the range of frequencies from 813 to 981 cm^{-1} . Unique to the Raman spectra of *Ph. carnifex* is a sharp mode at 863 cm^{-1} , and the intensity of the 953 cm^{-1} band is considerably greater than corresponding modes in the 950-960 cm^{-1} region of any other sample. Whether all of the bands can be assigned to rhodoxanthin is not certain.

Pt. pulchellus and *Pt. solomonensis*: The low-temperature resonance Raman spectra of these feathers appear to have no significant differences. The ν_1 frequency maxima are at identical position (1519 cm^{-1}) at low temperature. The fingerprint region reveals a band-for-band match for the two species, with at most a $\sim 3\text{ cm}^{-1}$ difference in the position of corresponding maxima. Both show clear doublet character to ν_2 , with significant intensity of one band centered at $1148\text{-}1149\text{ cm}^{-1}$, and another centered at 1159 cm^{-1} . A clear shoulder has a maximum at $1132\text{-}1133\text{ cm}^{-1}$. Finally, the methyl rock and six HOOP modes match with at most 1 cm^{-1} difference in the positions of the maxima. The intensities of the HOOP modes are very similar in the spectra of the two feathers.

Pt. jambu: The $\sim 7\text{ cm}^{-1}$ upshift in ν_1 upon cooling (from 1515 cm^{-1} to 1522 cm^{-1}) is a considerably greater change than seen for any other feather. The reason for the shift, as well as the overall greater breadth of this band is clear from the low-temperature spectrum, where it is obvious that the intensity in the ν_1 region is due to two overlapping bands. A fit of the spectra to two Voigt profiles yields peak positions at 1510 cm^{-1} (small) and 1524 cm^{-1} (large). Another unusual aspect of the *Pt. jambu* resonance Raman spectrum is the anomalously large HOOP band at 827 cm^{-1} . The relative intensity in the HOOP mode region is greatest for *Pt. jambu* among all the samples.

Effect of irradiance on the resonance Raman spectra

A comparison of the low and high irradiance Raman spectra of the feathers are shown in **Figure 3.A2**. The high-irradiance experiments employed a tightly focused $\sim 1 \mu\text{m}$ diameter beam that could probe a specific area of a single barbule, whereas similar specificity was not possible for the 2.50 mm by 0.040 mm sized spot of the low-irradiance experiments. Nevertheless, the spectra acquired at low and high irradiance, and over the differing areas, are nearly identical. In some cases there are differences in peak positions of $\sim 2 \text{ cm}^{-1}$. It is not clear whether these shifts are caused by the differing irradiance or uncertainties in the wavelength calibration. As the shifts observed between the high- and low- irradiance spectra of feathers are similar to shifts seen in spectra of thin films, it seems highly likely that the same explanation would hold for both feathers and films.

3.4.5 Resonance Raman spectroscopy of rhodoxanthin in solution.

The spectra of the three rhodoxanthin isomers with 568.2 nm excitation are shown in **Figure 3.9**. The position of the ν_1 band maximum downshifts slightly in the *trans* (E) configuration, relative to *cis* (Z): 6Z6'Z (1526 cm^{-1}), 6E6'Z (1524 cm^{-1}), and 6E6'E (1520 cm^{-1}). The ν_2 band has a maximum at $1158\text{--}1160 \text{ cm}^{-1}$ and the frequency position does not vary significantly or systematically among the isomers. In terms of intensities, the ν_2 band increases and ν_3 band decreases relative to the ν_1 band, in the series 6E6'E, 6E6'Z, and 6Z6'Z. The 1195 cm^{-1} band becomes less intense from 6E6'E \rightarrow 6Z6'Z while the 1205 cm^{-1} band increases. Also, the 1343 cm^{-1} band

intensity decreases from 6E6'E → 6Z6'Z while the 1312 cm^{-1} and 1392 cm^{-1} bands increase in intensity. Additionally, a small band at $\sim 825\text{cm}^{-1}$ is gains intensity between 6E6'E and 6Z6'Z.

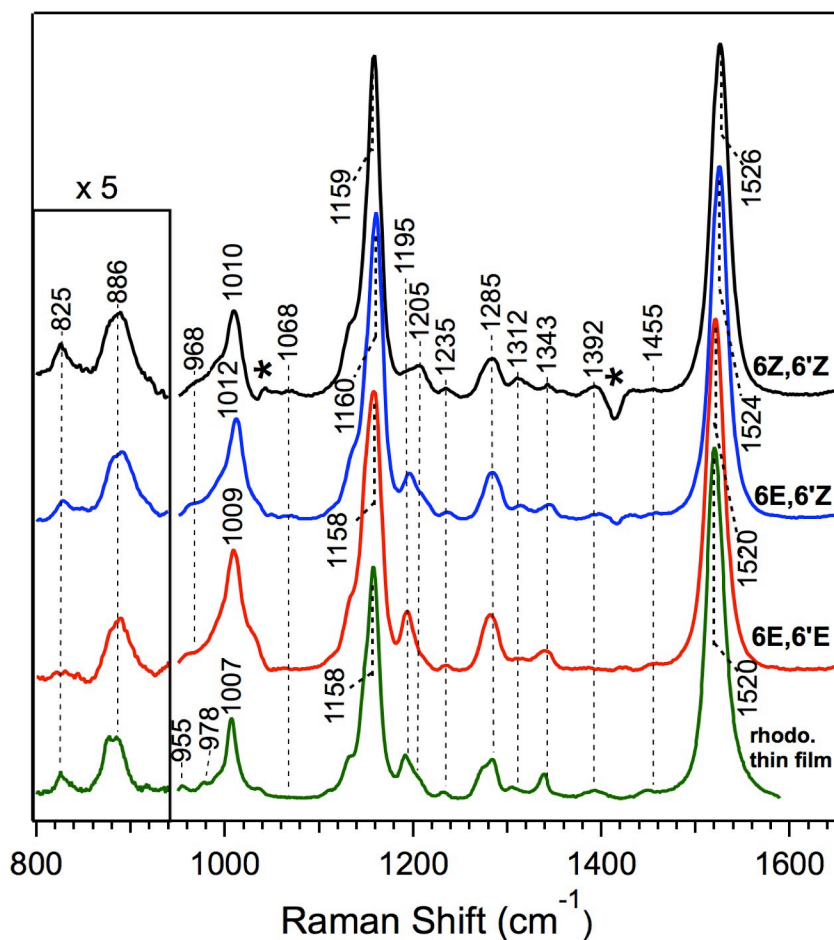


Figure 3.9: Raman spectra of rhodoxanthin isomers in solution and in the solid state. Raman spectra of rhodoxanthin in DMSO, with excitation wavelength 568.2 nm. The asterisks (*) denote regions where the solvent subtraction was imperfect. The green trace is the spectra of the thin film of rhodoxanthin on a glass substrate, acquired at high irradiance with a microscope. The excitation wavelength was 514.5 nm. The 800-950 cm^{-1} region all traces are magnified 5x. Each rhodoxanthin spectrum was normalized for equal amplitude of the ν_1 band.

Absorption spectra were taken before and after laser exposure to probe the stability of rhodoxanthin in solution. No shifts in the absorption maxima for any of the

3 isomers were observed after exposure to the laser, indicating that the majority of the rhodoxanthin remained in the starting configuration (**Figure 3.A3**). The stability of rhodoxanthin is also explored in section 3.4.7.

3.4.6 Resonance Raman spectroscopy of rhodoxanthin thin-films

The resonance Raman microscope spectra of the three rhodoxanthin isomer thin films exhibit very similar bands, both in peak position and relative amplitudes. Resonance Raman microscope spectra of a 6E6'E thin film at 514.5 nm excitation is also shown in **Figure 3.9**. The peak positions of ν_1 (1520-1521 cm^{-1}), ν_2 (1158 cm^{-1}), and ν_3 (1007 cm^{-1}) do not vary among the isomers. In addition, the HOOP region (800-980 cm^{-1}) shows no differentiation among isomers. Interestingly, the HOOP doublets at 955 and 978 cm^{-1} are more resolved than in the solution-phase spectra. No changes in the spectra were observed during the 15 min accumulation as observed in a series of 30-second exposures.

The resonance Raman spectra of the 6E6'E and 6E6'Z rhodoxanthin thin films have very similar peak positions, whether acquired with high- (514.5 nm excitation) or low- (568.2 nm excitation) irradiance excitation (**Figure 3.A4**). Only the ethylenic mode seemed to have a consistent $\sim 2 \text{ cm}^{-1}$ downshift with low irradiance and excitation wavelength. Specifically, when normalized to the amplitude of the ν_1 ethylenic band, ν_3 and lower frequency modes (e.g. HOOP modes) have relatively greater amplitudes at low irradiance and 568.2 nm excitation than high irradiance and

514.5 nm excitation. As with the high-irradiance experiments, no spectral shifts were noticed during the course of the low-irradiance excitation of thin films.

3.4.7 Photolysis of the 6-trans, 6'-cis isomer of rhodoxanthin

The photo-lability of rhodoxanthin in solution can be determined through bulk photolysis. Similarly to the rhodoxanthin solution absorption spectra taken after the Raman experiment at 568.2 nm excitation, the un-illuminated control sample showed no spectral shift after 60 min, indicating that little to no isomerization had occurred (**Figure 3.10**). However, closer inspection by HPLC revealed that this sample had undergone a small amount of isomerization, as indicated by a small 6Z6'Z peak seen at 9 min, and a 6E6'E peak observed at 12 min (**Figure 3.10B**). This result confirms that a small amount of isomerization occurs even when the sample is kept in dim light at room temperature, and suggests that the thermal barrier to isomerization in rhodoxanthin is quite low. In the HPLC chromatogram, integration of absorbance over the time axis indicate that the ratio of isomers are 6E6'E (5.6%): 6E6'Z (89.8%): 6Z6'Z (4.6%), assuming the extinction coefficient at 480 nm is equal among isomers.

The laser-illuminated sample spectrum showed a 3 nm spectral red-shift within the first 5 min of photolysis and remained essentially unchanged during the remainder of the 60 min illumination period (**Figure 3.10A**). This shift suggests a conversion to the all-trans isomer. HPLC analysis (**Figure 3.10C**) revealed that a substantial amount of both the 6Z6'Z and 6E6'E isomer were formed, as indicated by the appearance of

peaks at 9.6 and 12.6 min retention times. Integration of the HPLC chromatogram indicate that the ratios are 6E6'E (34.8%): 6E6'Z (49.1%): 6Z6'Z (16.1%).

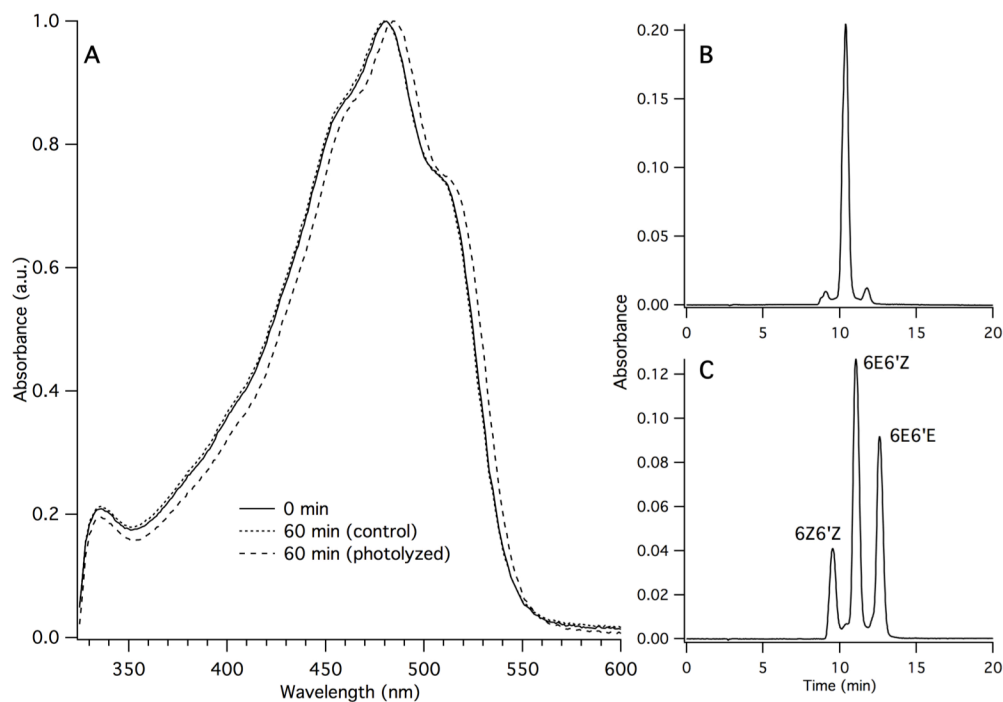


Figure 3.10. (A) Absorption spectra of 6E6'Z at 0 mins (black line) and after 60 mins of either no illumination (short dashes) and laser-illumination (long dashes). Right panels: NP-HPLC chromatogram of rhodoxanthin: (B) control sample after 60 min in dim light; and (C) sample after 60 min of laser illumination. The HPLC detection wavelength was 480 nm.

3.4.8 Calculations of the electronic structure and vibrational frequencies of rhodoxanthin isomers

Table 3.3 contains several important energetic and geometric results obtained from the retro-carotenoid and beta-carotene calculations at the B3LYP/6-31G(d) level of theory. The ionone rings of the retro-carotenoids, rhodoxanthin and iso-carotene, are much flatter with respect to the polyene chain than beta-carotene, as indicated by a

comparison of the dihedral angles. For rhodoxanthin, the C(6)=C(7) bond is slightly shorter when in the Z configuration than the E configuration, due to the enhanced conjugation of the polyene chain with the ionone ring.

Table 3.3: Results from DFT calculations

Molecule	E (cm ⁻¹)	Dihedral angle ^a (degrees)		Bond length (Å)		ν ₁ (cm ⁻¹)
		D	D'	C6-C7	C6'-C7'	
(6E,6'E)-rhodoxanthin	+341	-179.9	-179.9	1.374	1.374	1511
(6E,6'Z)-rhodoxanthin	+177	176.8	160.1	1.374	1.370	1513
(6Z,6'Z)-rhodoxanthin	0	-160.1	160.1	1.370	1.370	1516
β-carotene	-----	-48.9	48.9	1.475	1.475	1520
Isocarotene	-----	-168.0	168.0	1.372	1.372	1518

^a The dihedral angles are C5=C6-C7=C8 for β-carotene, and C4=C5-C6=C7 for the retro-carotenoids.

Table 3.4: Calculated frequencies of select normal modes of rhodoxanthin.

Frequency of mode (cm ⁻¹)			Assignment
6E,6'E	6E,6'Z	6Z,6'Z	
1511	1513	1516	Symmetric C=C stretches, extending from C8-C9 to C8'-C9'
1390,1401	1387,1395	1386,1395	Methyl bends + CH rock
1335	1334	1334	C13-C14 stretch ^a + CH rocks
1323	1324	---	CH rocks (including ring C4H) for E configuration
---	1300	1300	CH rocks (including ring C4H) for Z configuration
1209	1209	1209	C15-C15' stretch + CH rocks
---	1194	1194 (w)	C7-C8 stretch + ring methylene rock + CH rocks ^a
1181	1182, 1181, 1177	1178	C7-C8, C11-C12 stretches + CH rocks ^a
1158	1152, 1157, 1160	1155	C11-C12, C15-C15' stretches + CH rocks ^a
1143	1141	1138 (w)	C15-C15' stretch + CH rocks
995	996, 997	998	Methyl rocks
966	967 (w)	968 (w)	C10H, C11H, C12H HOOP wags ^a
899	902, 897	902	C7H, C8H and other HOOP wags ^a ; ring torsion
884	885, 883	885	C7H, C8H HOOP wags ^a
876	877	---	C7H and ring CH HOOP wags ^a
838	832	833 (w)	C8H, C10H, C11H, C14H, and C15H HOOP wags ^a

Abbrev: HOOP – Hydrogen-out-of-plane; (w) – weak

^a These modes include motion of the unlisted primed carbons on the opposite side of the molecule, e.g. a mode with the C13-C14 stretch also includes C13'-C14'.

The calculated Raman spectra for each of the three isomers are shown in **Figure 3.11**. Calculated Raman spectra for β -carotene and another retro-carotenoid, iso-carotene, are shown in the supplementary information (**Figure 3.A7**). **Table 3.3** contains the frequencies and assignments of bands in the calculated Raman spectra of rhodoxanthin.

The DFT calculations suggest that the ν_1 mode of retro-carotenoids such as rhodoxanthin contains C=C in-phase stretch vibrations from all double bonds between C(8)=C(9) and C(8')=C(9'). In comparison, the in-phase stretching vibrations of ν_1 mode of normal *all-trans* carotenoids, such as β -carotene, are localized between C(11)=C(12) and C(11')=C(12'). As discussed above, the experimental solution-phase results indicate a progressive downshift in the ethylenic (C=C) stretch mode in the isomer series of 6Z6'Z to 6E6'E. The DFT calculations agree with these results and the 6Z6'Z, 6E6'Z, and 6E6'E isomers have ν_1 frequencies of 1516, 1513, and 1511 cm^{-1} , respectively. The downshift correlates with enhanced planarity of the polyene backbone of rhodoxanthin, which extends into the ionone ring. With the E configuration, the dimethyl group attached to the ionone ring can straddle the polyene hydrogen attached to the C(8)/C(8') position, and thus keep the ionone ring relatively coplanar with the polyene backbone. Conversely, for the Z configuration there is steric hindrance between the single methyl group attached to the ionone ring, and the hydrogen at the C(8)/C(8') position. One would therefore expect a greater dihedral angle between the double bond on the ionone ring and polyene backbone in the Z configuration versus the E configuration. The DFT calculations indicate that the

6Z6'Z isomer dihedral angles are both -160.0° , the 6E6'Z isomer dihedral angles are -160.3° (Z) and 176.8° (E), and the 6E6'E isomer dihedral angles are both 179.9° .

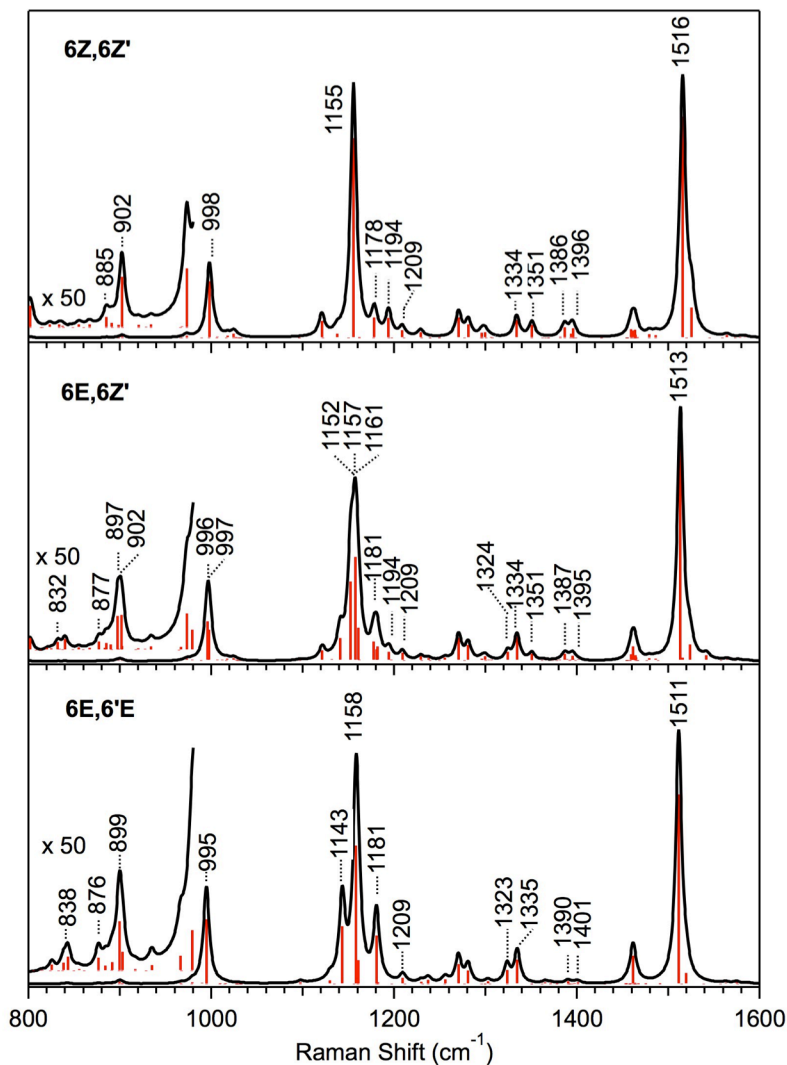


Figure 3.11: Results of the Gaussian 09W calculations of three rhodoxanthin isomers. The 800-980 cm^{-1} region has been magnified by 50x to clearly show the modes.

The fingerprint region ($1100 - 1400 \text{ cm}^{-1}$) is sensitive to the structure and geometry of the polyene chain, and is therefore useful in distinguishing isomers and different configurations of carotenoids. The ν_2 mode has a frequency of $\sim 1158 \text{ cm}^{-1}$

and is a combination of C-C single bond stretch vibrations and C-H in-plane (HIP) wags. We will focus on several prominent bands calculated for the rhodoxanthin at $\sim 1143\text{ cm}^{-1}$, $\sim 1158\text{ cm}^{-1}$, and $\sim 1181\text{ cm}^{-1}$. The strongest band, 1158 cm^{-1} , is similar among rhodoxanthin isomers. From 6E6`E to 6Z6`Z there is a loss of the 1181 cm^{-1} band and a growth of the 1194 cm^{-1} band. These calculated modes correspond to the 1194 cm^{-1} and 1205 cm^{-1} bands observed in the solution-phase results. Although the calculated 1143 cm^{-1} mode decreases in intensity between E configuration and the Z configuration, there is no corresponding decrease in intensity in the solution-phase Raman spectra.

The 6E6`Z ν_2 mode is split into bands at 1152 cm^{-1} , 1157 cm^{-1} , and 1160 cm^{-1} , due to the asymmetry of the molecule. The ν_2 band of the low-temperature feather Raman spectra shares the greatest similarity with that of the 6E6`Z isomer computational results, with at least two bands between 1150 cm^{-1} and 1160 cm^{-1} . The ν_2 band rhodoxanthin solution phase and thin film spectra share the same multi-band characteristic, although the peaks are not defined as well.

There are other trends in the fingerprint region of the calculated Raman spectra that correlate to observable differences between the rhodoxanthin isomers. For the solution-phase Raman results, the bands at 1312 cm^{-1} and 1392 cm^{-1} are larger with the Z configuration, and the 1343 cm^{-1} is larger with the E configuration. These modes correspond to the growth of the calculated modes at 1302 cm^{-1} , 1386 cm^{-1} , and 1394 cm^{-1} with the series 6E6`E to 6Z6`Z and the growth of the 1334 cm^{-1} mode with the

series 6Z6`Z to 6E6`E. All of these modes correspond to different combinations of methyl bending and HIP wagging vibrations.

The methyl rock mode (ν_3) of rhodoxanthin was calculated to have a frequency between 995(6E6`E) -998(6Z6`Z) cm^{-1} . In the E configuration, the DFT results suggest that the ionone ring methyl group next to the double bond is aligned with the methyl groups on the polyene chain and the methyl groups rock in-phase. In contrast, the Z configuration indicates weak contribution from all three of the methyl groups on the ring. The calculated Raman spectrum of the 6E6`Z isomer indicate two methyl-rock modes, one isolated to each side of the molecule corresponding to the E and Z trans. The slight changes in the ν_3 mode were too small to observe with the experimental procedures employed in this study.

Also important is the differences observed for the hydrogen-out-of-plane (HOOP) modes, which are located between 800-1000 cm^{-1} . The HOOP modes are sensitive to the distortion of the chain^{109, 110} and it has been proposed that a doublet in the IR absorption near 965 cm^{-1} is characteristic of retro-carotenoids.¹¹¹ With this in mind, we hoped to gain insight in the Raman signatures in the HOOP region for the rhodoxanthin isomers.

In each of the DFT calculations for the three rhodoxanthin isomers, there are several HOOP modes that are different from the HOOP modes of non-retro carotenoids and another mode that may be a indicator of E or Z configuration at the C(6)=C(7) position. Calculated rhodoxanthin modes at $\sim 966 \text{ cm}^{-1}$ and $\sim 989 \text{ cm}^{-1}$

correspond to HOOP modes of the hydrogen atoms at the C(10)/C(10'), C(11)/C(11'), and C(12)/C(12') positions and C(14)/C(14') and C(15)/C(15') positions, respectively. The positions of these modes do not change significantly between the three isomers.

Several HOOP modes of rhodoxanthin include contributions from the ionone ring, particularly modes at 900 cm^{-1} , 884 cm^{-1} , and 876 cm^{-1} . The 876 cm^{-1} mode is unique to the E configuration, and is a combination of C(7)/C(7') HOOP wag with methylene rock on the ionone ring. Other HOOP modes between $820\text{--}840\text{ cm}^{-1}$ have the highest intensity in the 6E6'E isomer and contain a combination of ring displacements and ring HOOP wags. These modes are likely not as resonantly enhanced in non-retro-carotenoids, as the ionone ring is out of the plane of the polyene chain in other carotenoids and therefore the H atoms are not on conjugated carbons.^{17,}

112, 113

As noted before, there is an emergence of a $\sim 825\text{ cm}^{-1}$ band in the rhodoxanthin solution-phase results from 6E6'E to 6Z6'Z (**Figure 3.9**), indicative that a mode in the region may be characteristic of the Z configuration. Candidate modes may be a HOOP wag and ring torsion mode, calculated for 6Z6'Z at 823 cm^{-1} , or an out-of-phase polyene chain HOOP mode, calculated at 834 cm^{-1} .

3.4.9 Experimental and Calculated evidence for C=O stretch in rhodoxanthin

The C=O stretch mode, which commonly has a frequency between $1685\text{--}1666\text{ cm}^{-1}$ for a conjugated system¹¹⁴, was calculated to be at $\sim 1694\text{ cm}^{-1}$ for rhodoxanthin. The frequency of the C=O stretch is invariant with different isomeric configurations,

indicating that the planarity of the ionone ring double bonds with the polyene backbone does not affect the C=O stretching frequency.

Experimentally, we observe a potential C=O stretch band at 1648 cm^{-1} for the rhodoxanthin-containing feathers and thin films and 1658 cm^{-1} for rhodoxanthin in DMSO (**Figure 3.A6**). This value is very similar to a previously reported value of 1659 cm^{-1} .¹¹⁵ The frequency does not change significantly or systematically among the five feathers.

3.5 Discussion

3.5.1 Overview

Through HPLC analysis of extracted pigments of several species of fruit doves (family: Columbidae; genus: *Ptilinopus*) and a cotinga (family: Cotingidae), we have verified, in support of earlier findings, that rhodoxanthin is the primary carotenoid within these birds and is responsible for the wide range of coloration seen in their plumage.^{80, 85} Rhodoxanthin is a relatively rare pigment in vertebrates, only existing in certain species of fish and birds.^{116, 117} Much more abundant in plants, it was believed until relatively recently that rhodoxanthin found in feathers were originated from insects or plants in the diet, and deposited unaltered into the feathers.¹¹⁸ However, there has been recent evidence to support the endogenous metabolism of rhodoxanthin from dietary xanthophylls in manakins and one species of cotinga.^{79, 80} Fruit doves are mainly frugivorous, and although berries and fruit are known to

contain rhodoxanthin, it is not known whether fruit pigeons have the ability to metabolize rhodoxanthin from other dietary carotenoids.

With the goal of determining the mechanisms by which rhodoxanthin exhibits different colors within the keratin matrix of the feather, we have analyzed *in situ* the feathers of 5 different bird species through reflectance spectroscopy and resonance Raman spectroscopy and compared the results with the spectra from isolated rhodoxanthin pigment, both in solution and in thin-films.

The origins of the vibrational and electronic changes of carotenoids in different environments has been addressed extensively in the past for the carotenoproteins of lobsters and other invertebrates^{10,92} and carotenoid containing feathers of birds.^{7,8,93} We will discuss the results observed with respect to four mechanisms that alter the way that light is absorbed by the carotenoid: 1) medium effects, such as changes in the refractive index between solvent and protein scaffold, 2) polarization, through interactions with charged amino acid residues, 3) distortion of the polyene backbone, and 4) electronic interactions. We will also discuss the observed change in color in terms of isomeric differences among feathers, pigment concentration, and structural coloration.

We will also discuss the differences in resonance Raman experimental techniques, their respective strengths and weaknesses, and their observed effects on resonance Raman spectroscopy, with special focus on the possibility of laser induced isomerization of rhodoxanthin.

3.5.2 Color and Raman spectroscopy

Previously, reflectance spectroscopy was the favored spectroscopic technique to gauge color and carotenoid-attributed absorption shifts within avian plumage.^{80,94} However, here we report, to the best of our knowledge, the first use of the “pile of plates” model as an extension of the Kubelka-Munk theory within an avian plumage system. While reflectance spectroscopy is the favored choice for its portability to the field and largely non-invasive implementation,⁹⁶ the ‘pile of plates’ model is useful to separate the absorption coefficient profile from the scattering profile, and gain an understanding of the shifts in the carotenoid electronic absorption.

As was previously mentioned, the perceived colors of the feathers (**Figure 3.5**) agree well with the calculated absorption and scattering coefficient profiles (**Figure 3.7**); a red shift in the feather absorption coefficient profiles corresponding to an increase in the purple characteristic of the five feathers. Although both the absorption and scattering coefficient profiles contribute the perceived color of the feathers, the absorption coefficient profile contains information relating to the electronic and vibrational structure of the carotenoid pigment. The series of low to high λ_{\max} for the feathers, *Pt. magnificus* (497 nm) < *Ph. carnifex* (505 nm) < *Pt. pulchellus* (523 nm) < *Pt. jambu* (525 nm) < *Pt. solomonensis* (536 nm), agree well with the series of high to low ν_1 frequency (high-irradiance, room temp) *Pt. magnificus* (1523 cm^{-1}) > *Ph. carnifex* (1520 cm^{-1}) > *Pt. pulchellus* (1518 cm^{-1}) > *Pt. jambu* = *Pt. solomonensis* (1515 cm^{-1}). Interestingly, the series of low to high $\lambda(R_{\text{mid}})$ for the feathers agrees closer to the low-temperature ν_1 frequencies. However, as the relationship between

color and ν_1 frequency is more relevant at room temperature, we will not discuss the reasons for this further.

Thus the frequencies of the ethylenic mode (ν_1) of the feathers are connected to the electronic absorption in the usual way, namely where the frequency of ν_1 correlates with energy of the electronic transition.³ However, there are some exceptions that warrant discussion. Despite similar color, we observe that the ν_1 peak positions of *Pt. magnificus* and *Ph. carnifex* differ by $\sim 3 \text{ cm}^{-1}$. Similarly, the ν_1 peak positions of *Pt. solomonensis* and *Pt. jambu* are identical, although their colors appear to be significantly different. Both of these observations indicate a breakdown of the well-established relationship between the frequency of ν_1 and $1/\lambda_{\text{max}}$ of the absorption band.

3

Medium effects, which are the differences in the refractive indices among solvent environment, have also been shown to be very important in the position of E_{00} .^{8, 119} For carotenoids, an increased index of refraction, n , is correlated with a decrease in E_{00} , through a linear relationship with the polarizability of the solvent, $R(n) = (n^2 - 1)/(n^2 + 2)$. For our own results, we observe a similar trend. 6E6'Z in methanol, which has a n of 1.33¹²⁰ has a λ_{max} of 484 nm. 6E6'Z in DMSO, with a n of 1.48,¹²¹ has a λ_{max} of 504 nm. On the other hand, the refractive index of avian keratin is 1.58¹²², which indicates that a greater red-shift for the λ_{max} of rhodoxanthin in feathers is expected. This result is observed, as the average λ_{max} of rhodoxanthin in feathers is ~ 520 nm. However, assuming that the keratin matrix between the birds is

identical, the variance of λ_{\max} among feathers indicates that other effects are responsible for the variance in color.

Therefore, variation in carotenoid-protein interactions may account for the range of colors observed in the feathers. There are several means by which rhodoxanthin may be perturbed within the matrix of keratin or other protein. A polarization mechanism, caused by hydrogen bonds between keto-carotenoids and positively charged or polarizable amino acid residues, result in a decrease in the ν_1 frequency and a redshift in the absorption spectrum.^{7, 88, 92} This mechanism has been identified as one of the primary causes of spectral shifts in canthaxanthin-containing feathers.⁸ We may also see evidence of polarization in the change in C=O stretch frequencies between the solution phase resonance Raman spectra and the feather Raman spectra (**Figure 3.A6**). There is a $\sim 10 \text{ cm}^{-1}$ decrease in the C=O stretch frequency compared to the solution-phase results which could indicate hydrogen bonding of a hydroxylic amino acid residue to the carbonyl.¹²³ Alternatively, increased effective conjugation length could also decrease the C=O stretch frequency.¹¹⁴

Within the carotenoid-protein environment, interactions with amino acid residues can distort or alter the configuration of the polyene backbone, which has been observed to disturb the relationship between ν_1 and λ_{\max} . However, among solvated carotenoids, there is an additional correlation between the frequencies of the ν_1 and ν_2 modes. Both modes, which correspond to the C=C and C-C stretches, are affected by the ‘effective conjugation length’, which is also skewed by distortions about the polyene backbone.^{3, 92, 93} With the exception of *Pt. jambu* at low temperature, there is

a good correlation between the ν_1 and ν_2 frequencies, in both the feather and isolated rhodoxanthin spectra, indicating that the rhodoxanthin in the feathers is not significantly more distorted than the rhodoxanthin in solution or thin film and that the amount of distortion is similar among the feathers.

In a similar canthaxanthin-feather system, there is a trend between the relative magnitude of the ν_4 mode with the decrease of the ν_1 frequency and redshift of the absorption band.⁸ We observe a similar trend among the rhodoxanthin-containing feathers. Besides having the most red-shifted absorption spectra, *Pt. solomonensis* and *Pt. jambu* at room temperature have larger bands in the 860-900 cm^{-1} (HOOP) region, than the other feathers. It is not clear how the enhancement of these modes correlate to red-shifted absorption spectra.

It is well known that carotenoids form aggregates in certain aqueous environments^{17, 39, 124}, and within lipid bilayers in biological and biomimetic systems¹²⁵ Electronic coupling between carotenoid molecules resulting from aggregation causes a perturbation of the excited state, which is split into in-phase and out-of phase exciton states. Within a protein framework such as a feather, it is possible that carotenoids become close to one another and exhibit exciton-coupling, causing a shift in the absorption spectra. The orientation of chromophores in the aggregate determines whether the in-phase (most-allowed) state is higher or lower in relative to the unperturbed excited state.²⁸

Exciton-coupling between astaxanthin molecules in crustacyanin has been hypothesized to cause shifts in the absorption profile.¹²⁶⁻¹²⁸ Although exciton-coupling splits the excited state of the carotenoid, the ground state is unperturbed, thus leaving the vibrational frequencies the same. However, although exciton-coupling does not change the ground state, physical effects induced by aggregation may. We have previously reported that zeaxanthin aggregates flatten with aggregation, increasing delocalization and causing a downshift in the ν_1 frequency.¹⁷ Therefore, packing effects from aggregation may play a large role in the variance of the ν_1 frequency and observed color.

In the case of the feathers, changes in the absorption profile, without corresponding changes in the ν_1 frequency, may be indicators of exciton-coupling among feathers. Exciton-coupling may be the most feasible cause of the difference in color seen between *Pt. solomonensis* and *Pt. jambu*, where, despite having the same ν_1 frequency, *Pt. solomonensis* absorption is significantly broader and redder than *Pt. jambu*. The relative red-shift of the absorption spectra is indicative of head-to-tail orientation of the chromophores.²⁸

3.5.3 Carotenoid concentration and photonic structure

Additional sources of color change can be carotenoid concentration and photonic structure. We have observed in carotenoids that the perceived color changes with concentration. Low concentrations of zeaxanthin appear yellow and highly concentrated solution is a deep red while low concentrations of rhodoxanthin appears

pink and highly concentrated solutions is also a deep red (*data not published*). *Pt. solomonensis* and *Pt. jambu* feathers are thought to have a lower concentration of carotenoids than the feathers of the other fruit pigeons, as indicated by lower carotenoid absorption relative to the keratin-absorption in the UV-region (**Figure 3.7**) and less vibrant appearance of the feathers. Between the feathers studied in this report, the *Pt. magnificus* feather contains the largest amount of photonic structures (**Figure 3.5**). The iridescent structures are likely related to the physical coloration seen in many other bird species, including parrots, peacocks, as well as other pigeons^{81, 129-131}. In domestic pigeons (*Columba livia domestica*), iridescent feathers of two different colors, green and purple, are observed. The iridescence originates from a thin film of keratin cortex, and the specific color as observed with a normal viewing angle is determined by the thickness of the keratin cortex, where the thicker keratin yields a green color.¹²⁹ Similarly, we observe two different colors of iridescent structure, blue (distal end of the feather) and green (proximal end of the feather), indicating that the thickness of keratin cortex decreases along the length of the feather.

The structural coloration, as perceived by eye, is not accurately reproduced in the reflectance spectra when collected with the integrating sphere. The reflectance spectrum changes with respect to the viewing angle, and since the integrating sphere collects all diffusely reflected light, the measured reflectance spectra would be an average of the reflectance over all angles. Although we currently cannot correct for this effect, there has been recent work to develop an apparatus to solve this problem.

3.5.4 Effect of isomerization at the 6,6' position on the vibrational and electronic structure of rhodoxanthin and rhodoxanthin-containing feathers

The DFT calculations (**Figure 3.11**) support the experimental trend of an increase in the ν_1 frequency in rhodoxanthin with *cis*-configuration at the C(6)/C(6') position. As was shown in an analogous system of canthaxanthin containing feathers, twisting of the ionone ring out of plane of the polyene backbone decreases the delocalization of the π -electrons into the terminal rings.^{80, 133} Similarly for rhodoxanthin, the *cis*-configuration of the double bond at the C(6)/C(6') position increases steric interaction between the methyl group on the ionone ring and the hydrogen at the C(8)/C(8') position. The steric hindrance is alleviated by an increase of the dihedral angle between the double bond on the ionone ring and the polyene backbone, thus decreasing the delocalization of the π -electrons into the terminal rings. Also corroborative of the increase in the length of delocalization along the carotenoid is the absorption spectra of the three rhodoxanthin isomers (**Figure 3.A3**) show a redshift of the all-trans isomer compared to the 6Z,6'Z isomer.

Two pieces of evidence indicates that rhodoxanthin isomers alone cannot account for the change of color among the feathers. First of all, the variation of ν_1 frequency among the five feathers ($\sim 9 \text{ cm}^{-1}$) exceeds that of the solution-phase rhodoxanthin isomers (6 cm^{-1}). Second, the shift in absorption spectra in of the rhodoxanthin isomers in methanol is only 520 cm^{-1} , while the estimated variance of λ_{max} is $\sim 1070 \text{ cm}^{-1}$. Although isomer effects may play a part in the variance in color

among feathers, it is not currently possible to determine the proportions of each isomer – the extraction process is known to cause isomerization.⁷

3.5.5 high- vs low- irradiance vs low temperature resonance Raman spectroscopy of rhodoxanthin-containing feathers

We will now discuss the effects of changing the experimental parameters between high- and low- irradiance and low-temperature on the resonance Raman spectra of the feathers. As will be discussed below, low-irradiance Raman spectroscopy was conducted to reduce the possibility of photo-degradation upon laser exposure. Compared to the high-irradiance resonance Raman spectra, the frequency of the ν_1 mode decreases by $\sim 2\text{ cm}^{-1}$ at low-irradiance. One explanation for this trend is local heating, which could cause the molecule to become more like rhodoxanthin molecules in solution.¹³⁴ Additionally, an increase in the frequency of the ν_1 mode is observed in the low-temperature spectra relative to the room-temperature spectra, possibly indicating a dependence of vibrational frequency on temperature seen in other systems such as silicon or graphene.^{135, 136} Alternatively, simultaneous changes in the ν_1 frequency with temperature may indicate that the decrease in thermal energy allows for a more twisted geometry of the carotenoid. Enhancements of the low-frequency modes, especially the in the $820\text{-}970\text{ cm}^{-1}$ region, may indicate increased distortions of the polyene backbone.

3.5.6 Comparison with carotenoprotein systems

A comparison of carotenoid-containing feathers with other carotenoid-protein systems, especially of crustaceans, is important to understand the mechanisms by which the coloration variation is observed. In carotenoproteins, such as α -crustacyanin, there is a specific binding site for the carotenoid ligand. In this protein, astaxanthin aids in the dimerization of α -crustacyanin to form β -crustacyanin.⁹² As the astaxanthin ligand binds to the protein pocket, the electronic and vibrational properties of the carotenoid are significantly perturbed. Astaxanthin in dichloromethane has a λ_{max} of 486, while a β -crustacyanin has a λ_{max} of 629 nm⁹. This large red shift in the absorption spectrum has been attributed to a combination of distortion and polarization effects,^{10, 90} as well as exciton-coupling.^{126, 128}

Therefore, the shifts in carotenoid absorption observed between solvated carotenoid and within the keratin matrix have the potential to be much greater than the corresponding shifts of rhodoxanthin within keratin matrix. Although the mechanism of binding for carotenoids in feathers is not explicitly known, it is the commonly held belief that carotenoids are directly bound to the surface of the keratin matrix, with unknown order, structure, or particular specificity.^{7, 83} In contrast, carotenoproteins usually have specific binding site for a certain carotenoid. Within the binding cavity, there are often either hydrophobic or aromatic amino acid residues that can interact with the carotenoids, perturbing the electronic and vibrational structure through distortion or polarization.¹³⁷ The relative narrowness of the feather Raman signatures,

even at low temperature (with the exception of *Pt. jambu*), indicates the keratin matrix holds the rhodoxanthin tightly in a, systematic orientation for each feather.

3.5.7 Possibility of isomerization with thin-films of Rhodoxanthin

Of the resonance Raman microscope studies, the unexpected finding is that the thin films of the three isomers have indistinguishable spectra at room temperature with 514.5 nm excitation (**Figure 3.A4-A5**). As shown by the photolysis results shown in **Figure 3.10** isomerization is a likely phenomenon during laser excitation of the thin films and it is possible that the same photoproduct or distribution of photoproducts are formed regardless of the starting configuration. However, during the Raman microscope studies, there were no qualitative changes in the Raman bands over a 15 minutes period, in either peak position or in bandwidth, as should be observable as a result of isomerization. If isomerization does occur, then the rate of isomerization is very fast and equilibrium between the photoproducts is reached within the exposure time of the first acquisition (30 sec).

Attempts to reduce the rate of isomerization by reducing irradiance by using pre-resonant excitation wavelength (568.2 nm) yielded the same result. The ν_1 peak positions of the 6E6'E and 6E6'Z isomers were the same, despite a 1000-fold decrease in the irradiance and a smaller absorption cross section. There are two explanations for this observation. It is possible that the energetic barrier for isomerization is very low and both levels of irradiance cause the majority of the rhodoxanthin thin film to reach isomeric equilibrium within the exposure time of the first acquisition. Alternatively,

the vibrational signatures of the three isomers, although significantly different in solution, could be indistinguishable in thin films. In this case, the distinct (1526–1520 cm^{-1}) ν_1 peak position for each rhodoxanthin isomer in solution, versus the nearly coincident (1520–1521 cm^{-1}) peak positions in thin films, would then lead to the conclusion that solid packing causes more structural/vibrational perturbation for the Z configuration than for the E configuration.

Frank et al. observed similar results when substituting spheroidene and methoxyneurosporene in the photosynthetic reaction center protein of the carotenoid-less *Rhodospseudomonas sphaeroides* mutant R26.¹³⁸ Although these carotenoids have different conjugation lengths, and therefore different absorption maxima in solution, when bound to protein they have the same λ_{max} . They hypothesized that the carotenoids were forced into a configuration where each had equivalent effective conjugation length. Experimental support for this effect in the rhodoxanthin thin films may also be found in the shape of the relative intensity of the 1195 and 1205 cm^{-1} bands. Corresponding to the C-C stretch and C-H bend modes, the intensities are identical in all the thin films but systematically varied in the solution-phase spectra. Therefore, as these modes are considered the structurally sensitive ‘fingerprint’ region, it is possible that within the thin film, the carotenoids are packed in the same way despite isomeric differences, and appear to have the same amount of conjugation and configuration.

Plans were made for photolysis of a pure rhodoxanthin isomer thin film followed by HPLC and UV-Vis analysis, but at this time we lacked enough

rhodoxanthin to complete this check. The results of this experiment will determine the extent of isomerization in the rhodoxanthin thin film.

3.5.8 high- vs low- irradiance experimentation

The possibility of all rhodoxanthin isomerizing instantly with laser exposure is weakened by a comparison of the relatively large amount of isomerization during the photolysis of 6E6'Z in solution with 488.0 nm excitation with no isomerization in any of the isomers in solution with 568.2 nm excitation. Thorough comparison of the 488.0 nm photolysis with the 568.2 nm Raman experiment, we can expect a ~400-fold decrease in isomerization between the high- and low-irradiance setups. In a similar comparison between high- and low- irradiance experiments of rhodoxanthin thin films, we can also estimate a difference of $\sim 10^4$ -fold decrease in the amount of isomerization between high- and low- irradiance. Details of these calculations can be found in the *Supplementary information* (Appendix). At this time, the differences between rates of isomerization of rhodoxanthin in solution or solid-state is not known.

3.5.9 Effect of changing the level of irradiance on resonance Raman spectroscopy

As was discussed above, motivation to explore low-irradiance experimental setup was prompted by possibility of rhodoxanthin isomerization. We now discuss the experimental consequences of using a low- irradiance, 180° backscattering setup in lieu of a high- irradiance Raman microscope.

Although approximately 20x more photons are used for the low-irradiance collection, the probed surface area is increased by a factor of $\sim 10^5$ relative to the area probed by the microscope-focused beam. Resonance Raman microscope spectroscopy is very efficient, and the decrease in irradiance comes at a cost to the photon counts per incident power. The ~ 5000 -fold decrease in irradiance, as seen between the microscope and backscattering experiments, came at a cost of a 10-fold decrease in effective signal (counts per second, normalized for power, as read by the CCD). Therefore, longer collections with higher counts are possible with the low-irradiance setup without sacrificing the integrity of the sample.

Although we have shown that diffusely illuminated resonance Raman spectroscopy is a viable method to probe the vibrational structure of photosensitive and less chemically robust sample, additional considerations must be made when choosing to use this method. The specificity gained with the microscope ($1\ \mu\text{m}$ diameter focus) is lost with the low-irradiance setup. Therefore the specimen probed with a low-irradiance setup should be uniform in composition over the total area that is probed. In addition, the dimensions of the diffuse beam should also be adjusted to reflect the height of the CCD and the slit width of the spectrograph, effectively taking full advantage of the instrument.

3.6 Conclusions

The present study has been motivated by the vast variety of color observed in rhodoxanthin containing birds, including four species of fruit doves (*Ptilinopus*) and a cotinga (Cotingidae). Vibrational, electronic, and reflectance spectroscopy was used to

determine that packing effects, polarization, and distortion of the polyene backbone, as well as possible exciton-coupling are all potential contributors to the variance in electronic and vibrational characteristics observed in the feathers. As with other carotenoid-protein systems, such as crustacean carotenoproteins, the observed results are likely a consequence of several of these mechanisms in concert.⁹² Additionally, while isomeric differences were shown to have little effect on the spectroscopy differences, photonic coloration and differences in concentration are also important factors in the perceived color of the feathers. Finally, low-irradiance experimental setups have been shown to be very effective in obtaining resonance Raman spectra for photosensitive or unstable samples.

This chapter in part is currently being prepared for submission for publication of the material. Berg, Christopher J.; LaFountain, Amy M.; Prum, Richard O.; Frank, Harry A.; Tauber, Michael J. The thesis author was the primary investigator and author of this material.

3.7 Appendix

3.7.1 Supplementary information for publication

Kubelka-Munk is the standard theory to treat a diffusely reflecting medium, where all light traveling through the medium is considered traveling in the positive direction, I_+ (as the direction of incident light) or in the negative direction I_- (opposite to the incident light). The amount of light traveling through length of the medium dx , can be expressed as

$$\frac{dI_+(x)}{dx} = -I_+(x)(K + S) + I_-(x)S \quad \text{Eq. 3.A1}$$

and

$$\frac{dI_-(x)}{dx} = -I_-(x)(K + S) + I_+(x)S \quad \text{Eq. 3.A2}$$

where K and S are the absorption and scattering coefficients of the medium. The solutions for each of the above equations are

$$\frac{d^2I_+}{dx^2} - \kappa^2 I_+ = 0 \quad \text{Eq. 3.A3} \quad \text{and} \quad \frac{d^2I_-}{dx^2} - \kappa^2 I_- = 0 \quad \text{Eq. 3.A4}$$

where $\kappa = K(K + 2S)$. With the boundary conditions that $I_+ = I_0$, where I_0 is the magnitude of the incident light, and $I_-(d) = 0$, where d is the edge of the medium, then the transmittance, T , and reflectance, R , of the sample can be expressed as

$$T = \frac{4\beta}{(1 + \beta)^2 e^{\kappa d} - (1 - \beta)^2 e^{-\kappa d}} \quad \text{Eq. 3.A5}$$

and

$$R = \frac{(1 - \beta^2)(e^{\kappa d} - e^{-\kappa d})}{(1 + \beta)^2 e^{\kappa d} - (1 - \beta)^2 e^{-\kappa d}} \quad \text{Eq. 3.A6}$$

where

$$\beta = \frac{\kappa}{K + 2S} \quad \text{Eq. 3.A7}$$

As the $d \rightarrow \infty$, as ideal for the infinite layer, then $T \rightarrow 0$ and

$$R_{\infty} = \frac{1 - \beta}{1 + \beta} \quad \mathbf{Eq. 3.A8}$$

and

$$F(R) = \frac{K}{S} = \frac{(1 - R_{\infty})^2}{2R_{\infty}} \quad \mathbf{Eq. 3.A9}$$

where $F(R)$ is the remission function. However, feathers are not accurately described by this assumption, and therefore we employ a pile of plates model to correct for the difference, as was previously done for leaves and forest canopies.^{95,96} Previously, a single leaf was modeled as 2 parallel plates, i and j , that either transmit or reflect light. For a single layer, the transmittance ($T_{i,j}$) and reflectance ($R_{i,j}$) can be represented as infinite geometric series that converge as

$$T_{i,j} = \frac{T_i T_j}{1 - R_i R_j} \quad \mathbf{Eq. 3.A10}$$

and

$$R_{i,j} = R_i + \frac{T_i^2 R_j}{1 - R_i R_j} \quad \mathbf{Eq. 3.A11}$$

$T_x(R_x)$ is the transmittance(reflectance) through x layer. These expressions are the derived in Condon and Lagorio (2007)⁹⁵ With the pile of plates model, the total transmittance and reflectance of many leaves is dependent on the a and b Stokes factors as well as the number of layers (or leaves), n .

$$\frac{R}{b^n - b^{-n}} = \frac{T}{a - a^{-1}} \quad \text{Eq. 3.A12}$$

The a and b Stokes factors¹³⁹ are dependent to the diffuse reflectance, r , and diffuse transmittance, t , of a single layer and are defined as

$$a = \frac{1 + r^2 - t^2 + \Delta}{2r} \quad \text{Eq. 3.A13} \quad \text{and} \quad b = \frac{1 - r^2 + t^2 + \Delta}{2t} \quad \text{Eq. 3.A14}$$

where

$$\Delta^2 = (1 + r + t)(1 + r - t)(1 + t - r)(1 - r - t) \quad \text{Eq. 3.A15}$$

Importantly, we can relate the Stokes parameters to the κ and β Kubelka-Munk parameters in the following manner

$$\kappa = \log b \quad \text{Eq. 3.A16}$$

and

$$\beta = \frac{a - 1}{a + 1} \quad \text{Eq. 3.A17}$$

which then gives us

$$K = \frac{a - 1}{a + 1} \log b \quad \text{Eq. 3.A18}$$

and

$$S = \frac{2a}{a^2 - 1} \log b \quad \text{Eq. 3.A19}$$

Therefore, by using the assumptions and model outlined here, it is possible to quantify the absorption and scattering coefficients of a feather from measuring the diffuse transmittance and reflectance of the feather.

Calculated absorption coefficient (K) and scattering coefficient (S) profiles for the 5 feathers

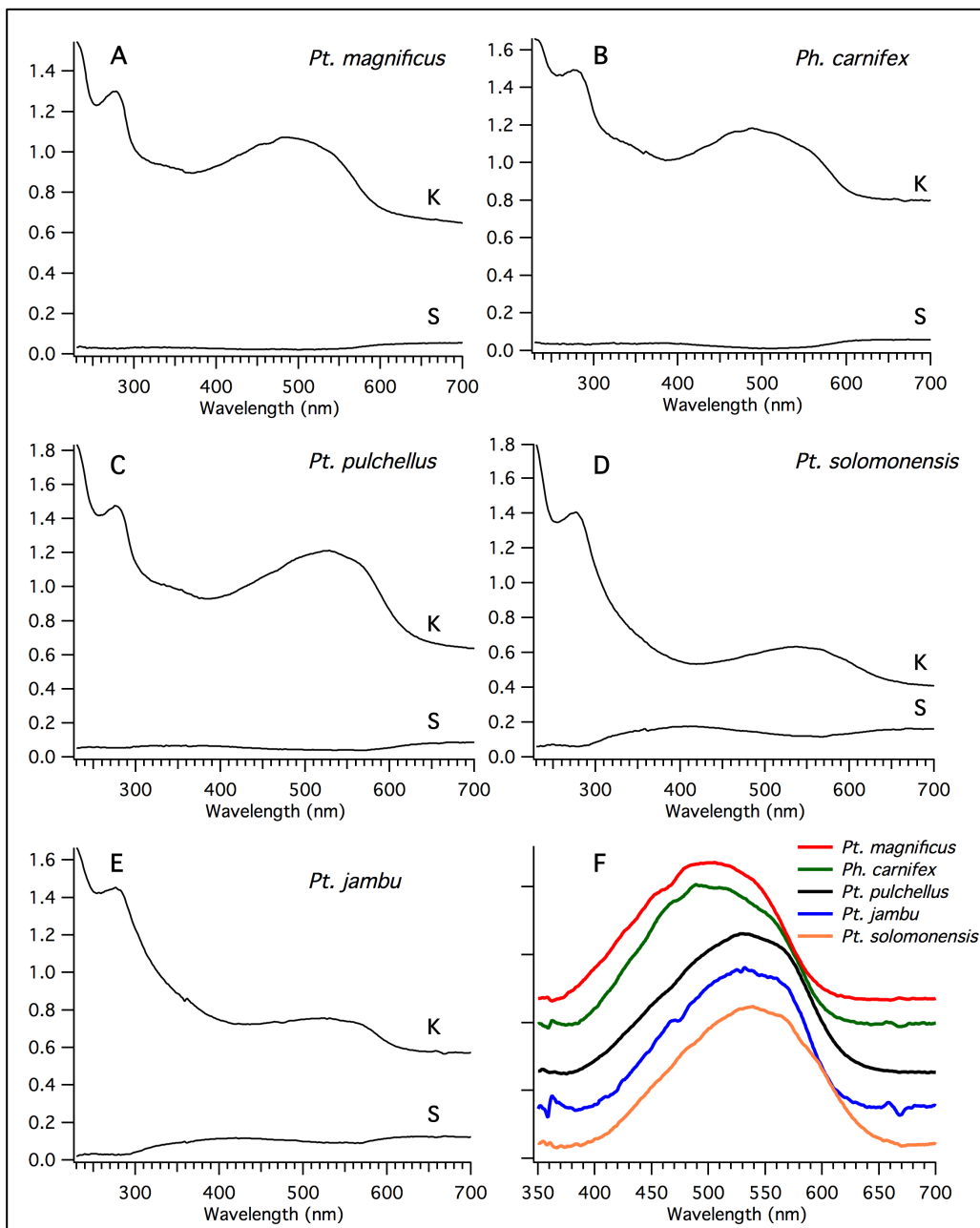


Figure 3.A1: A-E) Absorption coefficient (K) and scattering coefficient (S) profiles for the 5 feathers calculated from the diffuse transmittance and diffuse reflectance spectra. The absorption offset is an artifact of the experimental method. F) Baseline subtracted absorption spectra.

Comparison of low- and high- irradiance resonance Raman spectra of rhodoxanthin containing feathers

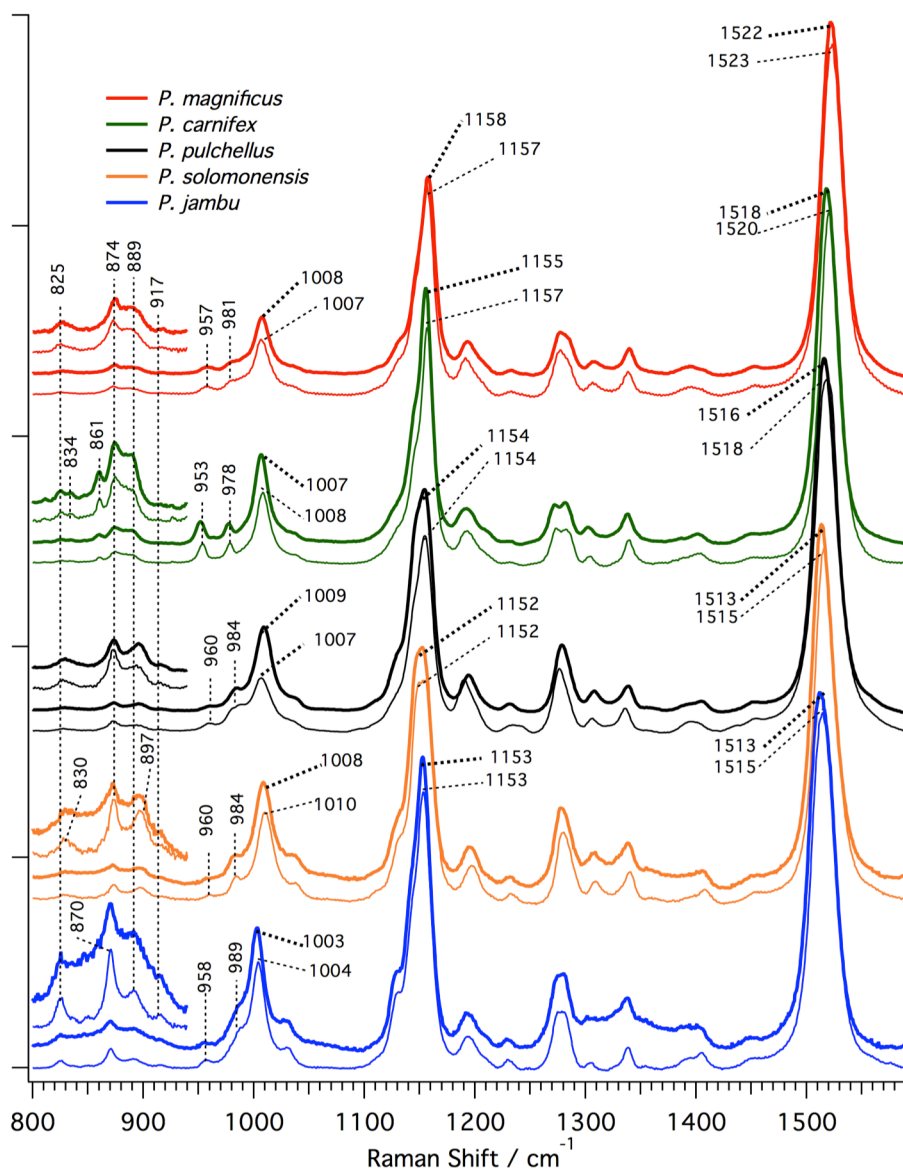


Figure 3.A2: Resonance Raman spectra of avian feathers, with 514.5 nm excitation. The thick lines are the Raman spectra acquired with low-irradiance, using the backscattering setup. The thin lines are spectra acquired with the Raman microscope at much higher irradiance levels. Two offsets were applied uniformly to the spectra within this figure: one offset between spectra of the same feather and one among the five feathers. The peak positions of fundamental modes ν_1 , ν_2 , ν_3 , and bands between 800 – 1000 cm^{-1} are labeled. The feathers are ordered from top to bottom in decreasing ν_1 peak frequency. Magnification of the 750 – 940 cm^{-1} region is 4x.

Absorption Spectra of Rhodoxanthin isomers in DMSO before and after exposure to 568.2 nm laser excitation.

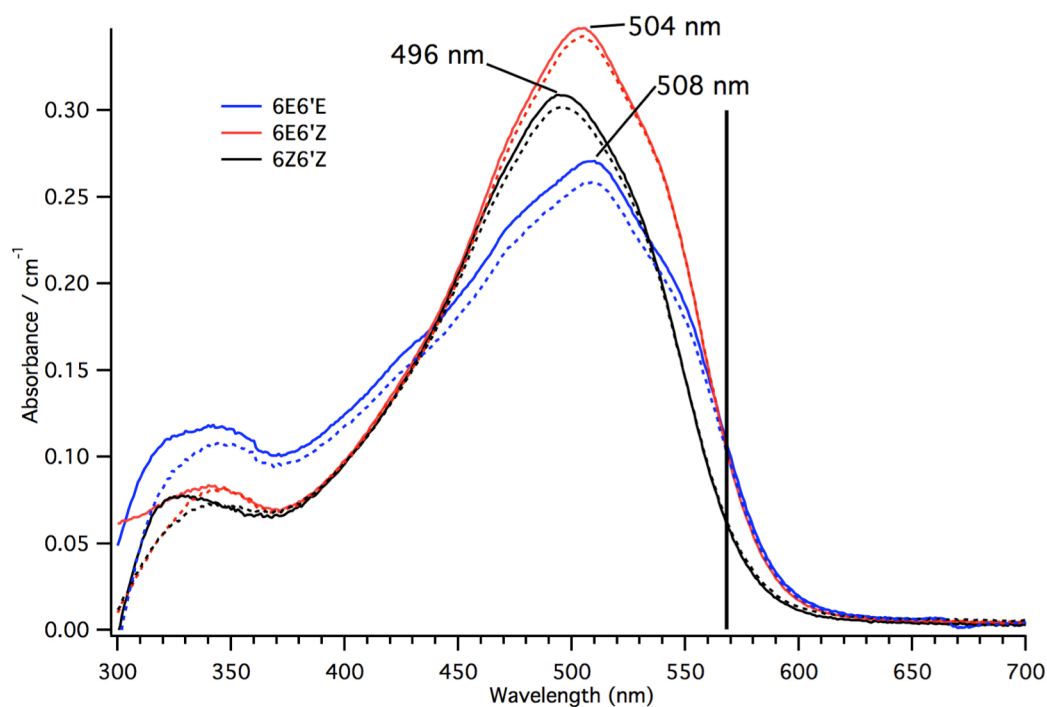


Figure 3.A3: Absorption spectra of rhodoxanthin isomers in DMSO. Solid lines are spectra acquired before photolysis, and dotted lines are spectra acquired after 1 hour of exposure to the laser excitation at 568.2 nm (solid vertical line). Negative features in the near-UV are artifacts caused by a mismatch of sample and reference, exacerbated by insufficient rhodoxanthin solution in the sample cuvette and the absorption of DMSO in the near-UV region. Absorption maxima are labeled.

Comparison of Resonance Raman results of thin films of 6E6'E and 6E6'Z isomers at both high and low irradiance

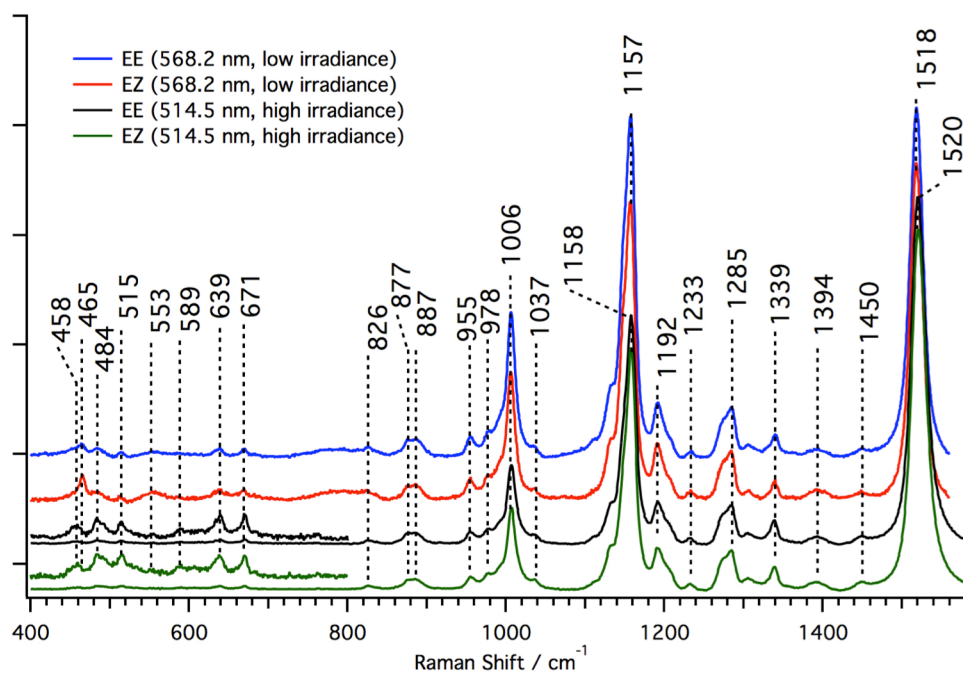


Figure 3.A4: Comparison of resonance Raman spectroscopy of high- and low- irradiance of rhodoxanthin thin films. High- irradiance spectra were taken with 514.5 nm excitation, while low-irradiance spectra were taken with 568.2 nm excitation. Prominent peaks are labeled. The ν_1 peak positions of EE and EZ at low irradiance and EE and EZ at high irradiance are the same.

Comparison of resonance Raman spectra of 6Z6'Z at low- and room-temperature.

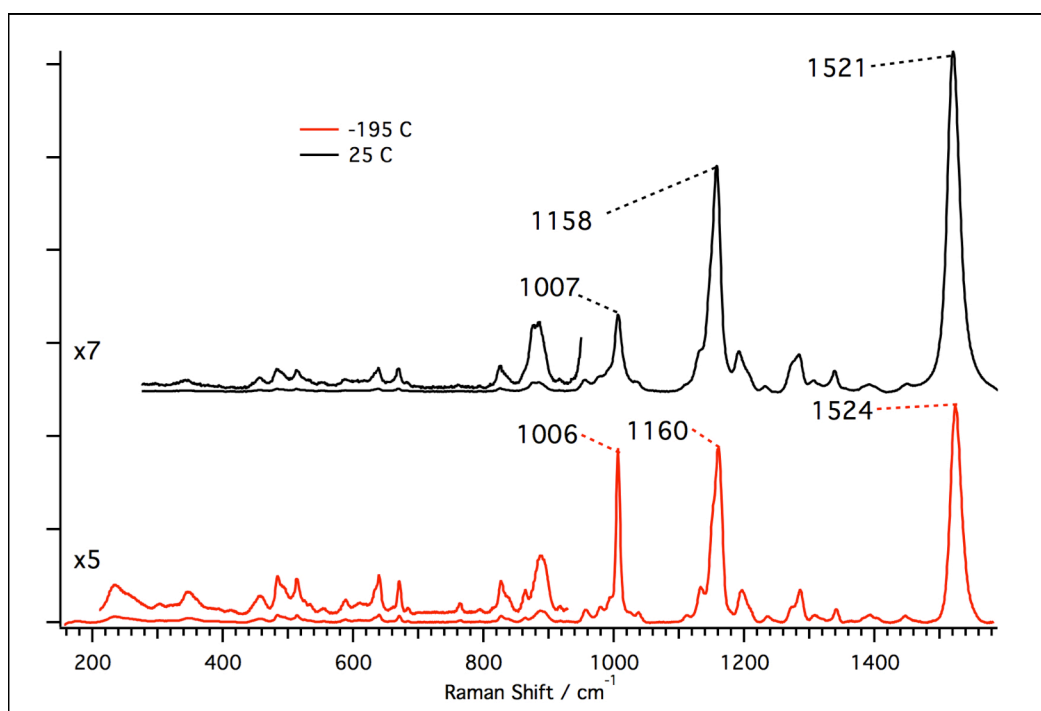


Figure 3.A5: Comparison of resonance Raman spectra of (6Z,6'Z) rhodoxanthin thin film at low temperature (acquired with Linkham LTS420) and at room temperature. Both spectra were acquired with 514.5 nm excitation.

Low-temperature Raman spectroscopy of 6Z6'Z thin film. The low-temperature spectrum of the 6Z6'Z thin film at 514.5 nm excitation is shown in **Figure 3.A5**. Relative to the room temperature spectra, there is a slight upshift ($\sim 2 \text{ cm}^{-1}$) in the peak positions of the ν_1 and ν_2 bands at low temperature. In addition, three constituent bands are resolved in the spectral window $1120\text{--}1170 \text{ cm}^{-1}$, with maxima at 1134 cm^{-1} , 1151 cm^{-1} , and 1161 cm^{-1} (ν_2).

Peak positions of ν_1 , ν_2 , and ν_3 bands for rhodoxanthin thin films and rhodoxanthin containing feathers

Table 3.A1: Rhodoxanthin solvated in DMSO: maxima of select Raman bands of three isomers.

Isomer	ν_1 (C=C stretch)	ν_2 (C-C stretch)	ν_3 (C-CH ₃ rock)
(6E,6'E)	1520	1158	1009
(6E,6'Z)	1524	1160	1012
(6Z,6'Z)	1526	1159	1010

Table 3.A2: Thin films of rhodoxanthin: maxima of select Raman bands of three isomers acquired with low and irradiance excitation.

Isomer	ν_1 (C=C stretch)		ν_2 (C-C stretch)		ν_3 (C-CH ₃ rock)	
	High	Low	High	Low	High	Low
(6E,6'E)	1520	1518	1158	1157	1007	1006
(6E,6'Z)	1520	1518	1158	1157	1007	1006
(6Z,6'Z)	1520	N/A	1158	N/A	1007	N/A

Table 3.A3: Feathers at low-temperature (~195 °C) versus room temperature: maxima of select Raman bands, acquired with high-irradiance excitation.

Feather	Room - temperature			Low - temperature		
	ν_1	ν_2	ν_3	ν_1	ν_2	ν_3
<i>Pt. magnificus</i>	1523	1157	1007	1525	1161, 1149, 1134	1007
<i>Ph. carnifex</i>	1520	1157	1008	1524	1160, 1149, 1131	1009
<i>Pt. pulchellus</i>	1518	1154	1007	1519	1159, 1148, 1132	1011
<i>Pt. solomonensis</i>	1515	1152	1010	1519	1159, 1149, 1133	1012
<i>Pt. jambu</i>	1515	1153	1007	1522	1157, 1143, 1132	1004

Inset of 1550 – 1800 cm^{-1} region of feather and thin film resonance Raman spectra

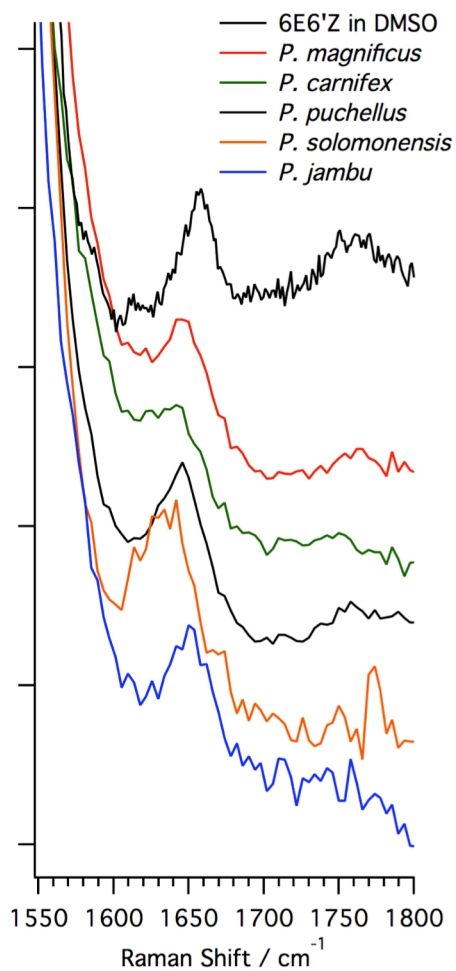


Figure 3.A6: Position of possible carbonyl stretch for the rhodoxanthin and rhodoxanthin-containing feathers. The (6E,6'Z) spectra in DMSO was taken with the macro 90°-setup and the feather spectra were taken with the Raman microscope setup. While 6E6'Z has a prominent band at 1658 cm^{-1} , the feathers have a band $\sim 10 \text{ cm}^{-1}$ downshifted, at 1648 cm^{-1} .

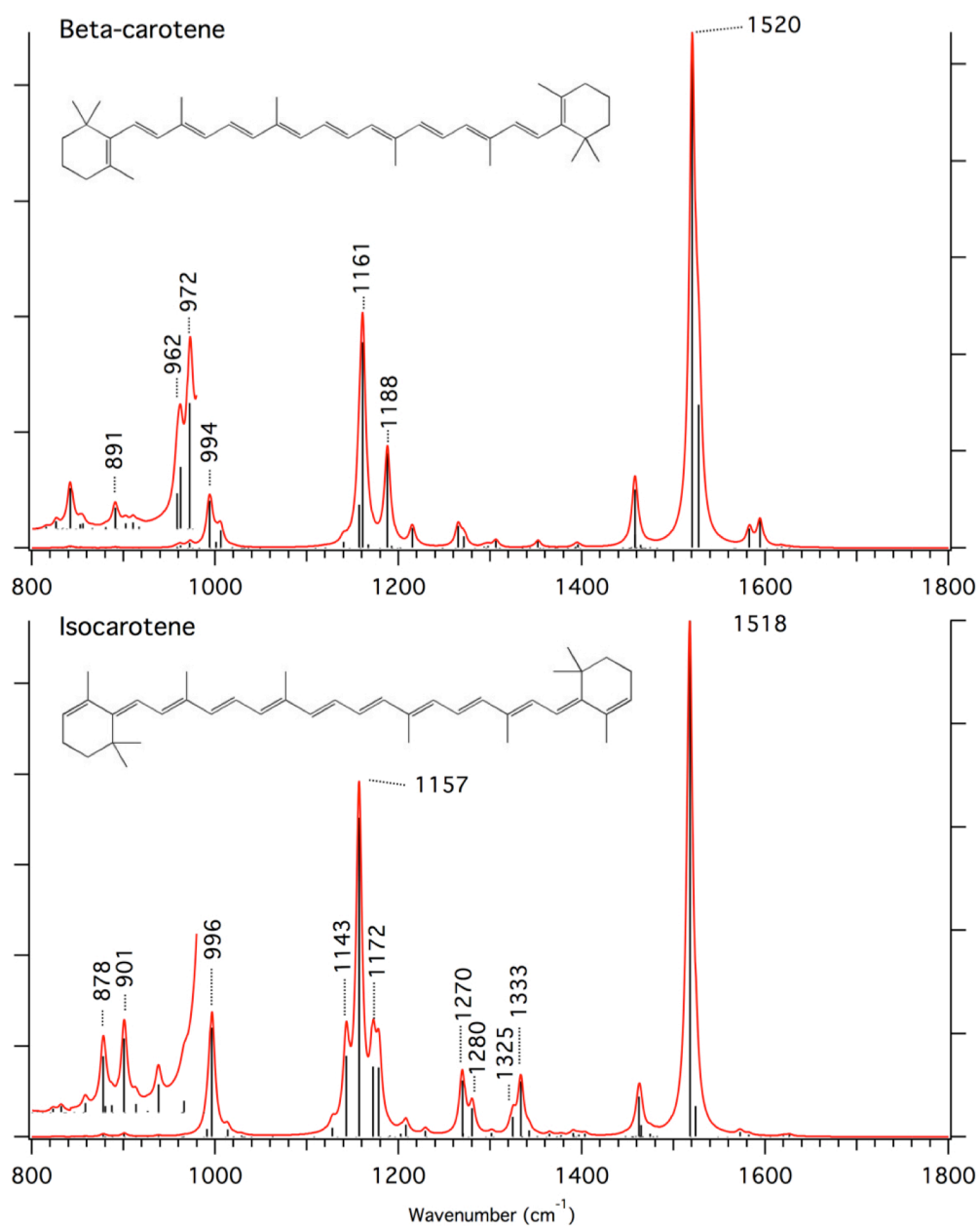


Figure 3.A7: Results of the Gaussian 09W calculations of β -carotene and isocarotene. The 800-973 cm⁻¹ region has been magnified by 25x to clearly show the modes. Selected vibrational modes are labeled. The molecular structures of β -carotene and isocarotene are also shown.

Estimation of rate of isomerization for rhodoxanthin

Of premier importance is the process of isomerization and the ability to quantify the likelihood of isomerization occurring each of the photolysis and Raman experiments. Here we will estimate the rate constant for the isomerization using the photolysis of rhodoxanthin as a standard (described in section 3.4.7) Isomerization is assumed to be a first-order rate process with reaction rate coefficient dependent on concentration of rhodoxanthin, photon flux, and relative absorption coefficient. We also assume that the process of isomerization is an irreversible process, and only occurs once per molecule.

We can express the formation of isomers as

$$\frac{dN_{\text{rhodo,iso}}}{dt} = -\frac{dN_{\text{rhodo}}}{dt} = k_{\text{iso}}N_{\text{rhodo}} \quad \text{Eq. 3.A20}$$

where k_{iso} is the rate constant of isomerization and is equal to

$$\Phi_{\text{iso}}\sigma_{\text{abs}}\frac{N_p}{N_{\text{rhodo},0}} \quad \text{Eq. 3.A21}$$

where Φ_{iso} is the isomerization quantum yield, reported per molecules isomerized per photon, σ_{abs} is the relative absorption cross-section, N_p is the photon flux, and $N_{\text{rhodo},0}$ is the total number of rhodoxanthin molecules in the illuminated area. Rate of isomerization is directly dependent on the relative photon flux per rhodoxanthin molecule, so irradiance and rhodoxanthin concentration are critically important. Photon flux, in photons per second is expressed as

$$N_p = \frac{p}{h\nu} = \frac{p\lambda}{hc} \quad \text{Eq. 3.A22}$$

Where p is power (J s^{-1}), λ is photon wavelength (m), h is planck's constant (J s) and c is the speed of light (m s^{-1}). The integrated rate law is

$$\ln N_{\text{rhodo}} - \ln N_{\text{rhodo},0} = -k_{\text{iso}}t \quad \text{Eq. 3.A23}$$

or

$$N_{\text{rhodo}} = N_{\text{rhodo},0} \exp(-k_{\text{iso}}t) \quad \text{Eq. 3.A24}$$

If we want the proportion of isomerized rhodoxanthin, we assume that $N_{\text{iso}} = N_{\text{rhodo},0} - N_{\text{rhodo}}$. Therefore,

$$\frac{N_{\text{iso}}}{N_{\text{rhodo},0}} = 1 - \exp\left(-\Phi_{\text{iso}}\sigma_{\text{abs}}\frac{N_p}{N_{\text{rhodo},0}}t\right) \quad \text{Eq. 3.A25}$$

With the estimation that $N_{\text{iso}}/N_{\text{rhodo},0}$ is 0.4 and the experimental parameters used in the photolysis experiment, we can calculate that Φ_{iso} is 2.38×10^{-6} molecules/photon for the isomerization of rhodoxanthin in solution. See **Table 3.A4** for a summary of the isomerization parameters.

For sake of argument, if we estimate that 10% of the rhodoxanthin was isomerized during the 514.5 nm excitation Raman experiment, we can calculate that Φ_{iso} is 4.89×10^{-9} molecules/photon for the isomerization of rhodoxanthin in thin films, meaning that there is a $>10^4$ fold decrease in the number of rhodoxanthin

molecules isomerized, with the assumptions made here, between the high and low irradiance photolysis thin films.

Table 3.A4: Isomerization parameters

Experiment	Excitation Wavelength	Power (mW)	Time (s)	# Rhodoxanthin molecules	Sample size	σ_{abs}	$N_{iso}/N_{rhodo,0}$
Photolysis – solution	488.0	200	300	6.88×10^{14}	N/A	1 (MeOH)	.4
Raman – solution	568.2	4.5	900	1.29×10^{15}	N/A	0.05 (MeOH)	1.1×10^{-3}
Raman – solution	514.5	0.050	900	5.41×10^9	1 μ m diameter circle	1 (DMSO)	.1 (example)
Raman – solution	568.2	1.0	900	6.88×10^{14}	2.5 mm x 0.040 mm	.32 (DMSO)	5.87×10^{-6}

In reality, the rate of isomerization should also be motivated by the equilibrium distribution of rhodoxanthin isomers. However, we do not have that information, and therefore cannot take that into consideration.

3.7.2 Assumption of the “pile of plates” model and the effect of ‘sparse’ feathers

The “pile of plates” method assumes that 100% of the incident light interacts with the sample. However, the rhodoxanthin-containing feather samples are sparse, meaning that the not all of the incident light interacts with the feather and the measured *diffuse* reflectance, r , and transmittance, t , data are both changed by I_i/I_0 , the fraction of incident light that interacts with the sample. Therefore, the *diffuse* reflectance and transmittance are lower than they would be if the feathers were more “full”.

While using the “pile of plates” method with Kubelka-Munk theory, the calculated K and S profiles are affected by the unaccounted for light in the following way: the absorption coefficient profile is offset positively while the scattering coefficient profile is negatively offset, giving the impression that the sample absorbs more and scatters less than is accurate. This effect does not change any qualitative aspects of the profiles or multiply the profiles by a scalar. Overlaying the profiles reveals that the spectra are otherwise identical.

Therefore, multiplying r and t by the factor c cancels out the effect of sparse samples, decreasing the absorption offset. For example, if a feather only interacts with 30% of the incident light, multiplying r and t by 2x or 3x, has the same effect as if the feather interacts with 60% or 90% of the incident light, respectively.

Table 3.A5 shows the corresponding K and S values with different given r and t values. From this information, we can confirm several aspects about the “Pile of Plates” method. A sample that has no reflectance and high transmittance is not going to absorb or scatter much. A sample that is not very reflective but also not very reflective is going to be very absorptive but not very scattering. A sample that is very reflective and not transmitting is very scattering and possibly absorptive, depending on value of r .

As we can infer from **Table 3.A5**, if both r and t are decreased because of holes/ gaps in the sample, then it gives the impression that the sample is absorbing more and scattering less than is representative of reality.

Table 3.A5: Example conditions and corresponding reflectance values

Variable	Highly scattering, non absorptive sample	Non-scattering, non-absorbing sample	Highly scattering and absorbing sample	Non-scattering highly absorptive sample
r	0.9	0.05	0.3	0.01
t	0.05	0.9	0.1	0.15
Δ	0.027	0.027	0.806	0.955
a	1.096	3.570	3.297	97.750
b	3.570	1.096	9.090	6.666
K	0.025	0.022	0.512	0.807
S	6.048	0.024	0.640	0.017

Example: Cockatiel (*Nymphicus hollandicus*) feather reflectance and transmittance spectra

To corroborate the information presented above, the diffuse transmittance and reflectance data was collected for a cockatiel tail feather. Two different configurations were used, 1) a feather that interacted with the entire area of the light (**Figure 3.A8a**), and 2) a smaller feather that interacted with the partial area of light (**Figure 3.A8b**).

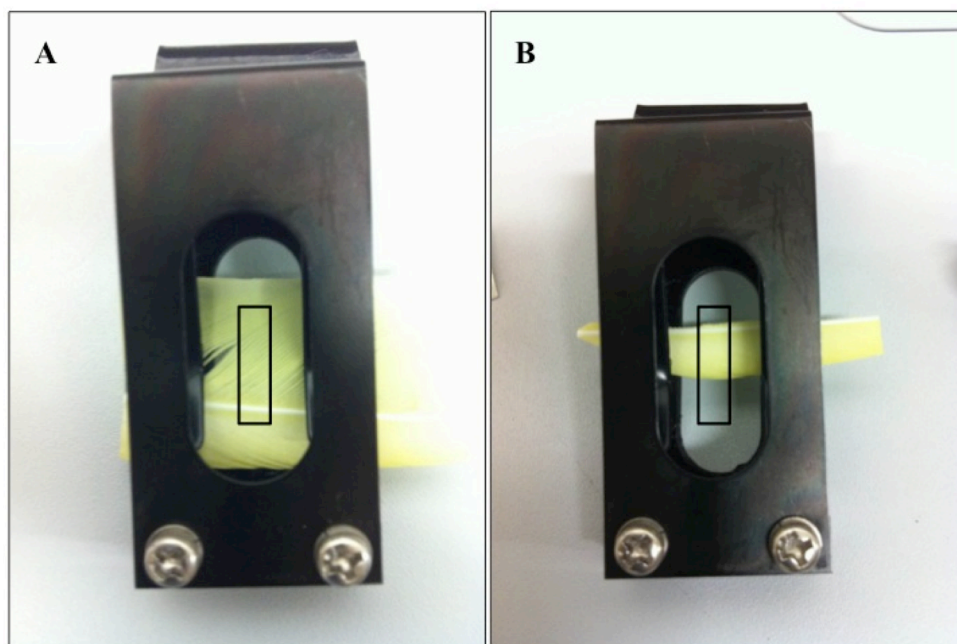


Figure 3.A8: Image of cockatiel feather held in sample holder. The black box shows the area of where the light hits. Two examples are shown: (A) entire beam interacts with the feather (B) only a fraction of the beam interacts with the feather.

As can be shown in **Figure 3.A9**, the partial sample (pictured in **Figure 3.A8b**) has smaller reflectance and transmittance values than the full sample, which correspond to a positive offset in the absorption profile and a negative offset in the scattering profile. Overall, this finding agrees with the above section, and supports the reasoning for the rhodoxanthin-containing feathers. Additionally, other sources of absorption offset would be specular transmittance or reflectance and diffuse scattering that exits the integrating sphere. Even in feather samples that appear to cover the entire light beam, there are also very small holes and gaps that may increase the absorption

offset. Another source of area is the possibility that the beam is not collimated, and thus the beam area changes between the transmittance and reflectance setup.

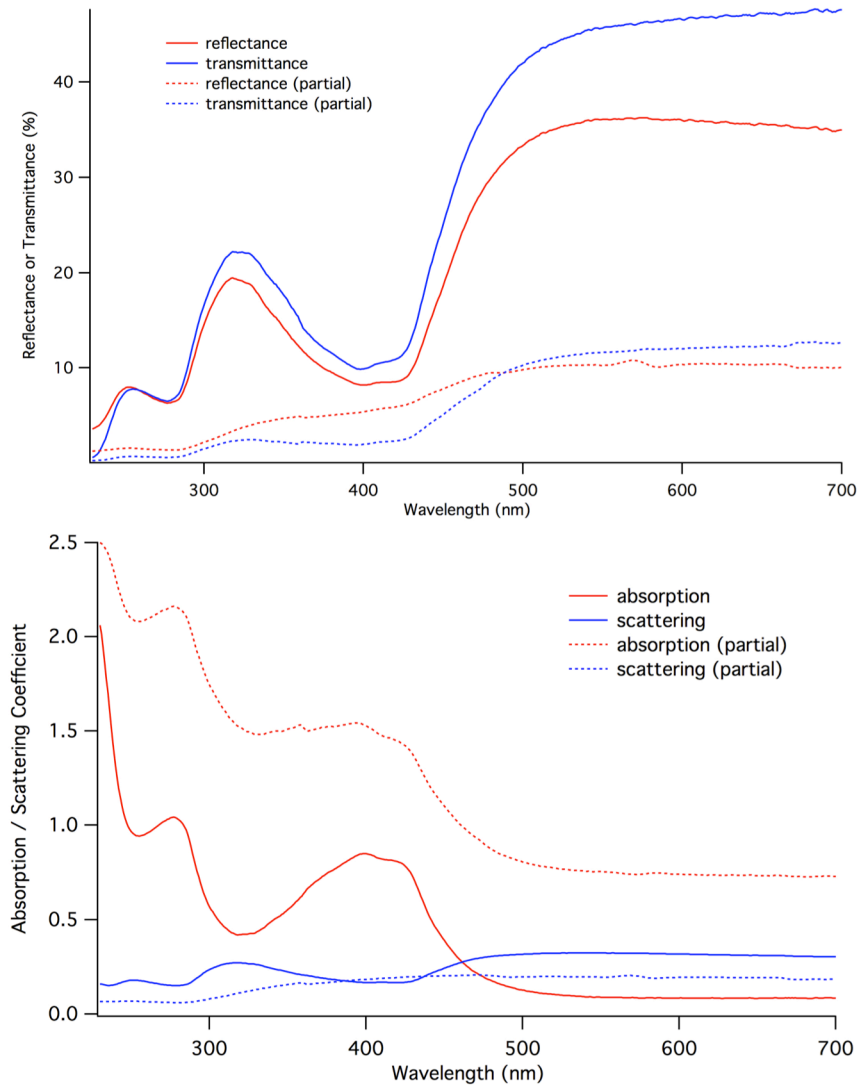


Figure 3.A9: (Top) Diffuse reflectance and transmittance spectra of a fully and partially illuminated cockatiel (*Nymphicus hollandicus*) feathers. (Bottom) the calculated absorption and scattering profiles of the cockatiel feather.

4 Conclusions and Future Studies

4.1 Conclusions

The research in this thesis aims to characterize various aspects of the geometric, electronic, and vibrational structure of carotenoids within aggregates and avian feather environments.

The first topic of the thesis addressed the correlation between the exciton-coupling of zeaxanthin aggregates and the perturbation of the excited state. The photophysical process of singlet-fission, which has important implications for photovoltaics²⁴, has been recently observed in zeaxanthin aggregates¹⁹. Therefore, it is important to understand what conditions are favorable for singlet fission, such as the number of coherently coupled chromophores within the aggregate, aggregate geometry, and coupling strength. This chapter aimed to answer some of these questions.

Although the frequencies of Raman processes are dependent only on the ground state vibrational structure, the intensities of resonantly-enhanced Raman transitions are dependent on the Franck-Condon overlaps of the ground and excited states. In this section the absorption profiles and resonance Raman excitation profiles of the aggregates were compared to the simulated profiles according to a previously developed exciton-coupled dimer model.³² The effects of changing the center-center distance of the monomers, the relative orientation of the monomers, and the

dimensionless displacements of several fundamental vibrational modes on the simulated absorption and rREPs were analyzed, and the parameter sets with the best agreement between the simulated and experimental profiles were found. The coupling between monomers was calculated with both a traditional point-dipole approximation and an extended dipole model. The J1 aggregate, which was previously defined as a weakly-coupled H-type aggregate, was successfully modeled as such with the dimer model. The sharp band of the H aggregate, which was hypothesized to be an inhomogeneous composition of strongly- and weakly- coupled H-type interactions, was fit to a dimer geometry with a very large interaction energy. However, the optimized parameters indicate that the dimer model is insufficient to accurately estimate the distance between each chromophore, and suggests that the exciton is delocalized over several chromophores. Additionally, the dimer model was largely unsuccessful in representing the J2 aggregate, indicating that additional factors are important in its molecular arrangement. The results also suggest that the exciton is constrained to a single chromophore in the J1 and J2 aggregates, as indicated by the similarities of the Huang-Rhys factor between the monomer and aggregates (J1/J2). In comparison, the Huang-Rhys factors optimized for the H aggregate is several times smaller relative to the monomer, which indicates that the exciton is spread between multiple chromophores.

The second section of this thesis investigated the changes of feather color between four species of fruit doves (*Ptilinopus*) and a cotinga (Cotingidae). The feathers of these birds were verified to contain the *retro*-carotenoid, rhodoxanthin, as

their sole or major carotenoid pigment. Using reflectance, transmittance, and resonance Raman spectroscopy, many of the same mechanisms that were applied towards crustacean carotenoproteins^{10, 90, 126, 127} were investigated and considered, including isomeric effects, polyene backbone distortion, polarization mechanisms, and exciton-coupling.

Using Kubelka-Munk analysis and the 'pile of plates' method, an absorption profile was generated for each feather. It was found that the observed color of rhodoxanthin is correlated with the resonance Raman spectra in the expected way, where a decrease in ν_1 frequency is coincident with the red shift of the carotenoid absorption profile.^{3, 140} Additionally, isomeric effects were analyzed through absorption and resonance Raman spectroscopy of the 6E6'E, 6E6'Z, and 6Z6'Z isomers of rhodoxanthin, and it was found that differences in isomer population cannot be a contributing factor to the observed variance in color. Normal mode analysis of each isomer also suggest that 6E6'Z is the most dominant isomer in the feathers.

Several experimental methods for resonance Raman spectroscopy, including low-irradiance and low-temperature spectroscopy were also explored. Low-irradiance Raman spectroscopy was found to be a viable alternative to Raman microscope spectroscopy, especially in cases where photo-degradation or photo-alteration was a possibility. Low-temperature Raman spectroscopy increased the resolution of the Raman spectra and allowed for the observation of closely spaced modes, which were otherwise indistinguishable by room temperature conditions. Although changes in

color can be attributed in part to a change in electronic structure of rhodoxanthin, the mechanism(s) by which the electronic state is perturbed is unknown.

4.2 Future Studies

Although much as been learned from REP analysis of zeaxanthin monomers, there are many questions that remain. It has been known for many years that the point-dipole approximation is inadequate for properly relating the distance between constituent monomers in a dimer to the coupling magnitude. As addressed in the end of Chapter 2, there is room to improve the coupling model through avenues such as the line-dipole approximation⁵⁹. This approximation may be the most accurate approximation for a linear polyene that can be computed in an integrated computational environment where the geometry of the dimer can be rapidly altered in an automated way to find the best fit. Additionally, improvements can be made in the dimer program. Although the dimer program was able to capture many aspects of the zeaxanthin aggregates, even more accurate and precise information can be gained through implementation of a trimer or a two-molecule per unit cell lattice model.⁷⁴

Finally, there are additional applications of the dimer program that may be more suited to its original purpose and current state of research regarding the excited state dynamics of zeaxanthin. Ms. Samantha Doyle of the Tauber group is leading a project involved with the synthesis and excited-state dynamic characterization with zeaxanthin dimers of varying coupling strengths and orientations. Similar REP

analysis of these zeaxanthin dimers would yield critical information regarding the perturbation in the excited states of the molecule.

There are still many questions to be answered regarding carotenoids in the keratin-matrix environment of avian feathers. Although the shifts in absorption spectra and changes in the resonance Raman spectra have been characterized, the actual mechanism(s) that is responsible for the changes are not clear. Particularly, it is not clear how much exciton-coupling is responsible for these changes. The method by which carotenoids bind to the keratin matrix is essential in determining this information. Possible additional studies include systematic *in vitro* spectroscopic experiments of carotenoids on keratin polymers or a similar substrate.

Although both of these topics are limited in scope and bring up more questions than are answered, they point to larger issues and applications. Besides the many roles and functions carotenoids have in nature and its importance as a model for singlet fission, the tunable and variable quality of carotenoid electronic structure in aggregate and biological systems, such as feathers, warrants the continued interest in carotenoids for not only basic science research, but application towards new technologies as well.

5. References

1. G. A. Armstrong and J. E. Hearst, *Faseb Journal* **10** (2), 228-237 (1996).
2. A. B. Myers, *Accounts of Chemical Research* **30** (12), 519-527 (1997).
3. J. C. Merlin, *J. Raman Spectrosc.* **18** (7), 519-523 (1987).
4. K. J. McGraw, in *Bird Coloration vol. 1: Mechanisms and Measurements*, edited by G. E. M. Hill, K.J. (Harvard University Press, Cambridge, MA, 2006).
5. J. D. M. Blount, K. J., in *Carotenoids volume 4: nutrition and health*, edited by G. L.-J. S. P. H. Britton (Birkhäuser, Basel, Switzerland; Boston, MA; Berlin, Germany, 2008), pp. 213-232.
6. A. P. Moller, C. Biard, J. D. Blount, D. C. Houston, P. Ninni, N. Saino and P. F. Surai, *Avian Poult. Biol. Rev.* **11** (3), 137-159 (2000).
7. R. Stradi, G. Celentano, E. Rossi, G. Rovati and M. Pastore, *Comp. Biochem. Physiol. B-Biochem. Mol. Biol.* **110B** (1), 131-143 (1995).
8. M. Mendes-Pinto, A. M. LaFountain, M. C. Stoddard, R. O. Prum, H. A. Frank and B. Robert, *Journal of the Royal Society Interface* (2012).
9. V. R. Salares, N. M. Young, H. J. Bernstein and P. R. Carey, *Biochemistry-US* **16** (21), 4751-4756 (1977).
10. M. Buchwald and W. P. Jencks, *Biochemistry-US* **7** (2), 844-& (1968).
11. P. Horton, A. V. Ruban and R. G. Walters, *Plant Physiol.* **106** (2), 415-420 (1994).
12. H. A. C. Frank, R. J., in *Carotenoids in Photosynthesis*, edited by G. Y. Britton, A (Chapman & Hall, New York, 1993).
13. R. Edge, D. J. McGarvey and T. G. Truscott, *J. Photochem. Photobiol. B-Biol.* **41** (3), 189-200 (1997).
14. B. Demmig-Adams, *Biochimica Et Biophysica Acta* **1020** (1), 1-24 (1990).
15. T. Ishibashi, N. Sorgente, R. Patterson and S. J. Ryan, *Investigative Ophthalmology & Visual Science* **27** (2), 184-193 (1986).

16. J. Ambati, B. K. Ambati, S. H. Yoo, S. Ianchulev and A. P. Adamis, *Survey of Ophthalmology* **48** (3), 257-293 (2003).
17. C. Wang, C. J. Berg, C.-C. Hsu, B. A. Merrill and M. J. Tauber, *The Journal of Physical Chemistry B* **116** (35), 10617-10630 (2012).
18. Y. Mori, K. Yamano and H. Hashimoto, *Chem. Phys. Lett.* **254** (1-2), 84-88 (1996).
19. C. Wang and M. J. Tauber, *J. Am. Chem. Soc.* **132** (40), 13988-13991 (2010).
20. C. A. Wang, Maria; Kuo, Chun-Hung; Tauber, Michael J, in *Physical Chemistry of Interfaces and Nanomaterials XI* (2012), Vol. 8459.
21. C. C. Gradinaru, J. T. M. Kennis, E. Papagiannakis, I. H. M. van Stokkum, R. J. Cogdell, G. R. Fleming, R. A. Niederman and R. van Grondelle, *Proceedings of the National Academy of Sciences of the United States of America* **98** (5), 2364-2369 (2001).
22. E. Papagiannakis, S. K. Das, A. Gall, I. H. M. van Stokkum, B. Robert, R. van Grondelle, H. A. Frank and J. T. M. Kennis, *J Phys Chem B* **107** (23), 5642-5649 (2003).
23. C. S. Wang, Diana E.; Desai, Varsha; Tauber, Michael J., *ChemPhysChem* (2011).
24. D. N. Congreve, J. Lee, N. J. Thompson, E. Hontz, S. R. Yost, P. D. Reusswig, M. E. Bahlke, S. Reineke, T. Van Voorhis and M. A. Baldo, *Science (New York, N.Y.)* **340** (6130), 334-337 (2013).
25. A. B. Myers, R. A. Harris and R. A. Mathies, *J. Chem. Phys.* **79** (2), 603-613 (1983).
26. S. Y. Lee and E. J. Heller, *J. Chem. Phys.* **71** (12), 4777-4788 (1979).
27. M. Kasha, *Rev. Mod. Phys.* **31** (1), 162-169 (1959).
28. M. Kasha, *Radiation Research* **20** (1), 55-& (1963).
29. M. Kasha, H. R. Rawls and M. Ashraf El-Bayoumi, *Eighth European Congress on Molecular Spectroscopy*, 371-392392 (1965).
30. A. S. Davydov, *Theory of Molecular Excitons*. (McGraw-Hill, New York, 1962).

31. S. G. Telfer, T. M. McLean and M. R. Waterland, Dalton Trans. **40** (13), 3097-3108 (2011).
32. A. M. Kelley, J. Chem. Phys. **119** (6), 3320-3331 (2003).
33. G. A. Sherwood, R. Cheng, T. M. Smith, J. H. Werner, A. P. Shreve, L. A. Peteanu and J. Wildeman, J. Phys. Chem. C **113** (43), 18851-18862 (2009).
34. L. A. Peteanu, G. A. Sherwood, J. H. Werner, A. P. Shreve and T. M. Smith, J. Phys. Chem. C **115** (31), 15607-15616 (2011).
35. A. Yassar, G. Horowitz, P. Valat, V. Wintgens, M. Hmyene, F. Deloffre, P. Srivastava, P. Lang and F. Garnier, Journal of Physical Chemistry **99** (22), 9155-9159 (1995).
36. J. L. McHale, J. Phys. Chem. Lett. **3** (5), 587-597 (2012).
37. R. J. Cogdell and H. A. Frank, Biochimica Et Biophysica Acta **895** (2), 63-79 (1987).
38. S. P. Sundelin and S. E. G. Nilsson, Free Radic. Biol. Med. **31** (2), 217-225 (2001).
39. M. Buchwald and W. P. Jencks, Biochemistry-U.S. **7** (2), 834-& (1968).
40. S. Köhn, H. Kolbe, M. Korger, C. Köpsel, B. Mayer, H. Auweter, E. Lüeddecke, H. Bettermann and H.-D. Martin, *Aggregation and Interface Behaviour of Carotenoids*. (2008).
41. F. C. Spano, J. Am. Chem. Soc. **131** (12), 4267-4278 (2009).
42. C. Köpsel, H. Moltgen, H. Schuch, H. Auweter, K. Kleinermanns, H. D. Martin and H. Bettermann, J. Mol. Struct. **750** (1-3), 109-115 (2005).
43. M. B. Smith and J. Michl, Chemical Reviews **110** (11), 6891-6936 (2010).
44. M. C. Hanna and A. J. Nozik, Journal of Applied Physics **100** (7) (2006).
45. E. Shorr and A. M. Kelley, Physical Chemistry Chemical Physics **9** (34), 4785-4792 (2007).
46. A. B. Myers, J. Raman Spectrosc. **28** (6), 389-401 (1997).

47. A. R. Gregory, W. H. Henneker, W. Siebrand and M. Z. Zgierski, *J. Chem. Phys.* **63** (12), 5475-5489 (1975).
48. R. L. Fulton and M. Gouterman, *J. Chem. Phys.* **41** (8), 2280-& (1964).
49. M. H. Perrin, Gouterman M and C. L. Perrin, *J. Chem. Phys.* **50** (10), 4137-& (1969).
50. V. Czikkely, H. D. Forsterling and H. Kuhn, *Chem. Phys. Lett.* **6** (3), 207-210 (1970).
51. C. Bremard, J. Laureyns, J. C. Merlin and G. Turrell, *J. Raman Spectrosc.* **18** (5), 305-313 (1987).
52. G. R. Loppnow and R. A. Mathies, *Biophys. J.* **54** (1), 35-43 (1988).
53. G. G. Kochendoerfer and R. A. Mathies, *Journal of Physical Chemistry* **100** (34), 14526-14532 (1996).
54. A. C. Albrecht and M. C. Hutley, *J. Chem. Phys.* **55** (9), 4438-& (1971).
55. A. J. Stone, *The Theory of Intermolecular Forces*. (Oxford University Press, New York, 1996).
56. B. P. Krueger, G. D. Scholes and G. R. Fleming, *J Phys Chem B* **102** (27), 5378-5386 (1998).
57. U. Roesch, S. Yao, R. Wortmann and F. Wuerthner, *Angewandte Chemie-International Edition* **45** (42), 7026-7030 (2006).
58. I. A. Howard, F. Zutterman, G. Deroover, D. Lamoen and C. Van Alsenoy, *J Phys Chem B* **108** (50), 19155-19162 (2004).
59. W. J. D. Beenken and T. Pullerits, *J. Chem. Phys.* **120** (5), 2490-2495 (2004).
60. D. M. Chen, Y. H. Zhang, T. J. He and F. C. Liu, *Spectrochimica Acta Part a-Molecular and Biomolecular Spectroscopy* **58** (10), 2291-2297 (2002).
61. A. M. Kelley, *Condensed-Phase Molecular Spectroscopy and Photophysics*. (John Wiley & Sons, Inc., Hoboken 2013).
62. A. B. M. R. A. Myers, in *Biological Applications of Raman Spectroscopy*, edited by T. G. Spiro (John Wiley & Sons, New York, 1987), Vol. 2, pp. 1-58.

63. F. Inagaki, M. Tasumi and T. Miyazawa, *Journal of Molecular Spectroscopy* **50** (1-3), 286-303 (1974).
64. H. Okamoto, S. Saito, H. Hamaguchi, M. Tasumi and C. H. Eugster, *J. Raman Spectrosc.* **15** (5), 331-335 (1984).
65. G. G. Maisuradze, *Aust. J. Chem.* **57** (11), 1109-1115 (2004).
66. L. C. Hoskins and M. C. McCarthy, *J. Chem. Phys.* **85** (3), 1322-1326 (1986).
67. L. C. Hoskins, *Spectrochimica Acta Part a-Molecular and Biomolecular Spectroscopy* **42** (2-3), 169-173 (1986).
68. M. K. Lawless and R. A. Mathies, *J. Chem. Phys.* **96** (11), 8037-8045 (1992).
69. W. N. Leng, F. Wurthner and A. M. Kelley, *J Phys Chem B* **108** (29), 10284-10294 (2004).
70. B. P. Nyholm and P. J. Reid, *J Phys Chem B* **108** (25), 8716-8724 (2004).
71. W. N. Leng, J. Grunden, G. P. Bartholomew, G. C. Bazan and A. M. Kelley, *J Phys Chem A* **108** (46), 10050-10059 (2004).
72. S. Choi, J. J. Lee, Y. H. Wei and T. G. Spiro, *J. Am. Chem. Soc.* **105** (11), 3692-3707 (1983).
73. V. A. Morozov, *J. Raman Spectrosc.* **24** (9), 585-589 (1993).
74. R. M. Hochstrasser and M. Kasha, *Photochem. Photobiol.* **3** (4), 317-331 (1964).
75. M. Schreiber and Y. Toyozawa, *J. Phys. Soc. Jpn.* **51** (5), 1528-1536 (1982).
76. D. M. Chen, T. J. He, D. F. Cong, Y. H. Zhang and F. C. Liu, *J Phys Chem A* **105** (16), 3981-3988 (2001).
77. F. C. Spano, *Accounts of Chemical Research* **43** (3), 429-439 (2010).
78. W. Siebrand, *J. Chem. Phys.* **46** (2), 440-& (1967).
79. J. Hudon, M. Anciaes, V. Bertacche and R. Stradi, *Comp. Biochem. Physiol. B-Biochem. Mol. Biol.* **147** (3), 402-411 (2007).

80. R. O. Prum, A. M. LaFountain, J. Berro, M. C. Stoddard and H. A. Frank, *Journal of Comparative Physiology B-Biochemical Systemic and Environmental Physiology* **182** (8), 1095-1116 (2012).
81. P. Vukusic and J. R. Sambles, *Nature* **424** (6950), 852-855 (2003).
82. G. E. Hill, *Nature* **350** (6316), 337-339 (1991).
83. M. C. Witmer, *Auk* **113** (4), 735-743 (1996).
84. J. Hudon and A. H. Brush, *J. Field Ornithol.* **60** (3), 361-368 (1989).
85. O. Volker, *Journal fuer Ornithologie* **94**, 263-273 (1953).
86. P. F. Zagalsky, *Pure and Applied Chemistry* **47** (2-3), 103-120 (1976).
87. G. Eyring, B. Curry, R. Mathies, R. Fransen, I. Palings and J. Lugtenburg, *Biochemistry-U.S.* **19** (11), 2410-2418 (1980).
88. B. Durbeej and L. A. Eriksson, *Chem. Phys. Lett.* **375** (1-2), 30-38 (2003).
89. P. R. Carey, R. G. Carriere, D. J. Phelps and H. Schneider, *Biochemistry-U.S.* **17** (6), 1081-1087 (1978).
90. V. R. Salares, N. M. Young, H. J. Bernstein and P. R. Carey, *Biochimica Et Biophysica Acta* **576** (1), 176-191 (1979).
91. I. Palings, J. A. Pardo, E. Vandenberg, C. Winkel, J. Lugtenburg and R. A. Mathies, *Biochemistry-U.S.* **26** (9), 2544-2556 (1987).
92. P. F. Zagalsky, E. E. Eliopoulos and J. B. C. Findlay, *Comp. Biochem. Physiol. B-Biochem. Mol. Biol.* **97** (1), 1-18 (1990).
93. M. Veronelli, G. Zerbi and R. Stradi, *J. Raman Spectrosc.* **26** (8-9), 683-692 (1995).
94. M. C. Stoddard and R. O. Prum, *Am. Nat.* **171** (6), 755-776 (2008).
95. G. B. Cordon and M. Gabriela Lagorio, *J. Chem. Educ.* **84** (7), 1167-1170 (2007).
96. W. A. Allen and A. J. Richards, *Journal of the Optical Society of America* **58** (8), 1023-& (1968).

97. M. L. Myrick, M. N. Simcock, M. Baranowski, H. Brooke, S. L. Morgan and J. N. McCutcheon, *Applied Spectroscopy Reviews* **46** (2), 140-165 (2011).
98. A. M. LaFountain, S. Kaligotla, S. Cawley, K. M. Riedl, S. J. Schwartz, H. A. Frank and R. O. Prum, *Arch. Biochem. Biophys.* **504** (1), 142-153 (2010).
99. K. J. McGraw, J. Hudon, G. E. Hill and R. S. Parker, *Behav. Ecol. Sociobiol.* **57** (4), 391-397 (2005).
100. G. Britton, S. LiaaenJensen and H. Pfander, *CAROTENOIDS HANDBOOK*. (Birkhäuser Verlag, Basel, Boston, Berlin, 2004).
101. P. Kubelka and F. Munk, *Z. Tech. Phys.* **12** (11a), 593-601 (1931).
102. W. W. M. W. Hecht, H.G., *Reflectance Spectroscopy*. (Interscience Publishers, New York, 1966).
103. M. J. T. Frisch, G. W.; Schlegel, H. B.; Scuseria, G. E.; Robb, M. A.; Cheeseman, J. R.; Scalmani, G.; Barone, V.; Mennucci, B.; Petersson, G. A.; Nakatsuji, H.; Caricato, M.; Li, X.; Hratchian, H. P.; Izmaylov, A. F.; Bloino, J.; Zheng, G.; Sonnenberg, J. L.; Hada, M.; Ehara, M.; Toyota, K.; Fukuda, R.; Hasegawa, J.; Ishida, M.; Nakajima, T.; Honda, Y.; Kitao, O.; Nakai, H.; Vreven, T.; Montgomery, Jr., J. A.; Peralta, J. E.; Ogliaro, F.; Bearpark, M.; Heyd, J. J.; Brothers, E.; Kudin, K. N.; Staroverov, V. N.; Kobayashi, R.; Normand, J.; Raghavachari, K.; Rendell, A.; Burant, J. C.; Iyengar, S. S.; Tomasi, J.; Cossi, M.; Rega, N.; Millam, J. M.; Klene, M.; Knox, J. E.; Cross, J. B.; Bakken, V.; Adamo, C.; Jaramillo, J.; Gomperts, R.; Stratmann, R. E.; Yazyev, O.; Austin, A. J.; Cammi, R.; Pomelli, C.; Ochterski, J. W.; Martin, R. L.; Morokuma, K.; Zakrzewski, V. G.; Voth, G. A.; Salvador, P.; Dannenberg, J. J.; Dapprich, S.; Daniels, A. D.; Farkas, Ö.; Foresman, J. B.; Ortiz, J. V.; Cioslowski, J.; Fox, D. J., (Gaussian, Inc., Wallingford CT, 2009).
104. O. Volker, *Hoppe-Seylers Zeitschrift Fur Physiologische Chemie* **290**, 223-227 (1952).
105. S. Andersson, M. Prager and E. I. A. Johansson, *Functional Ecology* **21** (2), 272-281 (2007).
106. J. Hudon, G. F. Grether and D. F. Millie, *Physiol. Biochem. Zool.* **76** (6), 776-790 (2003).
107. K. R. Millington, *Amino Acids* **43** (3), 1277-1285 (2012).
108. P. Meredith and T. Sarna, *Pigment Cell Research* **19** (6), 572-594 (2006).

109. G. Eyring, B. Curry, A. Broek, J. Lugtenburg and R. Mathies, *Biochemistry-U.S.* **21** (2), 384-393 (1982).
110. I. Palings, E. M. M. Vandenberg, J. Lugtenburg and R. A. Mathies, *Biochemistry-U.S.* **28** (4), 1498-1507 (1989).
111. E. Nicoara, V. Tamas, G. Neamtu and C. Bodea, *Annalen Der Chemie-Justus Liebig* **697** (SEP), 201-+ (1966).
112. R. J. Weesie, J. C. Merlin, J. Lugtenburg, G. Britton, F. Jansen and J. P. Cornard, *Biospectroscopy* **5** (1), 19-33 (1999).
113. A. Requena, J. P. Ceron-Carrasco, A. Bastida, J. Zuniga and B. Miguel, *J Phys Chem A* **112** (21), 4815-4825 (2008).
114. R. M. W. Silverstein, F. X.; Kiemle, D. J., *Spectrometric identification of organic compounds* (John Wiley & Sons, Inc., Hoboken, NJ, 2005).
115. E. Widmer, R. Zell, H. Grass and R. Marbet, *Helv. Chim. Acta* **65** (3), 958-967 (1982).
116. J. Hudon, A. Storni, E. Pini, M. Anciaes and R. Stradi, *Auk* **129** (3), 491-499 (2012).
117. M. M. Katsugama, T., *Bulletin of the Japanese Society of Scientific Fisheries* **45** (8), 1045 (1979).
118. J. Hudon, *Can. J. Zool.-Rev. Can. Zool.* **69** (9), 2311-2320 (1991).
119. I. Renge and E. Sild, *J. Photochem. Photobiol. A-Chem.* **218** (1), 156-161 (2011).
120. S. E. Wood, S. Langer and R. Battino, *J. Chem. Phys.* **32** (5), 1389-1393 (1960).
121. R. G. LeBel and D. A. I. Goring, *Journal of Chemical & Engineering Data* **7** (1), 100-101 (1962).
122. D. J. Brink and N. G. van der Berg, *J. Phys. D-Appl. Phys.* **37** (5), 813-818 (2004).
123. A. K. Samanta, P. Pandey, B. Bandyopadhyay and T. Chakraborty, *J. Mol. Struct.* **963** (2-3), 234-239 (2010).

124. F. Zsila, J. Deli, Z. Bikadi and M. Simonyi, *Chirality* **13** (10), 739-744 (2001).
125. W. I. Gruszecki, in *The Photochemistry of Carotenoids*, edited by H. A. Y. Frank, A. J.; Britton, G; Cogdell, R. J. (Kluwer Academic Publishers, 1999), pp. 363-379.
126. A. A. C. van Wijk, A. Spaans, N. Uzunbajakava, C. Otto, H. J. M. de Groot, J. Lugtenburg and F. Buda, *J. Am. Chem. Soc.* **127** (5), 1438-1445 (2005).
127. A. Strambi and B. Durbeej, *J Phys Chem B* **113** (15), 5311-5317 (2009).
128. R. P. Ilagan, R. L. Christensen, T. W. Chapp, G. N. Gibson, T. Pascher, T. Polivka and H. A. Frank, *J Phys Chem A* **109** (14), 3120-3127 (2005).
129. H. W. Yin, L. Shi, J. Sha, Y. Z. Li, Y. H. Qin, B. Q. Dong, S. Meyer, X. H. Liu, L. Zhao and J. Zi, *Phys. Rev. E* **74** (5) (2006).
130. J. Zi, X. D. Yu, Y. Z. Li, X. H. Hu, C. Xu, X. J. Wang, X. H. Liu and R. T. Fu, *Proceedings of the National Academy of Sciences of the United States of America* **100** (22), 12576-12578 (2003).
131. L. D'Alba, V. Saranathan, J. A. Clarke, J. A. Vinther, R. O. Prum and M. D. Shawkey, *Biol. Lett.* **7** (4), 543-546 (2011).
132. M. G. Meadows, N. I. Morehouse, R. L. Rutowski, J. M. Douglas and K. J. McGraw, *Behav. Ecol. Sociobiol.* **65** (6), 1317-1327 (2011).
133. J. C. J. Bart and C. H. Macgillavry, *Acta Crystallographica Section B-Structural Crystallography and Crystal Chemistry* **B 24**, 1587-& (1968).
134. S. Saito, M. Tasumi and C. H. Eugster, *J. Raman Spectrosc.* **14** (5), 299-309 (1983).
135. M. J. Allen, J. D. Fowler, V. C. Tung, Y. Yang, B. H. Weiller and R. B. Kaner, *Appl. Phys. Lett.* **93** (19) (2008).
136. T. R. Hart, R. L. Aggarwal and B. Lax, *Physical Review B-Solid State* **1** (2), 638-& (1970).
137. P. F. Zagalsky, E. E. Eliopoulos and J. B. C. Findlay, *Biochemical Journal* **274**, 79-83 (1991).
138. H. A. Frank, B. W. Chadwick, S. Taremi, S. Kolaczowski and M. K. Bowman, *Febs Letters* **203** (2), 157-163 (1986).

139. G. G. Stokes, Proceedings of the Royal Society of London **11**, 545-556 (1862).
140. L. Rimai, M. E. Heyde and D. Gill, J. Am. Chem. Soc. **95** (14), 4493-4501 (1973).